

High Frequency Noise Detection in Mesoscopic Devices

High Frequency Noise Detection in Mesoscopic Devices

Proefschrift

ter verkrijging van de graad van doctor
aan de Technische Universiteit Delft,
op gezag van de Rector Magnificus prof.dr.ir. J.T. Fokkema,
voorzitter van het College voor Promoties,
in het openbaar te verdedigen

op dinsdag 13 september 2005 om 10.30 uur

door

Gabriel-Eugen ONAC

natuurkundig master, Universiteit van Boekarest
geboren te Luduș, România.

Dit proefschrift is goedgekeurd door de promotor:

Prof. dr. ir. L. P. Kouwenhoven

Samenstelling van de promotiecommissie:

Rector Magnificus,	voorzitter
Prof. dr. ir. L. P. Kouwenhoven	Technische Universiteit Delft, promotor
Prof. dr. C. Schönenberger	Universität Basel, Zwitserland
Prof. dr. H. Schoeller	RWTH Aachen, Duitsland
Prof. dr. J. M. van Ruitenbeek	Universiteit Leiden
Prof. dr. ir. T. M. Klapwijk	Technische Universiteit Delft
Prof. dr. Yu. V. Nazarov	Technische Universiteit Delft
Dr. C. J. P. M. Harmans	Technische Universiteit Delft
Dr. Y. Blanter	Technische Universiteit Delft



Published by: Gabriel-Eugen Onac

Printed by: Cendris, Delft

An electronic version of this thesis, including colour figures, is available at:
<http://www.library.tudelft.nl/dissertations/>

Copyright © 2005 by Gabriel-Eugen Onac

Preface

This thesis presents the main results on the study of high frequency shot noise; an experimental work I carried out in the Quantum Transport group under the supervision of Leo Kouwenhoven. My first contact with the group was in the summer of 2000, during an interview visit. I was positively impressed and decided to start a PhD here. This was not always easy, as I started on a completely new project, not only for me, but also for the group in Delft. Still, after four and a half years, I can say that I could not be happier about my choice. I had the opportunity to work in one of the best groups in the field, within an excellent scientific environment and benefitted from state of the art facilities. But the group's main advantage is represented by its people: besides being excellent scientists they are also great persons with a wide range of interests.

First I would like to express my gratitude to my supervisor, Leo Kouwenhoven, for giving me the opportunity to work here. I always admired your scientific knowledge, bright ideas and your clear way of expressing them. I am grateful for the time spent together. Thank you also for the financial support (e.g. for international conferences, football, free drinks). On many occasions, I could notice that, any former member of QT remembers with happiness and pride the moments spent in Delft. For the what has become a 'QT spirit', I would like to thank Hans Mooij.

I am grateful to Kees Harmans for initiating me in the field of shot noise. Your vast theoretical and experimental expertise was of great help at the beginning, as well as during my PhD. After one year, Richard Deblock joined the shot noise project. I appreciated his rigorous and effective way of working, and his clear and solid answers to many of my scientific questions. I learned a lot from him and I am grateful for that. I also want to thank Franck Balestro for the work we did together. I enjoyed the (sometimes late) hours in the lab and the numerous discussions we had. My thanks also for Silvano de Franceschi, co-founder of the maintenance museum for the 'Frosatti fridge'. Out of the many reasons, I will just mention several: helpful scientific discussions, setting up the F016 fridge, entertaining the football atmosphere, initiation in Gaspanic experiences. During the last year Björn Trauzettel joined QT for a couple of days each week. I

benefitted from his remarkable theoretical insight into the shot noise field and I thank him for all the help.

The atmosphere in the office was always enjoyable thanks to my roommates: Caspar van der Wal, Erwin Slot, Hannes Majer, Diederik Rep, Sami Sapmaz, Yong-Joo Doh. Erwin, bedank voor de Nederlandse lessen. ‘Hannes Majer’ is already a well established tag for high quality software and hardware work in research labs. Thank you for your hospitality during my visit to Yale. Sami I really enjoyed your company and our numerous discussions. And I know I am not a singular case. Yong-Joo thanks for valuable advices and SIS related explanations.

During my PhD I had many interactions with the ‘quantum dot’ team. Special thanks to the dots’ king, Jeroen Elzerman. I always appreciated your friendly spirit and your advices on quantum dots measurements. I am also grateful to Ronald Hanson (I have a photo that will be worth a lot of money) and Laurens Willems van Beeveren (bedankt beide voor de samples), Ivo Vink (thanks for the summary translation), Wilfred van der Wiel and ‘omG’ Tristan Meunier.

I would also like to thank Jorden van Dam, Hubert Heersche (too bad we didn’t measure the spin noise in the end, but we hiked in the Grand Canyon), Alexander ter Haar, Floris Zwanenburg (sometimes bad words, but excellent Romanian accent), Lieven Vandersypen, Piotr Beliczynski, Kees Veerwijs (thanks for the tennis games), Pablo Jarillo-Herrero and Chris Lodewijk (thanks for the nanotube fabrication), Ethan Minot, Jelle Plantenberg. There are also several former QT members that I would like to mention here: Alberto Morpurgo (are there any Romanians in the pipeline?), Herre van der Zant (always in front, ready to score), Peter Hadley (thank you for helpful discussions on SET and SIS). I know there are many others I did not mention here and I would like to thank all of them for the great time spent in the QT.

For the theoretical part I am grateful to Yuli Nazarov, Yaroslav Blanter, Udo Hartmann, Dimitri Bagret, Ramon Aguado. Thank you all for enlightening and inspiring discussions. Particular thanks to Yuli Nazarov and Udo Hartmann for discussions and simulations on the quantum dot detection data.

Our results would have not been possible without the the excellent support provided by our technicians. Special thanks to Bram van der Enden and to our electronics wizard, Raymond Schouten, for their invaluable assistance. I am also grateful to Leo Dam, Wim Schot, Maascha van Oossanen and Leo Lander for technical support and liquid He supply. For all the paperwork I want to express my gratitude to our secretaries Yuki French Nakagawa and Ria van Heeren - van der Kramer.

I could always use a couple of Romanian jokes to charge my batteries, and

some network games to completely empty them. For the atmosphere in our apartment I am grateful to Odi, Anda and Giga. Odi thanks for keeping the apartment safe (usa, apa, gaz, curent...) and joyful at the same time. Anda thank you for your support and for the time spent together. Dziga thanks for enjoyable long discussions about technical, economical, political, social (and probably all other sorts) of matters.

I would like to thank Irinel, Adrian, Monique, Mara and Oana M. for the Romanian chats and events in Delft. I also thank my Leiden connection, Iulian and Ancuța, for great lunches, dinners and parties. For many extraordinary weekends in Groningen and in Delft, I am grateful to Cătălin and Mihaela (thank you for your hospitality and the great cooking), partenera Oana J., Vălică, Lăcră and Lucică. I appreciated your friendship and the great times spent together.

Finally, but most importantly, I want to thank my brother and my parents for their unconditioned love and support. Although so far away, I always felt you by my side. I am grateful to my girlfriend Alina for her continuous love and understanding. Thank you.

Eugen Onac
Delft, August 2005

Contents

1	Introduction	1
1.1	History	2
1.2	Motivation	3
1.3	Thesis Layout	4
	References	5
2	Noise Concepts. Systems used. Measurement techniques	7
2.1	Sources of Noise	8
2.1.1	Thermal Noise	9
2.1.2	Shot Noise	10
2.1.3	Quantum Noise	11
2.1.4	1/f Noise	14
2.2	Systems Used. Sample Fabrication	14
2.2.1	Josephson Junctions	14
2.2.2	Quantum Dots	16
2.2.3	Semiconductor 2DEG Structures	20
2.2.4	Carbon Nanotubes	22
2.3	Low Temperature Measurements	23
2.4	Noise Measurement Techniques	25
2.4.1	Low frequency cross-correlation technique	25
2.4.2	Resonant scheme for noise detection at MHz frequencies	26
2.4.3	High frequency detection scheme using rectifying diodes	27
2.4.4	On chip detection of high frequency signals	28
	References	30
3	On chip Detection of Quantum Noise in Mesoscopic Devices	33
3.1	Introduction	34
3.2	Method	36
3.2.1	Theory of SIS junction as a detector for HF fluctuations	38
3.2.2	The coupling circuitry. Fabrication	41

3.3	High frequency emission of a Josephson Junction	44
3.3.1	AC Josephson effect	44
3.3.2	Shot noise of the quasiparticle current	47
3.4	Power and efficiency	49
3.5	Conclusions	49
	References	50
4	Detection of Quantum Noise from an Electrically-Driven Two-Level System	51
4.1	Introduction	52
4.2	Sample Fabrication and Characterization	54
4.3	Noise Emission on the JQP Peak	57
4.4	Emission Noise at Larger Biases	59
4.5	Conclusions	60
	References	61
5	Shot Noise Detection on a Carbon Nanotube Quantum Dot	65
5.1	Introduction	66
5.2	Detection Principle and Calibration	67
5.2.1	Sample Fabrication	67
5.2.2	Calibration	68
5.3	Carbon Nanotube Characterization. Noise Detection	70
5.4	Conclusions	77
	References	77
6	A Quantum Dot as a High Frequency Shot Noise Detector	81
6.1	Introduction	82
6.2	Sample Characterization	83
6.3	Noise Detection	84
6.4	Theoretical Model	86
6.5	High Frequency Cut-off	89
6.6	Conclusions	90
	References	90
A	Quasiparticle tunneling current in the presence of an environment	93
	References	97
B	Properties and measurement of the calibration function	99

Summary	103
Samenvatting	107
Curriculum Vitae	111
List of publications	113

Chapter 1

Introduction

1.1 History

The physical description of our world was based, at the end of the 19th century, on classical, deterministic theories. Newton's laws for mechanics together with Maxwell's equations for the electromagnetic field and its interaction with the matter can be used to obtain an accurate description of the processes taking place at macroscopic scale. These are deterministic theories: if the state of a system, together with all the external conditions, are known at a certain moment one can calculate, using these theories, the evolution of the system at any later time, with any accuracy.

In 1900, Max Planck introduced the idea that energy is quantized, in order to derive a formula for the observed frequency dependence of the energy emitted by a black body. This represented the first phenomenological introduction (with no rigorous justification) of a quantum mechanical concept. Similar ideas were introduced shortly afterwards by Einstein and Bohr and, in 1924, Louis de Broglie put forward his theory of matter waves. All these were confirmed by the theory of quantum mechanics, developed in the first part of the last century with important contribution from scientists like Heisenberg, Schrödinger, Pauli or Dirac. Quantum mechanics uses the concept of wave-particle duality to describe light and matter: they can have both waves or particles behavior characteristics. For example a wave function is used to describe the state of an electron. The electron is not localized in space anymore: the probability to find it at a certain position can be calculated from the wave function. At one moment, the position and the velocity of the electron can only be determined within a certainty limit.

Quantum mechanics leads to non-intuitive notions such as quantum superposition and quantum entanglement. Quantum superposition of states refers to the possibility for a quantum system to be in two (or more) states at the same time. The measurement process of the actual state, will force the system, randomly, into one of the measurement eigenstates. Therefore, the result is non-deterministic and only the probability for each outcome is a determined quantity [2]. Furthermore, when two systems interact their states can become entangled: in this case the complete state of the whole system can be known, but the individual states of the subsystems are not necessarily determined. However, due to the strong correlation between the subsystems, a measurement made on one of them will automatically determine the state of the other, even when they are arbitrarily far away. These quantum features make possible the realization of physical phenomena such as quantum teleportation [3, 4] and quantum parallelism. They represent important tools in the context of quantum communication and quantum computation [5], promising a substantial speed-up of the calculation time

for certain problems.

1.2 Motivation

Based on the experiences of our macroscopic world, quantum effects are not intuitive. Therefore, one could be tempted to think that we are "safe" from experiencing them in our everyday life. This will certainly not be case in the future. The fast advance of electronic devices and the continuous race for their miniaturization are quite accurately described by the famous Moore's law [1]. Gordon Moore observed, in 1965, that the number of transistors per square inch of integrated circuits double every couple of years. The prediction for this exponential development is still valid our days. Nevertheless, a slowdown in this evolution can be predicted as the physical dimensions of the transistors approach the size of individual atoms. Here, the classical physics laws can not be used anymore to describe the transport, and quantum effects, due to the reduced dimensionality, need to be taken into account. While some aspects of the quantum behavior might represent a nuisance for future devices (e.g. current leakage due to quantum tunneling or the intrinsic current fluctuations due to the charge quantization), one can also take advantage of the unique features of quantum mechanics (e.g in the context of quantum computation). A detailed understanding of these effects is therefore necessary not only from the point of view of fundamental physics knowledge, but also for the technological design of future devices.

Mesoscopic physics, as a subfield of condensed matter physics, studies electrical properties of systems with typical dimensions at the borderline between the macroscopic scale of the world we live in, and the microscopic scale in which each atom is separately considered. The confining potential in these structures changes over length scales comparable with the electron wavelength, such that states are quantized. But at the same time devices contain a large number of atoms such that statistical properties (e.g. temperature and distribution function) still have meaning. Extensive studies, both theoretical and experimental, in the field of mesoscopic physics, over the last two decades, have lead to a better understanding for the phenomena taking place in these low dimensional devices (typical dimensions between 10 nm and 10 μm).

Conductance studies are widely used to obtain information about electronic transport properties, by measuring the current (average amount of charge transferred in a unit of time) for an applied voltage bias. At the same time, the fluctuations in time of a measured quantity can provide important information that is not present in the time-averaged value. As an example, noise is routinely

used nowadays in quantum optics to study photon statistics. Current fluctuations due to the discreteness of the electrical charge are known as shot noise. This was first discovered in classical systems (vacuum tubes) by W. Schottky in 1918. In mesoscopic physics, the time dependent current fluctuations, can provide important information regarding carrier interactions, effective charge of carriers, particle statistics [6].

1.3 Thesis Layout

The thesis presents results on the detection of shot noise at very high frequencies. To achieve this, we implemented new techniques for noise measurements, by coupling on chip the detector and the device under study. The detector rectifies an incident fluctuating signal, generated by the device, into a DC signal which is much easier to measure using standard DC techniques. We benefit from a large detection bandwidth and a good coupling, resulting in a high sensitivity for the noise detection. These detection schemes are used to measure noise generated by devices such as Josephson junction, Cooper pair box, quantum dot in a carbon nanotube, quantum point contact formed in a 2 dimensional electron gas. The thesis is organized as follows:

Chapter 2: Noise concepts are briefly introduced, together with some of the systems used in this thesis: quantum dots, Josephson junctions, 2 dimensional electron gas structures, carbon nanotubes. Several existing detection techniques are discussed, for a comparison with the high frequency ones demonstrated in this thesis.

Chapter 3: We employ an superconductor-insulator-superconductor (SIS) junction to measure high frequency noise in the current of a quantum device. The detector and device are capacitively coupled on chip. This allows noise detection over a large bandwidth (up to several 100 GHz, depending on the superconducting material). We detect the noise generated by another SIS junction. Using the AC Josephson effect we perform frequency resolved measurements up to 100 GHz with Al as superconductor. At higher biases we measure shot noise due to quasiparticle current. Non-symmetric emission noise is measured using a sub-gap biased detector.

Chapter 4: We measure the current fluctuations arising from coherent charge oscillations in a two-level system, a superconducting charge qubit. For the de-

tection we use a superconductor-insulator-superconductor tunnel junction as an on chip spectrum analyzer for high-frequency fluctuations. A narrow band peak is observed in the spectral noise density at the frequency of the coherent charge oscillations.

Chapter 5: The SIS on chip detection scheme is used to detect noise generated by a quantum dot formed in a single wall carbon nanotube. Measurement of shot noise over a full Coulomb diamond is reported with excited states and inelastic cotunneling clearly visible. Super-Poissonian noise is detected, for the first time, in the case of inelastic cotunneling.

Chapter 6: Presents an experimental realization of a Quantum Dot (QD), operated as a high-frequency noise detector. This is demonstrated by measuring shot noise produced in a nearby Quantum Point Contact (QPC). Current fluctuations in the QPC ionize the QD and are detected this way. We investigate the dependence of detector signal on the QPC transmission and voltage bias and observe that results are consistent with previous low-frequency measurements. We also observe and explain quantum threshold feature and saturation in the detector signal. This experimental work is also relevant in understanding the backaction of a QPC used as a charge detector.

References

- [1] G. E. Moore, *Electronics* **38** (1965).
- [2] R. P. Feynman, *The Feynman Lectures on Physics*, Vol.3 (Addison Wesley, 1970).
- [3] M. Riebe, H. Häffner, C. F. Roos, W. Hänsel, J. Benhelm, G. P. T. Lancaster, T. W. Körber, C. Becher, F. Schmidt-Kaler, D. F. V. James, and R. Blatt, *Nature* **429**, 734 (2004).
- [4] M. D. Barrett, J. Chiaverini, T. Schaetz, J. Britton, W. M. Itano, J. D. Jost, E. Knill, C. Langer, D. Leibfried, R. Ozeri, and D. J. Wineland, *Nature* **429**, 737 (2004).
- [5] R. P. Feynman, *The Feynman Lectures on Computation*, edited by R. W. Allen and T. Hey (Perseus Publishing, 2000).
- [6] Y. M. Blanter and M. Büttiker, *Phys. Rep.* **336**, 1 (2000).

Chapter 2

Noise Concepts. Systems used.
Measurement techniques

2.1 Sources of Noise

Noise represents spontaneous, random fluctuations (deviations) of physical quantities in time, away from a mean value. These are stochastic (random) processes and are a manifestation of the thermal motion of matter and the discreteness of its structure.

For electrical systems, not all sources of noise are inherent to the device or to the electron transport processes. These generate extrinsic noise and can be reduced or even eliminated (e.g. by employing better fabrication technologies [1]). In this case the study of noise can help developing better quality devices. Intrinsic noise is characteristic to the device. This can not be reduced and sets an upper limit for the accuracy that can be achieved in the measurements. For quantum systems, the presence of noise in the environment can represent an important source of decoherence. From this point of view, intrinsic noise can be regarded as a nuisance.

But, at the same time, the study of electrical fluctuations is an important tool to investigate the electronic properties of mesoscopic devices [2]. If we consider the electrical current through such a device, the intrinsic fluctuations contain information about the interactions that are regulating the transport. The temporal dependence of the current, $I(t)$, is not a straight line, but exhibits small fluctuations $\Delta I(t) = I(t) - \bar{I}$ around the mean value \bar{I} (see Fig. 2.1). To characterize noise the current-current correlator is defined as

$$C(\tau) \equiv \langle \Delta I(\tau + t) \Delta I(t) \rangle \quad (2.1)$$

and the power spectral density (the power of noise per unit of frequency)

$$S_I(\omega) \equiv \int_{-\infty}^{+\infty} d\tau e^{i\omega\tau} C(\tau) = \int_{-\infty}^{+\infty} d\tau e^{i\omega\tau} \langle \Delta I(\tau) \Delta I(0) \rangle \quad (2.2)$$

is the Fourier transform of the correlator. The brackets denote an ensemble average over identical systems or over the initial time t (system is assumed ergodic). For this classical case $C(t)$ is real and symmetric, i.e. $C(t) = C(-t)$, and so is the power density $S_I(\omega) = S_I(-\omega)$. It is enough, therefore, to consider a symmetrized spectrum

$$S_I^{sym}(\omega) = S_I(\omega) + S_I(-\omega) = 2 \int_{-\infty}^{+\infty} d\tau e^{i\omega\tau} C(\tau) \quad (2.3)$$

defined for positive frequencies ω . This is also the quantity that is detected in standard, low frequency noise measurements.

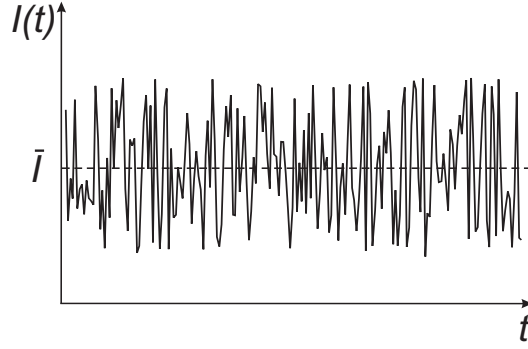


Figure 2.1: Time dependent fluctuations for the current through a mesoscopic device.

In the quantum limit, the spectrum is no longer symmetric $S_I(\omega) \neq S_I(-\omega)$ and this classical description is not valid anymore. The quantum case is discussed later in this Section.

There are more sources which can induce electrical noise (voltage or current fluctuations) in mesoscopic systems. In the following I will discuss several limits and the dominant noise mechanisms associated with them. Here we need to consider three energy scales: the thermal energy $k_B T$, the energy associated with the frequency of interest $\hbar\omega$ and the energy eV provided by the device voltage bias. Depending on the relation between these three energy scales, three limit cases for the noise exist.

2.1.1 Thermal Noise

At non-zero temperature, thermal fluctuations in the occupation number of the leads cause current fluctuations in the external circuit. These are equilibrium fluctuations ($V = 0$), also known as thermal or Johnson-Nyquist noise. In the limit $k_B T \gg eV, \hbar\omega$ thermal noise dominates over other types of noise. The power spectrum is white (i.e. frequency independent) up to a frequency $\omega = k_B T / \hbar$, where the quantum limit is reached. The magnitude of the noise power is directly related to the system conductance G

$$S_I^{symm} = 4k_B T G \quad (2.4)$$

This is known as the Johnson-Nyquist relation [3, 4] and can be regarded as a formulation of the fluctuation-dissipation theorem. Thus measurements of equilibrium fluctuations provide no additional information besides AC conductance measurements.

2.1.2 Shot Noise

Out of equilibrium, when current is passed through a conductor, shot noise is generated as a consequence of charge quantization. Incident charge quanta are randomly transmitted or reflected in the conductor, giving rise to current fluctuations. Because of this shot noise is also known as partition noise. The power spectrum is white and, in the strong backscattering limit, is proportional to the average current \bar{I} .

Shot noise has a dominant contribution for $eV \gg k_B T, \hbar\omega$. If we consider electrons incident to a potential barrier with a transmission probability t , the power density of the partition noise can be expressed [5]

$$S_I^{sym} = 2e\bar{I}(1 - t) \quad (2.5)$$

For a small transmission probability, $t \rightarrow 0$, the transfer of electrons is random (completely uncorrelated), and is described in time by a Poissonian distribution. In this case shot noise is called Poissonian and for the power we recover the Schottky formula [6]

$$S_I^{sym} = 2e\bar{I} \quad (2.6)$$

Interactions in mesoscopic systems can introduce correlations in the charge transport, resulting in a reduction of noise. Deviations from the Poissonian value are expressed by the Fano factor F defined as $F = S_I^{sym}/2e\bar{I}$. Pauli exclusion principle leads to a shot noise reduction when transport is ballistic (no scattering), e.g. in case of open channels of a quantum point contact (QPC) [7, 8]. The investigation of this reduction in an atomic size QPC provides information regarding the number of open channels and their transmission (the 'mesoscopic PIN code') [9]. Shot noise can also be suppressed when Coulomb interaction regulates the charge transfer. This was measured in the case of transport through a quantum dot [10, 11].

For systems in which current is not carried in units of electron charge (e.g. in the case of fractional Hall effect or in superconductors), the general formula for the shot noise power becomes $S_I^{sym} = F2q\bar{I}$. Here, the electron charge e is replaced by an effective charge q . Shot noise measurements performed in the fractional quantum Hall regime allowed the observation of the fractional charge corresponding to the quasiparticles [12, 13, 14]. In case of superconductor-normal metal junctions, a shot noise enhancement by a factor 2 was observed [15]. This is attributed to a $q = 2e$ effective charge transfer in Andreev reflection processes.

Shot noise measurements can also be employed to probe particle statistics. Bosons emitted by a thermal source tend to bunch (more of them are emitted at

the same time) resulting in a super-Poissonian statistics [16]. Due to the Pauli principle, a fermionic thermal source emits particles separately (anti-bunching) leading to sub-Poissonian statistics [17]. When such a generated stream of particles (bosons or fermions) is separated at a beam splitter, the correlations between the two outgoing streams are affected by the nature of particles. By using a Hanbury Brown and Twiss (HBT) geometry, positive correlations were measured in case of photons [16, 17, 18] and negative correlations for electrons [19, 20].

In macroscopic systems shot noise is not present, as current fluctuations are averaged out by electrons transferred through multiple transport channels.

2.1.3 Quantum Noise

In the quantum limit ($\hbar\omega \gg k_B T$), zero point fluctuations (ZPF) in the device introduce an asymmetry in the spectrum $S(\omega) \neq S(-\omega)$. The symmetrized approach is not valid anymore and the two sides of the power density need to be considered separately. In definitions (2.1) and (2.2), $I(t)$ is replaced by the time dependent current operator in the Heisenberg representation $\hat{I}(t) = \exp(i\hat{H}t/\hbar)\hat{I}\exp(-i\hat{H}t/\hbar)$, with \hat{H} being the time independent Hamiltonian of the system. The average is replaced by the quantum statistical expectation for the operator product and definition (2.1) becomes

$$C(\tau) \equiv \langle \Delta \hat{I}(\tau + t) \Delta \hat{I}(t) \rangle \equiv \sum_i \rho_{ii} \langle i | \Delta \hat{I}(\tau) \Delta \hat{I}(0) | i \rangle \quad (2.7)$$

Here ρ_{ii} is the diagonal element in the density matrix corresponding to the system eigen state $|i\rangle$. The current operators $\hat{I}(t)$ at different times do not commute and the correlator has a complex value, which satisfies the relation $C(\tau) = C(-\tau)^*$. The power density is now defined as

$$S(\omega) \equiv \int_{-\infty}^{+\infty} d\tau e^{i\omega\tau} C(\tau) = \int_{-\infty}^{+\infty} d\tau e^{i\omega\tau} \langle \Delta \hat{I}(\tau) \Delta \hat{I}(0) \rangle \quad (2.8)$$

We can insert the identity operator $\sum_f |f\rangle\langle f|$ and write

$$S(\omega) = \int_{-\infty}^{+\infty} d\tau e^{i\omega\tau} \sum_{i,f} \rho_{ii} \langle i | \hat{I}(\tau) | f \rangle \langle f | \hat{I}(0) | i \rangle \quad (2.9)$$

$$= 2\pi\hbar \sum_{i,f} \rho_{ii} |\langle i | \hat{I} | f \rangle|^2 \delta(E_f - E_i - \hbar\omega). \quad (2.10)$$

A clear physical interpretation for $S(\omega)$ can be reached if we assume the system (noise source) is coupled to a measuring device (detector). We consider this detector to be a quantum device where only the two lowest energy levels play

a role. These are the ground $|0\rangle$, respectively the excited state $|1\rangle$, separated by an energy $E_{01} = \hbar\omega_{01}$. Current fluctuations through the source, generate a perturbation potential $V_{perturb}(t) = A I(t)$ at the detector and induce a transition between the two levels. The coupling constant A is considered to be small. The transition rates can be expressed as [21]

$$\Gamma_{\uparrow} = \frac{A^2}{\hbar^2} S(-\omega_{01}) \quad (2.11)$$

$$\Gamma_{\downarrow} = \frac{A^2}{\hbar^2} S(\omega_{01}) \quad (2.12)$$

with Γ_{\uparrow} the rate for exciting the detector from ground to the excited state, respectively Γ_{\downarrow} the decay rate from the excited state into the ground state. Combining equations (2.10) - (2.12) we recover the well known Fermi golden rule. The power density $S(\omega)$ is proportional to the energy transfer rate between the system and the measuring device. Terms with $E_i > E_f$ describe transitions in which an energy of $-\hbar\omega = E_i - E_f > 0$ is transferred from the system to the measuring device, while terms with $E_f > E_i$ describe transitions in which $\hbar\omega = E_f - E_i > 0$ energy is transferred from the measuring device to the system. So we can conclude that $S(-\omega)$ describes the *emission* spectrum, while $S(\omega)$ corresponds to the *absorption* spectrum.

As we mentioned already, the asymmetry in the spectrum is caused by the presence of ZPF. If the system is in equilibrium at zero temperature, no energy is available for emission and subsequently $S(-\omega) = 0$. But, the presence of ZPF irrespective of the temperature, ensures that the system can always absorb energy and therefore $S(\omega) \neq 0$. The asymmetry is important also at finite voltage biases V and temperatures T , as long as the condition $\hbar\omega \gg eV, k_B T$ is valid.

If the system is in equilibrium, at temperature T , the power density obeys the detailed balance relation [22]

$$S(\omega) = e^{\hbar\omega/k_B T} S(-\omega) \quad (2.13)$$

In the limit of low frequencies $\hbar\omega \ll k_B T$ we recover the classical case relation $S(\omega) = S(-\omega)$.

In principle it is possible to measure separately the two sides of the spectrum, but for this a special detector is needed [21, 23, 24]. This *quantum spectrum analyzer* must be able to discern between emission and absorption processes. To measure the emission part $S(-\omega)$, the detector needs to be passive and return a signal only if energy is transferred from the noise source. Conversely, for the measurement of the absorption spectrum, the noise source needs to be in the ground state and absorb energy from an active detector. The detector is thus deexcited and measures the $S(\omega)$ side.

An example of such a quantum detector is the two level system considered before. This can be prepared in the ground or the excited state and then weakly coupled to the noise source. By measuring the occupation probabilities of the two states as a function of time, the transition rates Γ_{\uparrow} and Γ_{\downarrow} can be determined. These are directly related to the two-sided power spectrum (see equations (2.11), (2.12)).

To illustrate the interplay between the three types of noise discussed so far, we consider a simple conductor with a conductance G , at a temperature T . If a voltage bias V is applied, the non-symmetrized expression for the current power density can be written

$$S(\omega) = G \left[\frac{\hbar\omega + eV}{1 - \exp\left(-\frac{\hbar\omega + eV}{k_B T}\right)} + \frac{\hbar\omega - eV}{1 - \exp\left(-\frac{\hbar\omega - eV}{k_B T}\right)} \right] \quad (2.14)$$

This is reduced to simpler expressions in several limit cases.

Thus, if the energy provided by the voltage bias is much larger than $\hbar\omega$ and $k_B T$ we recover the frequency independent expression for shot noise

$$S = eVG = eI. \quad (2.15)$$

We recall here that the familiar Schottky formula refers to the symmetrized power density and reads $S^{sym} = 2eI$.

At equilibrium ($V = 0$) equation (2.14) becomes

$$S(\omega) = \frac{2\hbar\omega G}{1 - e^{-\hbar\omega/k_B T}} \quad (2.16)$$

valid for both positive and negative frequencies ω .

At low frequencies, if $k_B T \gg \hbar\omega$, thermal noise dominates and we recover the Johnson formula

$$S = 2k_B T G. \quad (2.17)$$

The spectrum is white and for the symmetrized case we can write $S^{sym} = 4k_B T G$.

In the quantum limit $\hbar\omega \gg k_B T$, the spectrum is asymmetric

$$S(\omega) = 2\hbar\omega G \Theta(\omega). \quad (2.18)$$

and the step function $\Theta(\omega)$ expresses the fact that, in the zero temperature case, the conductor can only absorb energy and no energy is available for emission.

2.1.4 1/f Noise

These types of fluctuations are caused by slow changes in the device resistance and they are found in most conducting materials. Their spectrum is proportional to the square of the injected DC current and increases as an inverse power of the frequency. Hence the name 1/f noise (also known as flicker noise).

The variations in the resistance are generally due to random motion of ionized impurities or scatterers between two locally stable positions. If the dimensions of a conductor are increased and therefore also number of individual fluctuators, the noise spectrum changes from one Lorentzian or a superposition of few Lorentzians to a continuous 1/f noise. Although many studies are available, because of the great variability of the systems in which these fluctuations occur, no universal mechanism for the 1/f noise exists.

1/f noise dominates at low frequencies and is strongly suppressed as frequency is increased (typically above several kHz). These types of fluctuations are not addressed in this thesis and they are eliminated in the measurements by working at much higher frequencies (in the GHz range). For more extensive reviews of 1/f noise studies see [1], [25].

2.2 Systems Used. Sample Fabrication

In this section, the systems used in the thesis for noise measurements are briefly introduced. Several techniques employed for sample fabrication are also presented here.

2.2.1 Josephson Junctions

A Josephson junction is made up of two superconducting electrodes with a non-superconducting barrier in between. The barrier is formed by a thin layer of conducting or insulating material. Superconducting circuits with Josephson junctions are widely used to study quantum mechanical effects. Josephson junctions are also used to build fast electronic switches (rapid single flux quantum - RSFQ) or sensitive magnetic field sensors (superconducting quantum interference devices - SQUID).

The supercurrent passing through a short-circuited Josephson junction ($V = 0$ bias voltage) can be written [26]

$$I_S = I_C \sin \varphi \quad (2.19)$$

with φ the superconducting phase difference across the junction. The critical current I_C represents the maximum value the supercurrent can achieve. This

gives an indication about the coupling between the two superconductors and is an important phenomenological parameter of the junction. So, even when there is no voltage drop across the junction a DC supercurrent flows through the insulator layer. This is known as the DC Josephson effect.

If a finite voltage V is applied between the superconductor electrodes, equation (2.19) is still valid but with a phase difference φ which evolves in time

$$\frac{\partial \varphi}{\partial t} = \frac{2e}{\hbar} V \quad (2.20)$$

Thus, for DC voltage bias V , a rapid alternating AC current $I_S = I_C \sin \omega t$ occurs within the insulator, at a frequency $\omega = 2eV/\hbar$. This is called the AC Josephson effect.

Besides I_S , additional contributions to the total current can be considered. At high frequencies, the capacitance of the junction, C , will lead to a displacement current $I_C = C dV/dt$. At the same time the quasiparticle contribution I_N can be written as $I_N = V/R$. Here R represents a resistance which depends strongly on the junction parameters, the temperature, T , and the bias voltage, V . This is called the resistively and capacitively shunted junction model (RCSJ) and for a current biased junction we can write

$$I_{bias} = \frac{\hbar C}{2e} \frac{d^2 \varphi}{dt^2} + \frac{\hbar}{2eR} \frac{d\varphi}{dt} + I_C \sin \varphi \quad (2.21)$$

Depending on parameters, the dynamic of the junction can be hysteretic (underdamped junction) or non-hysteretic (overdamped junction). When the bias voltage is larger than $2\Delta/e$, quasiparticle tunneling gives the main contribution and we recover what is called the normal state resistance of the junction.

Sample Fabrication

The advance of lithographic techniques permits nowadays reliable fabrication of small Josephson junctions with controllable parameters. Electron beam lithography with a standard angle evaporation technique was employed to fabricate Al based Josephson junctions.

The main steps of the fabrication procedure are schematically shown in Fig. 2.2. Samples are fabricated on a Si substrate with a 200 nm thick SiO_2 insulating layer on top. First two organic resist layers are spun: PMMA/MAA copolymer in ethyl-lactate respectively PMMA solved in chlorobenzene. We bake the substrate at 140°C for 30 minutes and then the sample pattern is written using a focussed electron beam (Fig. 2.2 a). This breaks the polymer chains in the resist and the exposed parts can be subsequently removed by developing the sample

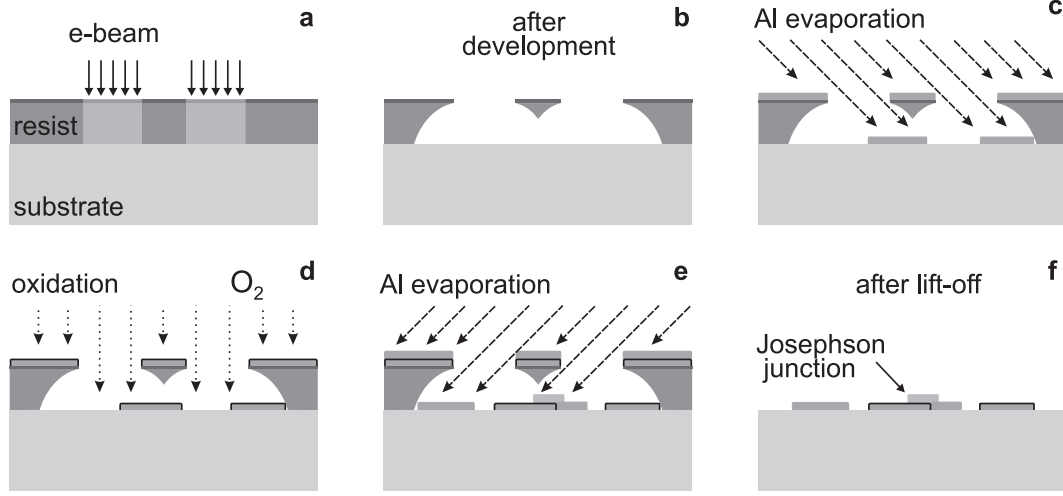


Figure 2.2: Schematic drawing of the fabrication steps for Josephson junctions.

for 90 s in a 1:3 solution of MIBK and iso-propanol. Electrons backscattered at the substrate interface and a lower molecular mass cause the bottom resist to be developed faster than the top one. The carved undercut can create suspended bridges as the one shown in Fig. 2.2b. The ends of this bridge are sustained by undeveloped resist located out of the paper plane. The first layer of Al (30 nm thick) is evaporated under an angle α (typically $\approx 12^\circ$) as shown in Fig. 2.2c. An insulating layer of Al_2O_3 is then formed by exposing the sample to a 35 mT atmosphere of pure O_2 for 5 minutes. A second Al layer (50 nm thick) is then deposited under an angle $-\alpha$ (Fig. 2.2e). At the region where the two Al layers overlap a small Josephson junction is formed. In the last ‘lift-off’ step acetone is used to remove the undeveloped resist together with the metal on top of it. After this, only the designed superconducting circuit, comprising the Josephson junctions, is left on the substrate (see Fig. 2.2f).

2.2.2 Quantum Dots

A quantum dot is simply a small box that can be filled with electrons. The box is coupled via tunnel barriers to a source and drain reservoir, with which particles can be exchanged (see Fig. 2.3). By attaching current and voltage probes to these reservoirs, we can measure the electronic properties of the dot. The dot is also coupled capacitively to one or more ‘gate’ electrodes, which can be used to tune the electrostatic potential of the dot with respect to the reservoirs. When the size of the dot is comparable to the wavelength of the electrons that occupy it, the system exhibits a discrete energy spectrum, resembling that of an atom. As

a result, quantum dots behave in many respects as *artificial atoms* [27].

A quantum dot is a general kind of system and many different sizes and materials can be used to realize it: single molecules trapped between electrodes, metallic or superconducting nanoparticles, self-assembled quantum dots, semiconductor lateral or vertical dots, semiconducting nanowires or carbon nanotubes between closely spaced electrodes. In this thesis, we study two types of quantum dots: carbon nanotube based quantum dots[28, 29] and lateral (gated) semiconductor quantum dots [30].

Electronic properties of quantum dots are conveniently understood using the constant interaction (CI) model [30]. This makes two important assumptions. First, the Coulomb interactions among electrons in the dot, and between electrons in the dot and those in the environment, are parameterized by a single, constant capacitance, C . This capacitance can be thought of as the sum of the capacitances between the dot and the source, C_S , the drain, C_D , and the gate, C_g : $C = C_S + C_D + C_g$. Second, the discrete energy spectrum can be described independently of the number of electrons on the dot. Under these assumptions the total energy of a N -electron dot in the ground state with the source-drain voltage, V_{SD} , applied to the source (and the drain grounded), is given by

$$U(N) = \frac{[-|e|(N - N_0) + C_S V_{SD} + C_g V_g]^2}{2C} + \sum_{n=1}^N E_n \quad (2.22)$$

where $-|e|$ is the electron charge and N_0 the number of electrons in the dot at zero gate voltage, which compensates the positive background charge originating from the donors in the heterostructure. The terms $C_S V_{SD}$ and $C_g V_g$ represent the charge on the dot that is induced by the bias voltage, respectively by the gate voltage, V_g . The last term of Eq. (2.22) is a sum over the occupied single-

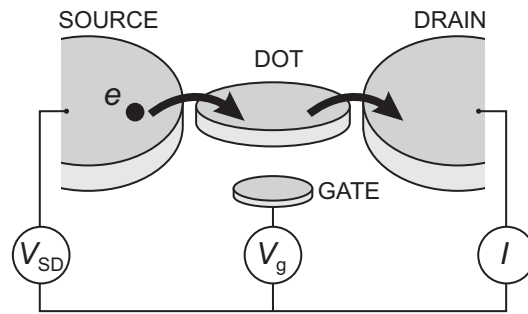


Figure 2.3: Schematic picture of a quantum dot (represented by a disk), connected to source and drain contacts via tunnel barriers, allowing the current through the device, I , to be measured in response to a bias voltage, V_{SD} and a gate voltage, V_g .

particle energy levels E_n . These energy levels depend on the characteristics of the confinement potential.

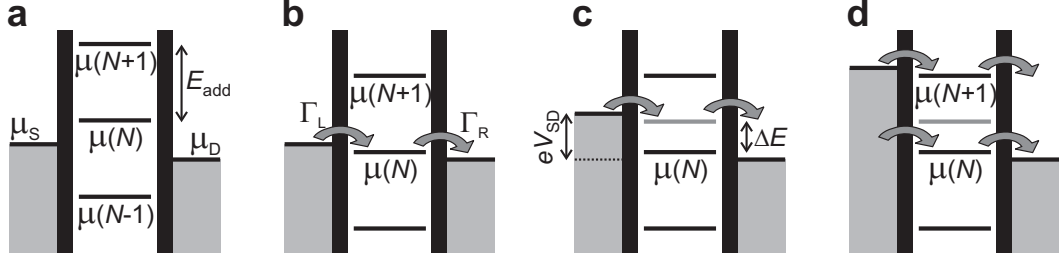


Figure 2.4: Schematic diagrams of the electrochemical potential of the quantum dot for different electron numbers. **(a)** No level falls within the bias window between μ_S and μ_D , so the electron number is fixed at $N - 1$ due to Coulomb blockade. **(b)** The $\mu(N)$ level is aligned, so the number of electrons can alternate between N and $N - 1$, resulting in a single-electron tunneling current. The magnitude of the current depends on the tunnel rates between the dot and the reservoirs Γ_L and Γ_R . **(c)** Both the ground-state transition between $N - 1$ and N electrons (black line), as well as the transition to an N -electron excited state (gray line) fall within the bias window and can thus be used for transport (though not at the same time, due to Coulomb blockade). This results in a current that is different from the situation in (b). **(d)** The bias window is so large that the number of electrons can alternate between $N - 1$, N and $N + 1$, i.e. two electrons can tunnel, onto and out of the dot, at the same time.

To describe transport experiments, it is often more convenient to use the electrochemical potential. This is by definition the energy required for adding the N th electron to the dot:

$$\begin{aligned}\mu(N) &\equiv U(N) - U(N - 1) = \\ &= (N - N_0 - \frac{1}{2})E_C - \frac{E_C}{|e|}(C_S V_{SD} + C_g V_g) + E_N\end{aligned}\quad (2.23)$$

where $E_C = e^2/C$ is the charging energy. This expression denotes the transition between the N electrons ground state and $N - 1$ electrons ground state.

The electrochemical potential for the transitions between ground states with a different electron number N is shown in Fig. 2.4a. The discrete levels are spaced by the so-called addition energy:

$$E_{add}(N) = \mu(N + 1) - \mu(N) = E_C + \Delta E. \quad (2.24)$$

The addition energy consists of a purely electrostatic part, the charging energy E_C , plus the energy spacing between two discrete quantum levels, ΔE . Note

that ΔE can be zero, when two consecutive electrons are added to the same spin-degenerate level.

Of course, for transport to occur, energy conservation needs to be satisfied. This is the case when an electrochemical potential level falls within the ‘bias window’ between the electrochemical potential (Fermi energy) of the source (μ_S) and the drain (μ_D), i.e. $\mu_S \geq \mu \geq \mu_D$ with $-|e|V_{SD} = \mu_S - \mu_D$. Only then can an electron tunnel from the source onto the dot, and then tunnel off to the drain without losing or gaining energy. The important point to realize is that since the dot is very small, it has a very small capacitance and therefore a large charging energy – for typical dots $E_C \approx$ a few meV. If the electrochemical potential levels are as shown in Fig. 2.4a, this energy is not available (at low temperatures and small bias voltage). So, the number of electrons on the dot remains fixed and no current flows through the dot. This is known as Coulomb blockade.

The Coulomb blockade can be lifted by changing the voltage applied to the gate electrode and thus shifting the whole ‘ladder’ of electrochemical potential levels up or down. When a level falls within the bias window, the current through the device is switched on. In Fig. 2.4b the electron number alternates between $N - 1$ and N . This means that the N th electron can tunnel onto the dot from the source. Only after it tunnels off to the drain can another electron come onto the dot again from the source. This cycle is known as single-electron tunneling.

By sweeping the gate voltage and measuring the current, we obtain a trace as shown in Fig. 2.5a. At the positions of the peaks, an electrochemical potential level is aligned with the source and drain and a single-electron tunneling current

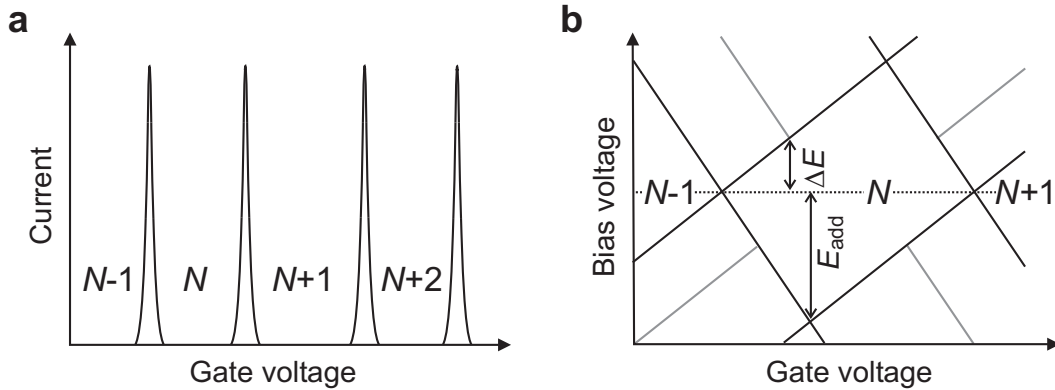


Figure 2.5: Transport through a quantum dot. (a) Coulomb peaks in current versus gate voltage in the linear-response regime. (b) Coulomb diamonds in differential conductance, dI/dV_{SD} , versus V_{SD} and V_g , up to large bias. The edges of the diamond-shaped regions (black) correspond to the onset of current. Diagonal lines emanating from the diamonds (gray) indicate the onset of transport through excited states.

flows. In the valleys between the peaks, the number of electrons on the dot is fixed due to Coulomb blockade. The distance between the peaks corresponds to $E_C + \Delta E$, and can therefore give information about the energy spectrum of the dot.

A second way to lift Coulomb blockade is by changing the source-drain voltage, V_{SD} (see Fig. 2.4c). This increases the bias window and also ‘drags’ the electrochemical potential of the dot along, due to the capacitive coupling to the source. Again, a current can flow only when an electrochemical potential level falls within the bias window. When V_{SD} is increased so much that both the ground state as well as an excited state transition fall within the bias window, there are two paths available for electrons tunneling through the dot. In general, this will lead to a change in the current, enabling us to perform energy spectroscopy of the excited states. How exactly the current changes depends on the tunnel rates of the two paths [31].

Usually, the current or differential conductance (the derivative of the current with respect to the source-drain bias) is measured while sweeping the bias voltage, for a series of different values of the gate voltage. Such a measurement is shown schematically in Fig. 2.5 b. Inside the diamond-shaped region, the number of electrons is fixed due to Coulomb blockade, and no current flows. Outside the diamonds, Coulomb blockade is lifted and single-electron tunneling can take place (or for larger bias voltages even double-electron tunneling is possible, see Fig. 2.4 d). Excited states are revealed as changes in the current, i.e. as peaks or dips in the differential conductance. From such a ‘Coulomb diamond’ the energy of excited states as well as the charging energy can be read off directly.

The simple model described above explains successfully how quantization of charge and energy leads to effects like Coulomb blockade and Coulomb oscillations. Nevertheless, it is too simplified in many respects. For instance, the model considers only first-order tunneling processes, in which an electron tunnels first from one reservoir onto the dot, and then from the dot to the other reservoir. But when the tunnel rates between the dot and the leads, are increased, higher-order tunneling via virtual intermediate states becomes important. Such processes are known as ‘cotunneling’. Furthermore, the simple model does not take into account the spin of the electrons, thereby excluding for instance exchange effects.

2.2.3 Semiconductor 2DEG Structures

Fabrication of lateral gated quantum dots starts with a semiconductor heterostructure, a sandwich of different layers of semiconducting material (see Fig. 2.6a). These layers, in our case GaAs and AlGaAs, are grown on top of each other us-

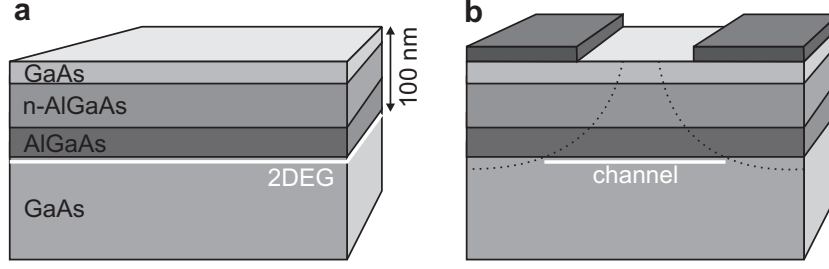


Figure 2.6: Confining electrons in a semiconductor. **(a)** Semiconductor heterostructure containing a 2DEG (indicated in white) approximately 100 nm below the surface, at the interface between GaAs and AlGaAs. The electrons in the 2DEG result from Si donors in the n-AlGaAs layer. (The thickness of the different layers is not to scale.) **(b)** By applying negative voltages to the metal electrodes on the surface of the heterostructure, the underlying 2DEG can be locally depleted. In this way, electrons can be confined to one or even zero dimensions.

ing molecular beam epitaxy (MBE), resulting in very clean crystals. By doping the n-AlGaAs layer with Si, free electrons are introduced. These accumulate at the interface between GaAs and AlGaAs, typically 100 nm below the surface, forming a two-dimensional electron gas (2DEG) – a thin (~ 10 nm) sheet of electrons that can only move along the interface. The 2DEG can have a high mobility and relatively low electron density (typically $10^5 - 10^6$ cm²/Vs and $\sim 3 \times 10^{15}$ m⁻², respectively). The low electron density results in a large Fermi wavelength (~ 40 nm) and a large screening length, which allows us to locally deplete the 2DEG with an electric field. This electric field is created by applying (negative) voltages to metal gate electrodes on top of the heterostructure (Fig. 2.6b).

These electrodes are fabricated using electron beam lithography as already discussed in the previous section. Here the metal gates are evaporated perpendicularly and the undercut is not crucial. Therefore only one layer of organic resist (PMMA) is used. The gates consist of a Ti ‘sticking’ layer (10 nm thick) with an Au layer on top (20 nm thick).

By applying negative voltages to the gates, the 2DEG is locally depleted, creating one or more small islands that are isolated from the large 2DEG reservoirs. These islands are the quantum dots. In order to probe them, we need to make electrical contact to the reservoirs. For this, we evaporate AuGeNi on the contact pads and anneal at ~ 440 degrees Celsius for 60 seconds. This forms ohmic contacts with a resistance of about 1 k Ω that connect the 2DEG source and drain reservoirs electrically to metal bonding pads on the surface. Metal wires bonded to these pads run toward the current or voltage probes, enabling us to perform transport measurements.

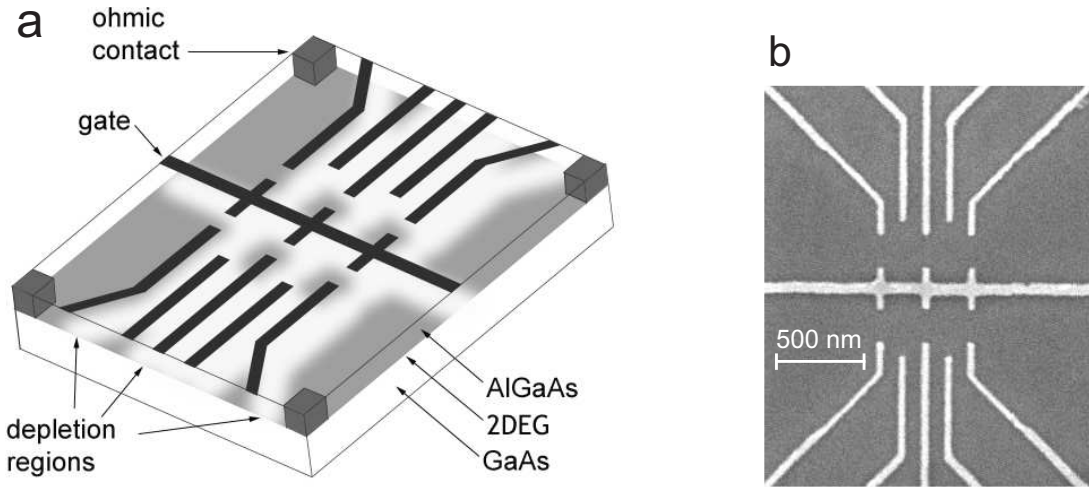


Figure 2.7: Lateral quantum dot device defined by metal surface electrodes. **(a)** Schematic view of a device. Negative voltages applied to metal gate electrodes (black) lead to depleted regions (white) in the 2DEG (gray). In this example four quantum dots (the gray spots) are formed by using all the top gates. Ohmic contacts (dark gray columns) enable bonding wires (not shown) to make electrical contact to the 2DEG reservoirs. **(b)** Scanning electron microscope image of an actual device, showing the gate electrodes (light gray) on top of the surface (dark gray). Appropriate voltages applied to the gates can define either quantum dots or quantum point contacts as will be explained in chapter 6 (Device fabricated by L. H. Willems van Beveren and R. Hanson at NTT Basic Research Labs.)

2.2.4 Carbon Nanotubes

Carbon nanotubes are small molecules, with a hollow cylindrical shape, made up of only carbon atoms. Since their discovery in 1991 by Sumio Iijima [32], numerous studies proved that they have outstanding mechanical and electrical properties.

A convenient way to visualize carbon nanotubes is to consider a sheet with a hexagonal lattice of Carbon atoms (graphene) which is rolled up and forms a cylinder. From the mechanical point of view, this confers carbon nanotubes a high mechanical stiffness and a good flexibility, at the same time. Thus, despite being lightweight, they are one of the strongest materials known, with a Young modulus in the range of TPa [33]. They are also extremely flexible: if strongly bent they form a buckle, completely reversible when tension is released. As an application, the small size and the excellent flexibility make carbon nanotubes very well suited for atomic force microscope tips.

Carbon nanotubes have also exceptional electrical properties and constitute ideal building blocks in a ‘bottom-up’ approach for building ultra-small electronics. They can be either metallic or semiconducting, depending on their chirality (how the graphene sheet is wind) and on their diameter. Theoretical predictions in this sense were confirmed by scanning tunneling microscopy (STM) measurements [34].

Electronic transport measurements in carbon nanotubes can be used not only to study their properties, but also to understand fundamental physical phenomena. For instance metallic nanotubes can be considered as one-dimensional conductors ideal for the study of Luttinger liquid behavior [35]. If closely spaced contacts are attached to a carbon nanotube, confinement is introduced in the remaining dimension and quantum dot is formed between the barriers at the contacts. Depending on the transparency of the barriers several limits can be addressed. For opaque barriers Coulomb blockade regime is reached, at intermediate transparency Kondo effect play an important role and for highly transparent contacts superconductivity can be induced from superconducting electrodes. In chapter 5 we present shot noise measurements from a carbon nanotube quantum dot in the Coulomb blockade regime.

The fabrication procedure for the carbon nanotubes starts by defining and evaporating 100 nm thick Pt markers on a Si substrate, using standard electron beam lithography (see section 2.2.1). Markers are necessary for alinement in subsequent electron beam lithography steps and for locating the nanotubes. A second electron beam lithography step is used to deposit Mo catalyst particles. Carbon nanotubes are CVD grown [36] from the catalyst particles by heating the substrate at 900 degrees Celsius for 10 minutes in a flow of CH_4 , H_2 and Ar. An atomic force microscopy (AFM) image of the carbon nanotubes is then used to design contacts and side gates. These are fabricated in a final electron beam lithography step and are used for transport measurements.

2.3 Low Temperature Measurements

Noise measurements in quantum devices need to be performed at very low temperatures for two reasons. Both the energy resolution (smallest energy separation that can be resolved) and the sensitivity of the noise detection are limited by thermal fluctuations. To reach sub-Kelvin temperatures, we use a Leiden Cryogenics MNK126-700 dilution refrigerator, with a base temperature of 8 mK and a cooling power of about 700 μW at 100 mK.

The sample holder is mounted on a ‘cold finger’, directly connected to the base

temperature part of the fridge. The sample sits in the bore of a superconducting magnet which can generate magnetic fields up to 14 Tesla. For measurements, 20 twisted pairs of manganin wires are used to contact the sample to room temperature electronics. Half of the 40 wires have a diameter of 0.1 mm and the other half 0.2 mm, resulting in a room temperature resistance of 190 Ω , respectively 50 Ω . The choice for the material and the diameter of the wires is made in order to reduce the heat conductance. All the wires are thermally anchored, by carefully wrapping them around copper posts, at several temperature stages (4 K, 1 K, 100 mK and 10 mK). To avoid heating due to high frequency radiation, two filter stages are used. At room temperature all wires are filtered by commercial π filters with an attenuation of more than 45 dB above 100 MHz and a capacitance of 3 nF. At base temperature the wires run through ‘copper powder filters’. These are copper tubes filled with copper powder, in which 4 signal wires, with a length of about 2 meters each, are wound. The powder absorbs the high-frequency noise very effectively, leading to an attenuation of more than 60 dB from a few 100 MHz up to more than 50 GHz. This wiring results in an effective electron temperature below 200 mK, when no extra heat loads are present.

The most important parts of the measurement electronics (i.e. digital to analog convertor (DACs), the voltage and current sources, the current-to-voltage (IV) convertor and the isolation amplifier) are all built by Raymond Schouten at Delft University. They are battery powered and optically coupled to the rest of the electronic equipment. Thus, the sample is electrically isolated and a separate, clean ground is used in the measurements.

Measurements are controlled by a computer running LabView. This sends commands via a fiber link and can set 16 independent DACs to voltages between -2 and 2 V with a 16 bit resolution. The DACs are then used to control voltage or current sources with gains of 1-100 mV/V respectively 10 nA/V -10 μ A/V. For voltage measurements we use isolated amplifiers with gains between and . The IV converter has a feedback resistance that can be set between 1 M Ω and 1 G Ω , and an input resistance that is a factor 10^3 or 10^4 smaller (for ‘low noise’ or ‘low input resistance’, respectively). The voltage amplifier has a gain up to 10^4 and a high input impedance (>10 G Ω).

Finally the voltage is measured by a digital multimeter (Keithley 2700) and read by the computer via GPIB interface. Alternatively we can use a lock-in amplifier (Stanford Research 830 DSP) for synchronous measurements.

2.4 Noise Measurement Techniques

In this section I will discuss several existing techniques for shot noise measurements. This will help put our new detection methods into the present context.

2.4.1 Low frequency cross-correlation technique

Although, in the end, one is interested in the current fluctuations $\langle \Delta I_D^2 \rangle$ of a device, usually they are derived from the voltage fluctuations $\langle \Delta V_D^2 \rangle$, as the last ones are more easily measured. The conversion $\langle \Delta V_D^2 \rangle = (R_D)^2 \langle \Delta I_D^2 \rangle$ makes use of the device dynamical resistance $R_D = dV/dI$. In a conventional way, the voltage drop across the de device is amplified (using a low noise amplifier) and fed into fast Fourier transform spectrum analyzer (see Fig. 2.8a). The result is the spectral density of the total voltage fluctuations in a specific bandwidth Δf . The measured square of the total voltage noise can be expressed as

$$\langle \Delta V^2 \rangle = \langle \Delta V_D^2 \rangle + (R_D + R_L)^2 \langle \Delta I_A^2 \rangle + \langle \Delta V_A^2 \rangle + 4R_L k_B T_L \Delta f \quad (2.25)$$

with R_L and T_L the resistance, respectively, the temperature of the measurement leads; $\langle \Delta I_A^2 \rangle$, $\langle \Delta V_A^2 \rangle$ the current and the voltage noise of the amplifier (generated at the input). Therefore, to determine the noise corresponding to the device, one needs to have precise information regarding the noise characteristics of the amplifier and the temperature and resistance of the leads. For long acquisition times, the stability of these two components might pose an even bigger problem. In addition, the amplifier voltage noise $\langle \Delta V_A^2 \rangle$ has a $1/f$ noise contribution that can dominate over the sample noise at low frequencies.

To avoid these problems, a cross-correlation method can be employed [37, 38]. This makes use of two independent channels and voltage amplifiers to measure noise in parallel (see Fig. 2.8b). By multiplying the two results, uncorrelated contributions, such as the voltage noise of the amplifiers or the thermal noise in the leads, are eliminated. If we consider the configuration in Fig. 2.8b, the cross correlation signal can be written

$$\langle \Delta V_a \Delta V_b \rangle = \langle \Delta V_D^2 \rangle + R_D(R_D + R_a)^2 \langle \Delta I_a^2 \rangle + R_D(R_D + R_b)^2 \langle \Delta I_b^2 \rangle \quad (2.26)$$

Usually the wires resistance can be neglected ($R_a, R_b \ll R_D$). To determine the voltage fluctuations $\langle \Delta V_D^2 \rangle$, knowledge of amplifiers current noise is required. This, together with the exact gain for the entire measurement circuit (i.e. amplifiers, wires, filters), are determined in an initial calibration step, usually by measuring the thermal noise of the sample. Special care is required for the combination of wires and filters capacitance and sample resistance, as the RC time

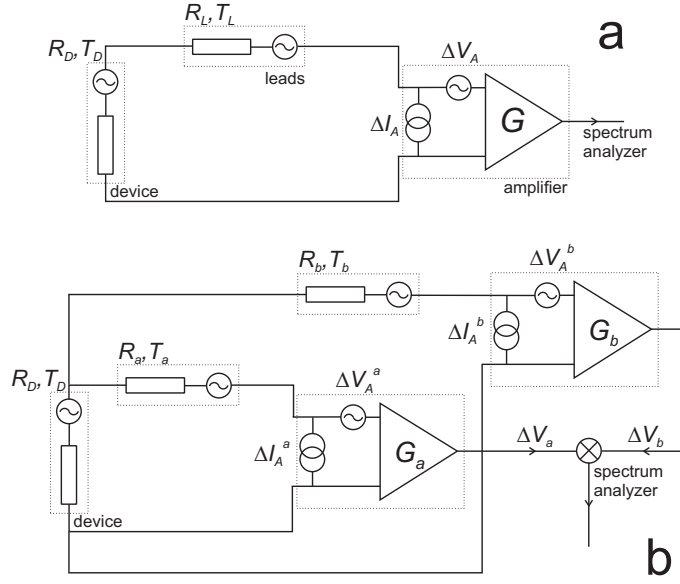


Figure 2.8: (a) Conventional noise measurement setup with one amplifier. (b) Cross correlation setup for noise measurements. Two independent channels are used in the measurement to eliminate un-correlated sources of noise (e.g. thermal noise of the wires or voltage noise at the input of the amplifiers).

of the circuit gives an upper limit $\nu_{cut-off} = (2\pi RC)^{-1}$ for the measurement frequency. At the same time cross-talk between the two measurement channels should be minimized (e.g. by using separate batteries to power the amplifiers).

After amplification, the two signals are fed into a spectrum analyzer. This calculates and averages the cross-spectrum, around a center frequency and in a certain bandwidth. The result is a frequency resolved noise spectrum for frequencies that are in the range of several kHz to several 100 kHz.

For the achieved final resolution, filtering and shielding of the measurement wires as well as the input noise of the amplifiers and the number of averages play an important role. As a numerical example, in Ref. [38] the resolution achieved is $S_V = 7.7 \times 10^{-20} \text{ V}^2/\text{Hz}$ (or 10 mK resolution on a 140 k Ω sample) after averaging for 100 s at 1 kHz.

2.4.2 Resonant scheme for noise detection at MHz frequencies

A slightly modified detection scheme is used in Ref. [13, 14] to measure the charge of quasiparticles in the fractional quantum Hall regime. The circuit is schematically presented in Fig. 2.9 and allows detection of fluctuations in the

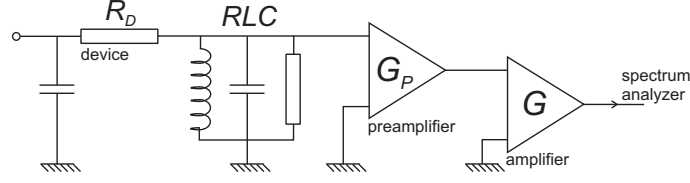


Figure 2.9: Detection scheme using a RLC resonant circuit to measure voltage fluctuations in the MHz range.

MHz range. As already mentioned, the RC time of the device-coaxial cable circuit can limit the measurement bandwidth. For typical devices ($k\Omega$ range impedance) with coaxial line connections the cut-off frequency is in the kHz range. To attain higher frequencies, authors in Ref. [13, 14] introduced an inductance in parallel to the coaxial line, forming thus an RLC resonant circuit. The capacitance is provided by the coaxial line, while the resistive part is due to the device. The impedance transforms current fluctuations of the device into voltage fluctuations at one side of the LC circuit. Frequencies centered around the resonance (at 4 MHz) are transmitted and fed into a preamplifier placed at 4.2 K. At room temperature the signal is further amplified and the power spectrum, integrated over a 100 Hz bandwidth, is calculated by the spectrum analyzer. In this case, the current noise of the preamplifier is $S^{preamp} = 1.1 \times 10^{-28} \text{ A}^2/\text{Hz}$ and gives a lower bound for the detection sensitivity.

2.4.3 High frequency detection scheme using rectifying diodes

For GHz range frequencies, two similar detection schemes are used in Ref. [7] and [21]. Instead of a spectrum analyzer, they employ rectifying diodes to measure the high frequency fluctuations. The output voltage of the diodes is proportional to the noise integrated over a certain bandwidth $\Delta\nu$: $V_{out} \propto \langle \Delta I^2 \rangle_{\Delta\nu}$.

In both schemes, a first amplification stage is placed at low temperatures. Even like this, the amplifiers noise at the input is several orders of magnitude larger than the noise levels generated by the device (representing here the signal). To improve the signal to noise ratio, a lock-in detection technique is used in both cases. The dc current through the device is modulated at a low frequency $f \approx 1 \text{ kHz}$, and the amplified excess noise is measured synchronously. This leads to a sensitivity improvement by a factor $\sqrt{\Delta\nu} \tau$, where τ is the integration time of the lock-in amplifier [40].

In the first example [7] a good impedance matching is achieved by means of an additional resistance in series with the device (see Fig. 2.10a). This also ensures

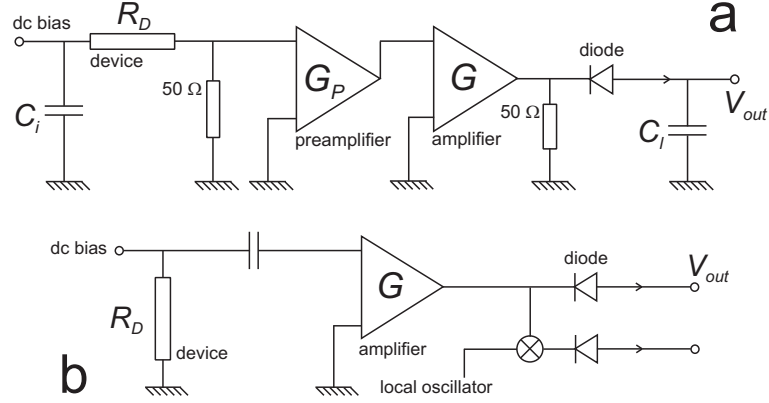


Figure 2.10: High frequency detection schemes using rectifying diodes. A good impedance matching is achieved either **(a)** by adding a $50\ \Omega$ series resistance or **(b)** by choosing a small impedance device .

a constant dynamical resistance, making easier the subtraction of the amplifier current noise. The fluctuations are measured between 8 and 18 GHz ($\Delta\nu = 10$ GHz) and the detection sensitivity is $6 \times 10^{-23}\ \text{V}^2/\text{Hz}$.

For the second example (see Fig. 2.10b) the device has a low impedance ($R_D = 47\ \Omega$). Two independent channels can be used for the detection. The first one measures fluctuations at a fixed frequency (1.5 GHz), while the second one makes use of a local oscillator and a mixer to allow detection at frequencies between 5 and 20 GHz. Both channels integrate the noise power in a $\Delta\nu = 0.5$ GHz bandwidth. The sensitivity achieved is $1.3 \times 10^{-23}\ \text{V}^2/\text{Hz}$.

2.4.4 On chip detection of high frequency signals

In this thesis we use quantum detectors to measure noise signals in the high GHz range (several GHz to several 100 GHz). Via capacitive coupling, fluctuations generated by the device modify the electrical transport properties of the detector [41]. By measuring the change induced in the detector $I - V$ characteristics, we can obtain information regarding the high frequency noise generated by the device.

This general idea is followed also in Ref. [42], where authors propose the realization of a double quantum dot as an on chip spectrum analyzer (see Fig. 2.11). Current fluctuations generated by the device induce fluctuations in the energy difference δE between the levels in the two quantum dots (see Fig. 2.11c). They lead to inelastic tunneling events, in which electrons exchange energy with the environment (either absorb or emit, as illustrated in Fig. 2.11c and d). When the central barrier is the most opaque, upon an applied voltage bias V_{bias} , transport is

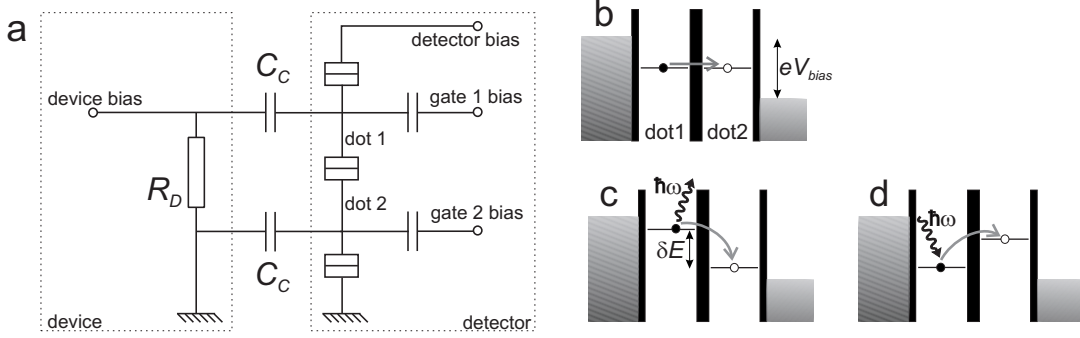


Figure 2.11: (a) Electrical circuitry for a noise detection scheme using double quantum dots. Schematic drawings for elastic (b), respectively inelastic tunneling ((c) and (d)) between the two quantum dots.

determined by inter-dot tunneling events and the inelastic current contains information about the power spectrum of noise. The double dot system can be tuned such that is sensitive either to the absorption, $S_I(\omega)$ (Fig. 2.11c), or emission part of the spectrum, $S_I(-\omega)$ (Fig. 2.11d). The detection frequency $\omega = \delta E/\hbar$ is determined by the energy difference δE between the two levels in the bias window and can be manually tuned.

The lower bound for the detection frequency is determined by the width of the resonant tunneling peak and is in the GHz range [43]. The upper limit is given by the energy level spacing for one dot. For semiconductor quantum dots this can be as large as several meV, corresponding to a detection frequency in the THz range. Special care should be taken to suppress electron pumping effects between one dot and the adjacent lead. Developing a calibration procedure for this detection scheme is difficult, as the coupling strength is highly dependent on the specific sample geometry. Nevertheless, the detection scheme is suited for frequency resolved measurements, in the GHz-THz range, for both emission and absorption part of the noise spectrum.

In this thesis two types of on chip detectors are used: a superconductor-insulator-superconductor (SIS) junction, respectively a semiconductor quantum dot defined in a 2 dimensional electron gas. The detection schemes and mechanisms are presented in chapter 3 respectively chapter 6. The SIS junction is then used, in two separate experiments (chapters 4 and 5), to measure the noise generated by a Cooper pair box, respectively a carbon nanotube quantum dot.

References

- [1] Sh. Kogan, *Electronic noise and fluctuations in solids* (Cambridge University Press, 1996).
- [2] Y. M. Blanter and M. Büttiker, Phys. Rep. **336**, 1 (2000).
- [3] M. B. Johnson, Phys. Rev. **29**, 367 (1927).
- [4] H. Nyquist, Phys. Rev. **32**, 110 (1928).
- [5] J. H. Davies, P. Hyldegaard, S. Hershfield, and J. W. Wilkins, Phys. Rev. B **46**, 9620 (1992).
- [6] W. Schottky, Ann. Phys. (Leipzig) **65**, 51 (1921).
- [7] M. I. Reznikov, M. Heiblum, H. Shtrikman, and D. Mahalu, Phys. Rev. Lett. **75**, 3340 (1995).
- [8] A. Kumar, L. Saminadayar, D. C. Glattli, Y. Jin, and B. Etienne, Phys. Rev. Lett. **76**, 2778 (1996).
- [9] H. E. van den Brom and J. M. van Ruitenbeek, Phys. Rev. Lett. **82**, 1526 (1999).
- [10] H. Birk, M. J. M. de Jong, and C. Schönenberger, Phys. Rev. Lett. **75**, 1610 (1995).
- [11] A. Nauen, I. Hapke-Wurst, F. Hohls, U. Zeitler, R. J. Haug, and K. Pierz, Phys. Rev. B **66**, 161303 (2002); A. Nauen, F. Hohls, N. Maire, K. Pierz, and R. J. Haug, Phys. Rev. B **70**, 033305 (2004).
- [12] L. Saminadayar, B. E. Y. Jin, B. Etienne, and D. C. Glattli, Phys. Rev. Lett. **79**, 2526 (1997).
- [13] R. de-Picciotto, M. Reznikov, M. Heiblum, and V. Umansky, Nature **389**, 162 (1997).
- [14] M. Reznikov, R. de-Picciotto, T. G. Griffiths, M. Heiblum, V. Umansky, G. Bunin, and D. Mahalu, Nature **399**, 238 (1999).
- [15] X. Jehl, P. Payet-Burin, C. Baraduc, R. Calemczuk, and M. Sanquer, Phys. Rev. Lett. **83**, 1660 (1999).
- [16] R. H. Brown and R. Q. Twiss, Nature **178**, 1046 (1956).
- [17] E. Purcell, Nature **178**, 1449 (1956).
- [18] B. L. Morgan and L. Mandel, Phys. Rev. Lett. **16**, 1012 (1966).
- [19] W. D. Oliver, J. Kim, R. C. Liu, and Y. Yamamoto, Science **284**, 299 (1999).

- [20] M. Henny, S. Oberholzer, C. Strunk, T. Heinzel, K. Ensslin, M. Holland, and C. Schönenberger, *Science* **284**, 296 (1999).
- [21] R. J. Schoelkopf, A. A. Clerk, S. M. Girvin, K. W. Lehnert, and M. H. Devoret, *Quantum Noise*, chapter *Qubits as Spectrometers of Quantum Noise*. Kluwer Academic, Dordrecht (2003). cond-mat/0210247.
- [22] L. Van Hove, *Phys. Rev.* **95**, 249 (1954).
- [23] U. Gavish, Y. Levinson, and Y. Imry, *Phys. Rev. B* **62**, R10637 (2000).
- [24] G. B. Lesovik and R. Loosen, *JETP Lett.* **65**, 295 (1997).
- [25] M. B. Weissman, *Rev. Mod. Phys.* **60**, 537 (1988)
- [26] B. D. Josephson, *Phys. Lett.* **1**, 251 (1962).
- [27] L.P. Kouwenhoven, D.G. Austing, and S. Tarucha, *Rep. Prog. Phys.* **64** (6), 701 (2001).
- [28] S. J. Tans, M. H. Devoret, H. Dai, A. Thess, R. E. Smalley, L. J. Geerligs, and C. Dekker, *Nature* **386**, 474 (1997).
- [29] M. Bockrath, D. H. Cobden, P. L. McEuen, N. G. Chopra, Andreas Thess, R. E. Smalley, and A. Zettl, *Science* **275**, 1922 (1997).
- [30] L. P. Kouwenhoven, C. M. Marcus, P. L. McEuen, S. Tarucha, R. M. Westervelt, and N. S. Wingreen, in *Mesoscopic Electron Transport*, edited by L. L. Sohn, L. P. Kouwenhoven, and G. Schön, (Kluwer, Series E **345**, 1997), p.105-214.
- [31] See e.g. R. Hanson, I. T. Vink, D. P. DiVincenzo, L. M. K. Vandersypen, J. M. Elzerman, L. H. Willems van Beveren, and L.P. Kouwenhoven, published in the Proceedings of the XXXIXth Rencontres de Moriond (La Thuile, 2004) *Quantum information and decoherence in nanosystems*. cond-mat/0407793.
- [32] S. Iijima, *Nature* **354**, 56 (1991).
- [33] M. M. J. Treacy, T. W. Ebbesen, and J. M. Gibson, *Nature* **381**, 678 (1996).
- [34] J. W. G. Wildöer, L. C. Venema, C. Dekker, A. G. Rinzler, and R. E. Smalley, *Nature* **391**, 59 (1998).
- [35] Marc Bockrath, David H. Cobden, Jia Lu, Andrew G. Rinzler, Richard E. Smalley, Leon Balents, and Paul L. McEuen, *Nature* **397**, 598 (1999).
- [36] J. Kong, H. T. Soh, A. M. Cassell, C. F. Quate, and H. Dai, *Nature* **395**, 878 (1998).
- [37] Van der Ziel, *Noise in Solid State Devices and Circuits* (Wiley, New York, 1986).

- [38] D. C. Glatthi, P. Jacques, A. Kumar, P. Pari, and L. Saminadayar, *J. Appl. Phys.* **81**, 11 (1997).
- [39] M. Henny, S. Oberholzer, C. Strunk, and C. Schönenberger, *Phys. Rev. B* **59**, 2871 (1997).
- [40] R. H. Dicke, *Rev. Sci. Instrum.* **17**, 268 (1946).
- [41] G. L. Ingold and Y. V. Nazarov, in *Single-Charge Tunneling*, edited by H. Grabert and M. H. Devoret (Plenum, New York, 1992).
- [42] R. Aguado and Leo P. Kouwenhoven, *Phys. Rev. Lett.* **84**, 1986 (2000).
- [43] T. Fujisawa, T. H. Oosterkamp, W. G. van der Wiel, B. W. Broer, R. Aguado, S. Tarucha, and L. P. Kouwenhoven, *Science* **282**, 932 (1998).

Chapter 3

On chip Detection of Quantum Noise in Mesoscopic Devices

E. Onac, R. Deblock and L.P. Kouwenhoven

We employ an superconductor-insulator-superconductor (SIS) junction to measure high frequency noise in the current of a quantum device. The detector and device are capacitively coupled on chip. This allows noise detection over a large bandwidth (up to several 100 GHz, depending on the superconducting material). We detect the noise generated by another SIS junction. Using the AC Josephson effect we perform frequency resolved measurements up to 100 GHz with Al as superconductor. At higher biases we measure shot noise due to quasiparticle current. Non-symmetric emission noise is measured using a sub-gap biased detector.

3.1 Introduction

Measurements of electrical noise, i.e. current fluctuations due to quantization of the electric charge, are an important tool for studying the electronic properties of mesoscopic devices [1]. They can provide additional information besides the usual conductance measurements, in particular when charge motion is regulated by interaction effects between charge carriers. Electrical noise is usually characterized by a power spectral density defined as the Fourier transform of the current-current correlator

$$S_I(\omega) = \int_{-\infty}^{+\infty} d\tau e^{i\omega\tau} \langle \delta I(t + \tau) \delta I(t) \rangle \quad (3.1)$$

where $\delta I(t) = I(t) - \langle I \rangle$ represents the time dependent current fluctuations around the mean value $\langle I \rangle$. This definition is valid for the usual case of positive frequencies ($\omega > 0$ or $\tau > 0$) as well as for negative values ($\omega < 0$ or $\tau < 0$). The distinction between these two cases will become clear in the following.

Depending on the relation between the energy scales set by temperature ($k_B T$), sample bias (eV) and frequency ($\hbar\omega$) we can distinguish three noise regimes. At high temperature ($k_B T \gg eV, \hbar\omega$) thermal fluctuations of the charge carriers lead to Johnson-Nyquist noise. Its power spectral density is white (i.e. frequency independent) and proportional to temperature and sample conductance. At low temperatures ($k_B T \ll eV$), when moving from low to high frequencies, a crossover from a classical to a quantum limit exists at $\hbar\omega = eV$. Most experiments so far focused on measuring the noise at low frequencies (kHz range) where shot noise dominates [1]. The shot noise spectrum is white with a power density directly proportional to the average current and symmetric in terms of frequencies (i.e. there is no difference between the positive and negative side). Here we study noise in the high frequency regime (GHz range), where the energy $\hbar\omega$ is of the order or higher than $k_B T$ and eV . In this case it is important to consider the quantum system together with the surrounding environment and the energy exchange between them as sketched in Fig. 3.1. From the point of view of the device, the detector acts as an environment. Any kind of processes involving emission of energy from the device to the environment are depicted by the upper arrow. In our notation these emission processes contribute to the negative frequency part of the noise spectrum $S(-\omega)$. Processes associated with absorption of energy from the environment are indicated by the lower arrow and these contribute to $S(\omega)$.

At $T = 0$ the presence of zero-point fluctuations (ZPF) in the environment leads to spontaneous emission. This refers to the "willingness" to absorb energy

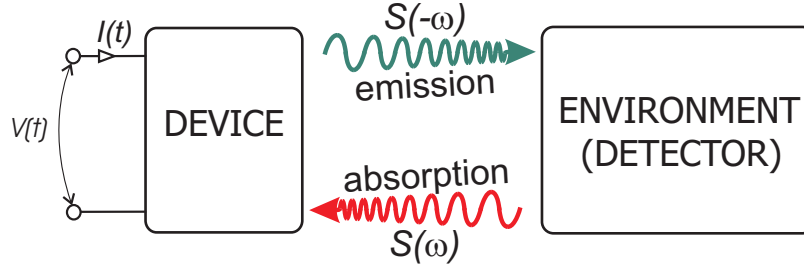


Figure 3.1: Quantum device and its surrounding environment. Fluctuating current $I(t)$ (voltage drop $V(t)$) in bias lines gives rise to different types of noise. Processes taking place in the device entail energy exchange with the environment (emission or absorption). The two types of processes are indicated with the two arrows (green, respectively red); each of them contribute to a different part of the noise spectral density. A detector coupled to the device can also be viewed as being part of the environment.

quanta from the device even when the environment is in its ground state. The necessary energy in this case is supplied by the external device bias. At the same time the reverse process, namely absorption of energy by the device from the environment, is completely suppressed here simply due to the lack of energy in the bath. The asymmetry in the occurrence of these two types of processes yields $S(\omega) \neq S(-\omega)$.

At finite temperatures, also stimulated processes (both emission and absorption) take place because of the energy now available in the environment. As long as spontaneous emission gives a significant contribution an absorption-emission asymmetry remains observable in the noise spectrum. Consequently ZPF in the electromagnetic field of the environment lead to an asymmetry in the noise between positive and negative frequencies. This asymmetry in the noise has been defined as quantum noise [2, 3, 4]. To measure quantum noise a spectrum analyzer able to discern between emission and absorption processes is needed. The *quantum spectrum analyzer* has to be quiet when measuring the emission part of the noise (to avoid the stimulated absorption processes at the device) and the energy should be provided by the device bias. When measuring the absorption part the energy must be supplied by the detector which should give a signal only when the device absorbs it.

In this frequency range (where $\hbar\omega \gg k_B T, eV$) the internal energy scales of the studied mesoscopic device can also be probed, while the sensitivity is increased due to a larger bandwidth. Only very few experiments are available in this regime [5] because of the difficulty in working at such high frequencies (typically between 1 and a few 100 GHz for mesoscopic devices). Special care has to be taken in

this case for achieving a good coupling between device and detector as parasitic capacitances could easily lead to a signal leak.

We present our method for measuring non-symmetrized current fluctuations (in the frequency range from 5 to 80 GHz) by using a superconductor-insulator-superconductor tunnel junction as an on chip spectrum analyzer. We test this new technique by measuring the emission noise generated by a Josephson junction, in both regimes of AC-Josephson effect and quasiparticle tunneling. The usefulness of this detection scheme was demonstrated in measuring the narrow band noise generated by an electrically driven charge qubit (see Ref. [6]).

3.2 Method

The idea of on chip noise detection is realized by capacitively coupling the quantum device of interest to a detector [7, 4]. For the detector we use a superconductor-insulator-superconductor (SIS) junction which is extensively used as a high frequency mixer [8] in astrophysics to detect weak microwave signals [9]. The detection principle is based on photon assisted tunnelling (PAT) of quasiparticles across a barrier formed by an insulating layer between two superconducting electrodes (Fig. 3.2a). The PAT current is a DC signal, but, as discussed below, it contains information regarding the high frequency spectrum of the microwave radiation present in its environment. In essence, the SIS detector rectifies an incident fluctuating signal into a DC signal which is much easier to measure.

We consider only the quasiparticle current through a voltage biased SIS junction and assume full suppression of the super-current (density of states is sketched in Fig. 3.2a). For bias voltages $V_{SIS} < 2\Delta/e$, no quasiparticle tunnelling is possible (due to the gap in the density of states of the superconductors) and therefore no current will flow. For $e|V_{SIS}| \geq 2\Delta$, the bias provides enough energy to brake Cooper pairs resulting in a quasiparticle current (see black curve in Fig. 3.2b). The corresponding resistance, $R_N = \partial V_{SIS} / \partial I_{SIS}$, is called the normal state resistance.

However, even for $e|V_{SIS}| < 2\Delta$, if the junction is submitted to HF radiation, a quasiparticle current can occur provided that the absorbed photons have enough energy. For photons of energy $\hbar\omega$ a non-zero PAT current can flow if the bias voltage satisfies $e|V_{SIS}| > 2\Delta - \hbar\omega$. In the case of a single frequency signal this leads to the emergence of a small step (Fig. 3.2b, red curve). The position of the onset and the step height are determined by the frequency and the power of the radiation, respectively. Thus the PAT current provides information on the number and the energy of the photons reaching the junction. The process

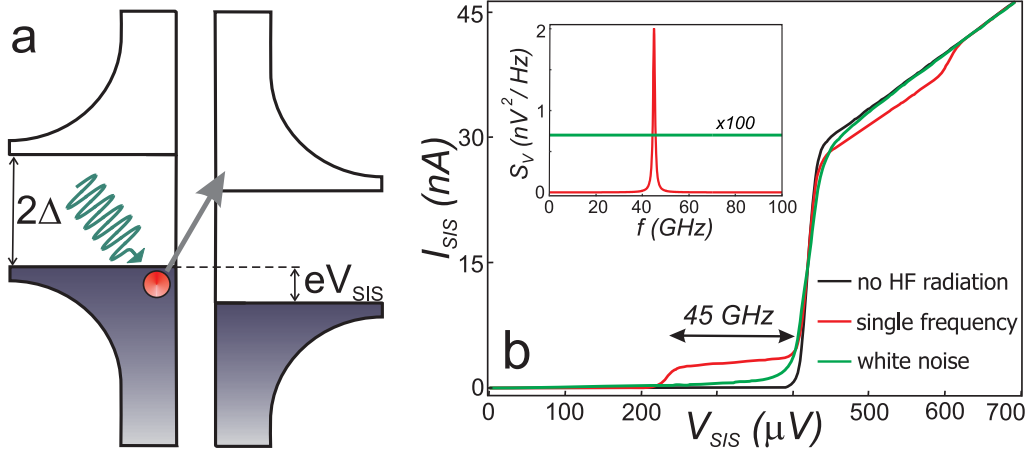


Figure 3.2: (a) Density of states (horizontal) versus energy (vertical) for a SIS junction biased at a voltage V_{SIS} . PAT involves absorption of an energy quantum from an external electromagnetic wave allowing quasiparticle tunneling to higher, empty energy states. Δ is the superconducting gap. (b) Numerical simulation: the influence of high frequency radiation on the $I - V$ characteristic of a SIS junction for monochromatic respectively white noise (see inset). We consider here only the quasiparticle current; the black line represents the $I - V$ without radiation while the red and green ones are in the presence of HF radiation. In case of single frequency radiation, the change in the quasiparticle current is a step-like increase and a reduction on the two sides of the superconducting-normal state resistance transition. For the white spectrum radiation the PAT current leads to a more gradual increase of the quasiparticle current close to the transition. Inset: positive frequencies side (signal is symmetric on the negative side) of the used power spectral densities: a single frequency (sinusoidal oscillating signal at 45GHz with a thermal broadening of 1GHz) respectively a white noise signal.

described above involves absorption of (microwave) photons by the detector. In a capacitively coupled device-detector scheme these photons are emitted by the device under study, thus contributing to its *emission* part of the noise $S(-\omega)$.

The absorption spectrum of the device, denoted by $S(+\omega)$, is non-zero when the device can absorb photons from its environment, i.e. in our scheme the SIS junction. At zero temperature the SIS emission spectrum is zero (i.e. noiseless) in the sub-gap region $eV_{SIS} < 2\Delta$. For $eV_{SIS} > 2\Delta$ the noise in the quasiparticle current contains energy which can be absorbed by the device. This energy loss in the detector leads to a step-wise reduction in the SIS $I - V$ curve (see Fig. 3.2b). The reduction is more difficult to measure since it occurs on a fairly large background current.

In the case of radiation with a white spectrum the change in the $I - V$ is a gradual increase in the quasiparticle current as more frequencies give a contri-

bution when we move close to the superconductor-normal state transition. Note that the HF power taken in the simulation of Fig. 3.2b is large for a clear illustration of the effect.

3.2.1 Theory of SIS junction as a detector for HF fluctuations

The theory for PAT in SIS junctions is well-known for symmetrized noise sources, i.e. $S(-\omega) + S(\omega)$ [8]. It is our goal to distinguish between $S(-\omega)$ and $S(\omega)$. Here we work out an extended theory for the PAT current in SIS junctions. For this derivation we, momentarily, view the SIS detector as "the device" and the device under study as the environment. Noise in the environment (i.e. current noise generated by the device) capacitively couples as voltage fluctuations across the SIS detector. The total quasiparticle current can be written as (see Appendix A)

$$I_{QP}(V_{SIS}) = \int_0^{+\infty} d\epsilon' P(e\bar{V}_{SIS} - \epsilon') I_{QP,0}\left(\frac{\epsilon'}{e}\right) \quad (3.2)$$

Eq. (3.2) is a convolution between the probability $P(\epsilon)$ of energy exchange with the environment and the current-voltage characteristic of the junction in the absence of the environment $I_{QP,0}(V_{SIS} = \epsilon'/e)$.

We first relate the probability $P(\epsilon)$ to the power spectrum of the voltage fluctuations across the SIS junction, $S_V(\omega)$. Here we sketch the steps of the full derivation given in Appendix A. We associate a fluctuating phase $\delta\varphi(t) \equiv \frac{e}{\hbar} \int^t dt' \delta V_{SIS}(t')$ to the fluctuating voltage across the SIS detector, $\delta V_{SIS}(t) = V_{SIS}(t) - \bar{V}_{SIS}$. The fluctuations can be characterized by the phase correlator $J(t) = \langle \delta\varphi(t)\delta\varphi(0) - (\delta\varphi(0))^2 \rangle$. Using the phase definition the first part can be written as

$$\langle \delta\varphi(t)\delta\varphi(0) \rangle = \frac{e^2}{\hbar^2} \int^t dt' \int^0 dt'' \langle \delta V_{SIS}(t') \delta V_{SIS}(t'') \rangle \quad (3.3)$$

We also have the definition for the *non-symmetrized* power spectral density of the voltage fluctuations across the junction

$$S_V(\omega) \equiv \int_{-\infty}^{+\infty} dt e^{i\omega t} \langle \delta V_{SIS}(t) \delta V_{SIS}(0) \rangle \quad (3.4)$$

Note that the *symmetrized* version is defined as

$$S_V^{symm}(\omega) \equiv \int_{-\infty}^{+\infty} dt e^{i\omega t} \frac{1}{2} [\langle \delta V_{SIS}(t) \delta V_{SIS}(0) \rangle + \langle \delta V_{SIS}(0) \delta V_{SIS}(t) \rangle].$$

Combining Eqs.(3.4) and (3.3) gives

$$\langle \delta\varphi(t)\delta\varphi(0) \rangle = \frac{e^2}{2\pi\hbar^2} \int^t dt' \int^0 dt'' \int_{-\infty}^{+\infty} d\omega e^{-i\omega(t'-t'')} S_V(\omega) \quad (3.5)$$

After performing the first two integrals we get [7]

$$J(t) = \frac{e^2}{2\pi\hbar^2} \int_{-\infty}^{+\infty} d\omega \frac{e^{-i\omega t} - 1}{\omega^2} S_V(\omega) \quad (3.6)$$

The probability $P(\epsilon)$ for energy exchange is defined as the Fourier transform of the phase correlator $J(t)$ (see Appendix A)

$$P(\epsilon) = \frac{1}{2\pi\hbar} \int_{-\infty}^{+\infty} dt \exp \left[J(t) + \frac{i}{\hbar} \epsilon t \right] \quad (3.7)$$

In the limit of small noise powers $S_V(\omega)$, the condition $J(t) \ll 1$ is fulfilled, and we can make use of the approximation $\exp[J(t)] \approx 1 + J(t)$ to relate $P(\epsilon)$ to the voltage fluctuations $S_V(\omega)$

$$P(\epsilon) \approx \frac{1}{2\pi\hbar} \int_{-\infty}^{+\infty} dt e^{i\epsilon t/\hbar} [J(t) + 1] = \left[1 - \frac{e^2}{2\pi\hbar^2} \int_{-\infty}^{-\infty} d\omega \frac{S_V(\omega)}{\omega^2} \right] \delta(\epsilon) + \frac{e^2}{2\pi\hbar} \frac{S_V(\epsilon/\hbar)}{\epsilon^2} \quad (3.8)$$

Inserting this expression in equation (3.2), we obtain for the photon assisted tunneling current

$$\begin{aligned} I_{PAT}(V_{SIS}) &= I_{QP}(V_{SIS}) - I_{QP,0}(V_{SIS}) \\ &= \int_0^{+\infty} d\omega \left(\frac{e}{\hbar\omega} \right)^2 \frac{S_V(-\omega)}{2\pi} I_{QP,0} \left(V_{SIS} + \frac{\hbar\omega}{e} \right) \\ &\quad + \int_0^{eV_{SIS}} d\omega \left(\frac{e}{\hbar\omega} \right)^2 \frac{S_V(\omega)}{2\pi} I_{QP,0} \left(V_{SIS} - \frac{\hbar\omega}{e} \right) \\ &\quad - \int_{-\infty}^{+\infty} d\omega \left(\frac{e}{\hbar\omega} \right)^2 \frac{S_V(\omega)}{2\pi} I_{QP,0}(V_{SIS}) \end{aligned} \quad (3.9)$$

The first term corresponds to emission from the device (absorption by the SIS detector, $\omega < 0$). The second describes the absorption by the device (emission by the SIS detector, $\omega > 0$) and the third one renormalizes the elastic SIS current. Note that the second term is cut-off at $\hbar\omega = eV_{SIS}$ since the SIS detector cannot emit more energy than supplied by the bias, while for the first term all frequencies give a contribution (they can always be absorbed by the detector). Although not

apparent from this equation, a cut-off frequency (in $S_V(-\omega)$) given by the device bias is introduced also for this term.

An important experimental case is when $eV_{SIS} < 2\Delta$. Then $I_{QP,0}(V_{SIS} - \frac{\hbar\omega}{e}) = 0$ and $I_{QP,0}(V_{SIS}) = 0$ so that only the first term can have a non-zero contribution:

$$I_{PAT}(V_{SIS}) = \int_0^{+\infty} d\omega \left(\frac{e}{\hbar\omega} \right)^2 \frac{S_V(-\omega)}{2\pi} I_{QP,0} \left(V_{SIS} + \frac{\hbar\omega}{e} \right) \quad (3.10)$$

Here the SIS detector is completely quiet and sensitive only to the emission part of the voltage noise ($\omega < 0$) generated by the device.

Case of a single frequency spectrum

Suppose that the voltage fluctuations are of the form $\delta V_{SIS}(t) = V_{SIS,0} \cos(\omega_0 t + \varphi)$. Then the time correlator becomes

$$\langle \delta V_{SIS}(t + \tau) \delta V_{SIS}(t) \rangle = \frac{V_{SIS,0}^2}{2} \cos(\omega_0 \tau) \quad (3.11)$$

and thus $S_V(\omega) = \frac{V_{SIS,0}^2}{4} [\delta(\omega + \omega_0) + \delta(\omega - \omega_0)]$. Inserting this formula in Eq. (3.9), we get

$$I_{PAT}(V_{SIS}) = \frac{1}{8\pi} \left(\frac{eV_{SIS,0}}{\hbar\omega_0} \right)^2 \left[I_{QP,0} \left(V_{SIS} + \frac{\hbar\omega_0}{e} \right) + I_{QP,0} \left(V_{SIS} - \frac{\hbar\omega_0}{e} \right) - 2I_{QP,0}(V_{SIS}) \right] \quad (3.12)$$

which is the well known Tien-Gordon result derived in ref. [10], in the limit of small $eV_{SIS,0}/\hbar\omega_0$. The change in the $I - V$ characteristic of the SIS junction for this case of single frequency spectrum has been qualitatively described at the beginning of this section and presented in Fig. 3.2b.

Again, for $eV_{SIS} < 2\Delta$, the last two terms are not contributing and

$$I_{PAT}(V_{SIS}) = \frac{1}{8\pi} \left(\frac{eV_{SIS,0}}{\hbar\omega_0} \right)^2 I_{QP,0} \left(V_{SIS} + \frac{\hbar\omega_0}{e} \right) \quad (3.13)$$

Thus, for a spectrum with a single frequency, the PAT detector signal at biases below $2\Delta/e$ is a copy of the original $I - V$ step with its onset shifted by $\hbar\omega_0/e$ and its height scaled by a factor containing both the amplitude, $V_{SIS,0}$, and the frequency ω_0 of the oscillation.

This treatment relates the PAT current to the voltage fluctuations across the SIS junction. After measuring the detector PAT signal, the spectrum of the fluctuations can be obtained using de-convolution techniques. Finally, if we wish to study the current noise of a device $S_I(\omega)$ we need to know how this translates into a voltage noise $S_V(\omega)$ across the SIS detector. This is discussed next.

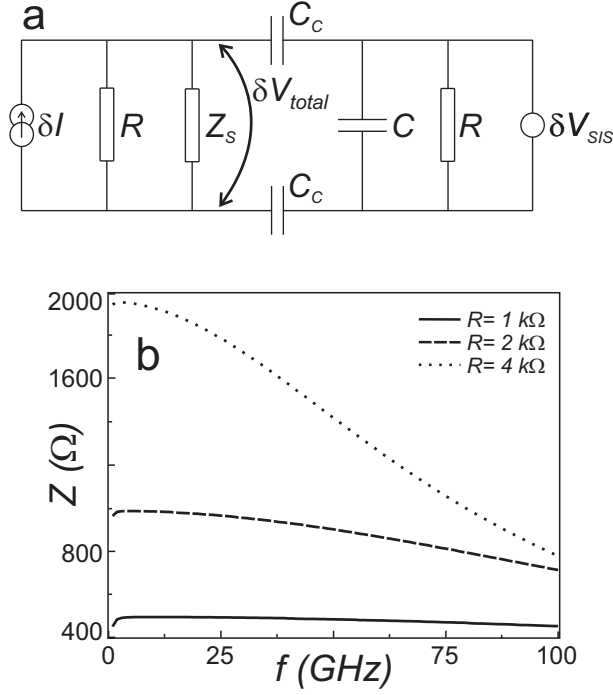


Figure 3.3: (a) Equivalent AC scheme of the coupling circuit. Coupling capacitances C_C delimit the device (left) respectively the detector (right) side. The current fluctuations are introduced as a current source. Z_S is the impedance of the device while the SIS detector is represented as a capacitance C (its resistance is very high in the bias regime $V_{SIS} < 2\Delta$). (b) Frequency dependence of the transimpedance $|Z(\omega)|$ calculated from Eq.(3.16) using the DC values for the coupling capacitances C_C and on chip resistances R . The device impedance Z_S is assumed to be large and therefore neglected. The capacitance associated with the SIS detector is $C = 1 \text{ fF}$.

3.2.2 The coupling circuitry. Fabrication

In order to achieve good detection sensitivity one has to provide a good coupling between the device under study and the SIS junction in the frequency range of interest. For electrical circuits this coupling is described by the transimpedance $Z(\omega)$

$$|Z(\omega)|^2 = \frac{S_V(\omega)}{S_I(\omega)} \quad (3.14)$$

which expresses how well the current fluctuations generated by the device $S_I(\omega)$, couple as voltage fluctuations across the SIS detector junction, $S_V(\omega)$, at a certain frequency ω . A good signal transfer (in terms of fluctuations reaching the detector as compared to the noise generated by the source) requires a high value for $Z(\omega)$. To evaluate the transimpedance we consider the equivalent AC scheme for our

circuit (see Fig. 3.3a). The coupling between device and detector is provided by coupling capacitances C_C , while the resistances R are used to isolate the circuit (the detector, the coupling capacitances and the device) from the external part. In particular they isolate from parasitic capacitances to ground induced by the wiring between the measurement setup at room temperature and the sample; those parasitic capacitances act as a short circuit for the HF signal and would drastically influence our sensitivity. Noise is introduced as a fluctuating current source. Transimpedance $Z = \delta V_{SIS}/\delta I$ relates a small current excitation δI to the voltage change δV_{SIS} induced across the detector. The total voltage change across the device can be expressed as

$$\delta V_{total} = \left[\frac{1}{R} + \frac{1}{Z_S} + \frac{1}{z} \right]^{-1} \delta I \quad (3.15)$$

where Z_S is the impedance of the device, $z = 2/i\omega C_C + R/(1 + i\omega CR)$ corresponds to the right part of the circuit including the coupling capacitances and C is the capacitance of the SIS detector. From these voltage fluctuations only a fraction $\delta V_{SIS}/\delta V_{total} = R/z(1 + i\omega CR)$ drops across the detector. Therefore the transimpedance can be written as

$$Z(\omega) = \frac{i\omega C_C R}{2 + i\omega(2C + C_C)R} \left[\frac{1}{R} + \frac{1}{Z_S} + \left(\frac{2}{i\omega C_C} + \frac{R}{1 + i\omega CR} \right)^{-1} \right]^{-1} \quad (3.16)$$

Using the values for the circuit elements presented at the end of this section we obtain the frequency dependence shown in Fig. 3.3b (assuming a high device impedance, thus neglecting the term $1/Z_S$). We stress that this calculation is only indicative for the experimental transimpedance. It is complicated to have a precise representation of all the on chip components at high frequencies. In particular, the resistances have also a distributed capacitance to ground, which is not included. Thus, to allow for quantitative statements one needs to calibrate the on chip circuit, i.e. measure $Z(\omega)$.

Equation (3.16) shows the importance that the different parts of the coupling circuitry play in achieving a good detection sensitivity. For a simple dependence of the detector signal compared with the device noise signal, a flat dependence of $Z(\omega)$ versus ω is preferable. The electrical scheme of the actual circuitry, based on resistances and capacitances, is shown in Fig. 3.4a. The capacitances C_C are designed to provide a strong coupling between the detector and the device at high frequency and to permit independent DC biasing for the two parts of the circuit. Four contact wires are used for the device and also for the detector. This allows us to bias and measure at the same time the real voltage drop on both sides.

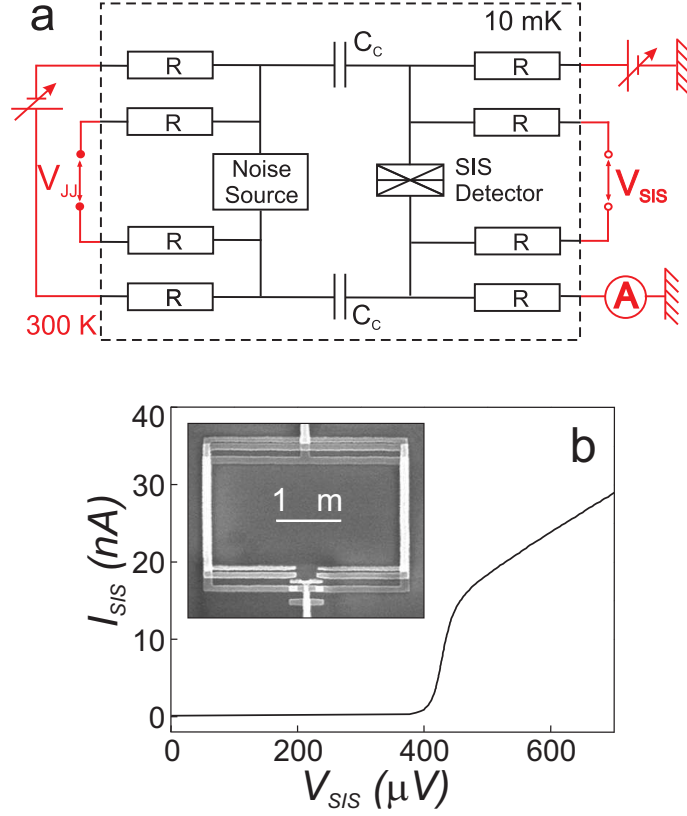


Figure 3.4: (a) Schematic of the coupling circuit between the device (the noise generator) and the SIS detector. The circuit comprises on chip resistances R and coupling capacitances C_c . This is the black area which is cooled down to a temperature of 14 mK. The red part represents the biasing and measurement equipment at room temperature. (b) $I-V$ characteristic for the SIS detector in absence of noise. Super-current is suppressed using an external applied small magnetic field. Quasiparticle tunneling leads to step increase in the I_{SIS} current at the voltage bias $V_{SIS} = 2\Delta/e$. Inset: SEM picture of the detector: two SIS junctions in a SQUID geometry allowing for a tuning of the Josephson coupling by means of a magnetic flux Φ .

A SEM picture of the on chip detector is presented in the inset of Fig. 3.4b. The fabrication process of the sample necessitates three steps of electronic beam lithography. The first step resides in the fabrication of the resistances (20 μm long Pt wires with a width of 100 nm and a thickness of 20 nm) and the bottom plates of the capacitances (80x10 μm^2). In the second step we deposit the insulating oxide layer for the capacitances (50 nm of SiO). During the third step the top plates of the capacitances are deposited and the source and the detector are fabricated out of Al using a shadow evaporation technique. This choice for the superconducting material results in a detection bandwidth between

5 and 90 GHz. The value of the resistances is $R = 2 \text{ k}\Omega$ (measured at a 14 mK temperature). The capacitances are estimated to be $C_C = 550 \text{ fF}$.

3.3 High frequency emission of a Josephson Junction

In order to calibrate our SIS noise detection coupling circuitry we measure the already well characterized noise generated by a Josephson junction. Both the device and detector are fabricated in a SQUID geometry which allows to tune the Josephson coupling and thus the supercurrent (the Cooper-pair current). The areas of the two SQUIDS are in a ratio of $1:6$ so we can independently tune the Josephson currents: maximize it for the device and minimize it for the detector junction (as mentioned, we only use the quasiparticle branch for the detection).

Depending on the bias conditions, the Josephson junction can be used as a source of either narrow or broad band noise. The detector signal is different for these two cases. This is apparent from Fig. 3.5a which plots the detector PAT current as a function of source junction bias (V_{JJ}) and detector bias (V_{SIS}). The plot represents the detector signal induced by the noise coming from the device (source junction): is obtained by subtracting the detector current in the two cases of finite and zero source bias. This is done because the detector current is not completely blocked in the sub-gap region $V_{SIS} < 2\Delta/e$ (even when there is no bias applied to the source junction) (see inset of Fig. 3.5a). The two regions in Fig. 3.5b correspond to a voltage bias for the source below or above $2\Delta/e$ and they are associated with two different types of tunneling processes. We analyze them separately in the following.

3.3.1 AC Josephson effect

When the bias voltage V_{JJ} is below $2\Delta/e$ only a Cooper-pair current flows, which is characterized by [11]

$$I = I_C \sin(\phi) \quad (3.17)$$

$$\frac{d\phi}{dt} = \frac{2eV_{JJ}}{h} \quad (3.18)$$

with ϕ the superconducting phase difference across the junction and $I_C = \pi\Delta/(2eR_N)$ the critical current. Consequently, for a finite DC bias, the junction acts as a HF signal generator with an AC current of amplitude I_C and frequency $f = 2eV_{JJ}/h$. This is the single frequency case presented in the previous Sections.

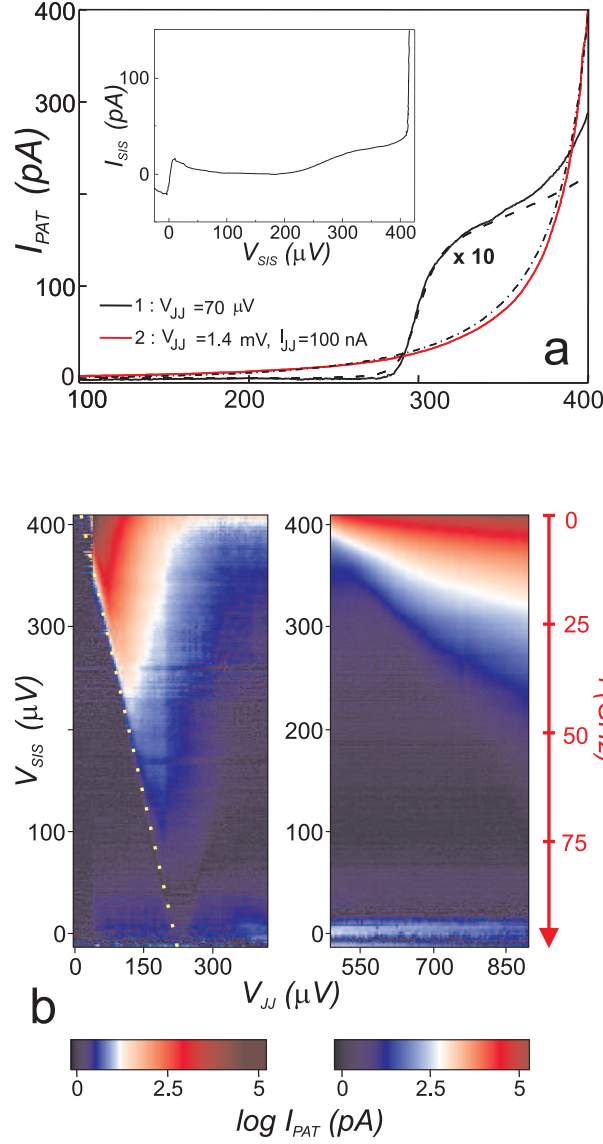


Figure 3.5: (a) Detector curves (solid lines) with fits (dashed and dash-dotted line) for two different bias conditions of the device: AC Josephson, respectively quasiparticle regime. Inset: sub-gap part for I-V characteristic of the SIS detector in the case of zero device bias $V_{JJ} = 0$. A suppressed Josephson branch around $V_{SIS} = 0$ and a small current I_{SIS} in the sub-gap region are visible. (b) Density plots in logarithmic scale of the PAT detector current as a function of source and detector bias (V_{JJ} and V_{SIS}). This is the contribution in quasiparticle current caused by the noise coming from the device (source SIS junction). The two regions correspond to the AC Josephson effect ($V_{JJ} < 2\Delta$) and, respectively, quasiparticle shot noise ($V_{JJ} > 2\Delta$). The dotted line in the AC Josephson part highlights the onset of the small step in the detector signal

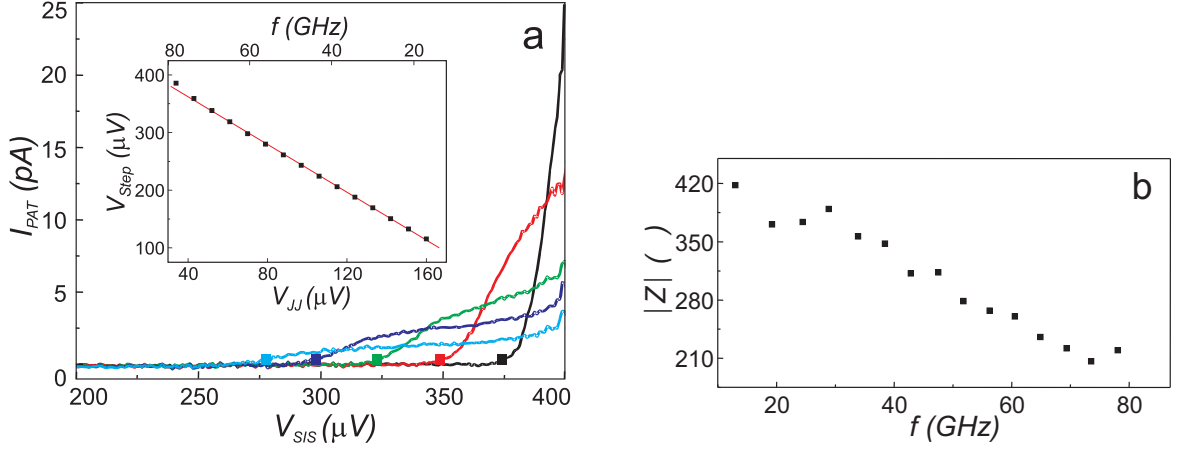


Figure 3.6: (a) PAT current in the AC Josephson regime for source biases (red, green, blue and cyan respectively) $V_{JJ} = 15, 30, 45, 60, 73 \mu\text{V}$. Inset: extracted step position (squares in the big plot) as a function of V_{JJ} . Upper axis gives the corresponding frequency $f = 2eV_{JJ}/h$. (b) Extracted frequency dependence of the transimpedance $|Z(f)|$.

The detector signal (vertical cuts in the left plot of Fig. 3.5b) is presented in Fig. 3.6a for several selected source bias voltages, V_{JJ} . Note that only the region where $V_{SIS} < 2\Delta$ is presented, i.e. only the contribution in the PAT current due to $S(-\omega)$ (emission noise from Josephson junction). We obtain a step-like PAT current indicating the presence of a single dominant frequency in the detected signal (compare to Fig. 3.2b). The measured frequency is directly proportional to the length of the small step $2\Delta/e - V_{step}$, where V_{step} represents its onset position defined as the V_{SIS} value where the PAT current exceeds a small threshold (see the squares in Fig. 3.6a). The linear dependence in equation (3.18) is clearly visible in the density plot (dotted line in Fig. 3.5b) and is extracted from selected curves in the inset of Fig. 3.6a. The slope of the linear fit $\alpha = -2.1$ is in good agreement with the expected value of $\alpha_{theory} = -2$ (transport involves $2e^-$ Cooper-pair charge in the source junction and e^- quasiparticle charge in the detector).

Using equation (3.13) with the amplitude $V_{SIS,0} = |Z|I_C$ these curves can be fitted very well (see Fig. 3.5a) with $|Z|$ as the only fitting parameter (in our case $R_N = 14.1 \text{ k}\Omega$ corresponds to a critical current value $I_C = 23 \text{ nA}$). Repeating this at different frequencies f determines the transimpedance as shown in Fig. 3.6b. The values are slightly smaller than estimated theoretically (see Fig. 3.3a), but with a similar frequency dependence.

Note that it should be possible, in principle, to extract the spectral width of the AC Josephson effect (i.e. using equation (3.10) to determine $S_V(\omega)$).

However, since I_{PAT} is a convolution of $S_V(\omega)$ and the $I - V$ of the SIS detector, this is possible only if this width is larger than the width of the transition at 2Δ in the $I - V$ characteristic of the SIS detector. Our devices are in the other limit, prohibiting the extraction of the spectral width of the AC Josephson effect.

3.3.2 Shot noise of the quasiparticle current

In the limit $eV_{JJ} > 2\Delta$, the bias provides enough energy for quasiparticle tunneling through the source junction. The associated (non-symmetrized) shot noise $S_I(\omega)$ can be written in this case [7]

$$S_I(\omega) = \frac{1}{R_N} \left[\frac{\hbar\omega + eV_{JJ}}{1 - \exp\left(-\frac{\hbar\omega + eV_{JJ}}{k_B T}\right)} + \frac{\hbar\omega - eV_{JJ}}{1 - \exp\left(-\frac{\hbar\omega - eV_{JJ}}{k_B T}\right)} \right] \quad (3.19)$$

This expression simplifies in the zero temperature limit ($|eV_{JJ}|, \hbar|\omega| \gg k_B T$) and for $V_{JJ} > 0$ we have

$$S_I(\omega) = \begin{cases} 0 & \text{for } \omega < -\omega_0 \\ (eV_{JJ} + \hbar\omega)/R_N & \text{for } -\omega_0 < \omega < \omega_0 \\ 2\hbar\omega/R_N & \text{for } \omega_0 < \omega \end{cases} \quad (3.20)$$

with $\omega_0 = eV_{JJ}/\hbar$.

A schematic picture of this dependence is given by the solid line in Fig. 3.7. As already discussed, the asymmetry between positive and negative frequencies is caused by the ZPF: the system (here the Josephson junction) can always absorb energy leading to a finite noise contribution on the absorption part ($\omega > 0$); whereas on the emission part this is non-zero only when the bias provides enough energy to excite the environmental states (for $-\omega_0 < \omega < 0$). On the positive side the change in slope corresponds to the point where the bias cannot induce anymore stimulated emission (the energy provided is not enough) and therefore only spontaneous emission processes take place for $\omega > \omega_0$. The flat band shot noise regime is in the limit of low frequencies ($\omega \ll \omega_0$) and not clearly visible in this picture.

In our case the source junction is biased above the gap ($eV_{JJ} > 2\Delta$) and the detector is sensitive on the emission side to frequencies $-2\Delta < \hbar\omega < 0$. Since the 2 junctions have the same Δ we are in the regime $-\omega_0 (= -eV_{JJ}/\hbar < -2\Delta/\hbar) < \omega < 0$ and we cannot measure the cut-off at $-\omega_0$.

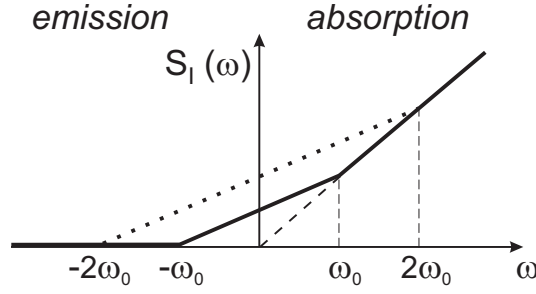


Figure 3.7: Zero temperature noise for a junction with bias voltage V_{JJ} (solid line). The effect of the bias is visible in the frequency range $(-\omega_0, \omega_0)$. Outside this interval the noise vanishes for the negative part and increases linearly for positive frequencies. The dotted line represents the case for a bias voltage that is two times larger. White shot noise only occurs in the limit $\omega \rightarrow 0$.

The PAT contribution to the SIS current in this case is shown in Fig. 3.8a and the difference from the AC Josephson effect (Fig. 3.6b) is clearly visible: broad band noise now leads to a PAT current that does not have a step-like shape anymore, but increases gradually as more (lower) frequencies contribute to PAT when we approach the transition at $eV_{SIS} = 2\Delta$.

From these curves it is possible to extract the noise spectral density by making use of equation (3.10) and knowing the PAT current and the $I - V$ characteristic of the junction without noise (i.e. $I_{QP,0}(V_{SIS})$). Special care has to be taken to cure numerical instabilities with regularisation techniques. Numerically it is convenient to extract $S_V(\omega) = |Z(\omega)|^2 S_I(\omega)$ (inset of Fig. 3.8a) and then deduce $S_I(\omega)$ (shown in Fig. 3.8b) by using the previously determined transimpedance.

The value of the noise deduced from this fit is consistent with the Poissonian value of the non-symmetrized noise eI_{JJ} . The result deviates by a factor 2 from the well known Schottky value $S_I^{sym} = 2eI$ since we measure the non-symmetrized noise (only emission part). As we discussed, the noise can be expressed like $S_I(-\omega) = (eV_{JJ} - \hbar\omega)/R_N$. Because $eV_{JJ} \gg \hbar\omega$, this renders a weak frequency dependence (close to a white spectrum) which prevents us from clearly seeing the frequency dependent part of the noise with the present accuracy.

An alternative way of analyzing the data is to observe that a white noise power spectral density gives a good fit to the experimental curves in Fig. 3.8a with the amplitude S_I as the only fitting parameter (see Fig. 3.5a). In this way a linear dependence of the noise S_I as a function of source current I_{JJ} can be obtained. The standard error deviation for the linear fit $S_I = eI_{JJ}$ indicates a noise resolution for this detection of $80 \text{ fA}^2/\text{Hz}$, equivalent with a temperature noise of 3 mK on a 1 k Ω resistor. If we take into account the source impedance

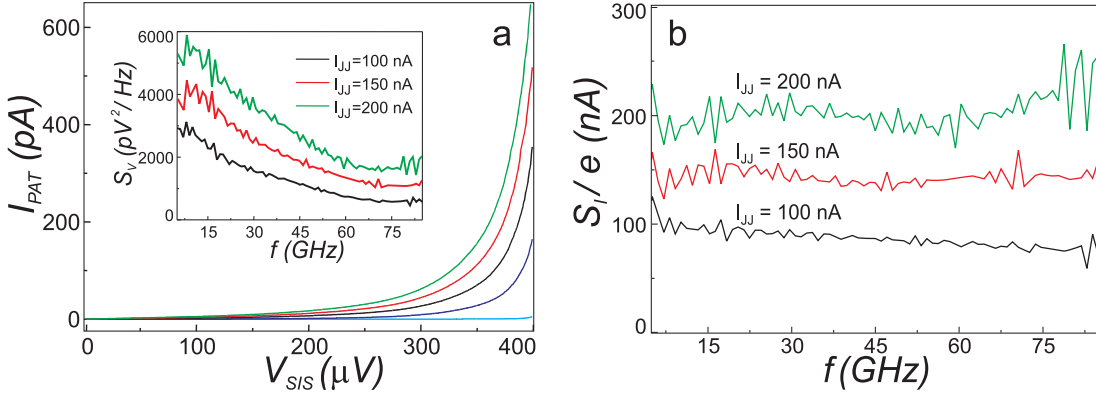


Figure 3.8: (a) Increasing I_{PAT} for $I_{JJ} = 10, 50, 100, 150, 200$ nA. Inset: Voltage spectral density $S_V(\omega)$ extracted from the PAT current. This refers to the voltage fluctuations across the detector. (b) Current spectral density (i.e. $S_I(\omega) = S_V(\omega)/|Z(\omega)|^2$) determined for different I_{JJ} through the source.

($R_N = 14$ k Ω) this translates in a voltage noise of $S_V = 1.6 \times 10^{-20}$ V²/Hz. This compares well with a resolution of $S_V = 7.7 \times 10^{-20}$ V²/Hz achieved by a cross-correlation technique for noise measurements at low frequencies [12].

3.4 Power and efficiency

In the AC Josephson effect regime the signal can be measured for frequencies as high as 90 GHz. The power of the signal coupled into the circuit by the source can be written: $P_{source} = ZI^2/2$, where $Z = 400$ Ω is the transimpedance and $I = I_C = 23$ nA is the amplitude of the AC oscillating current through the source (given by the critical current). This leads to a dissipated power $P_{source} = 100$ fW. The power of the measured signal (leading to a detector signal) is given by: $P_{detector} = hf I_{PAT}/e$. At the frequency $f = 25$ GHz the measured detector signal is $I_{PAT} = 30$ pA resulting in $P_{detector} = 3$ fW. Thus the signal is converted into a PAT current with a quantum efficiency of $P_{detector}/P_{source} = 0.03$ at 25 GHz.

3.5 Conclusions

We demonstrated that SIS junctions can be used as detectors for high-frequency emission noise in mesoscopic devices. They act as an on chip spectrum analyzer allowing us to determine the amplitude of microwave signals from usual DC measurements. The SIS scheme is suited for high frequency (5–90 GHz) detection and allows frequency resolved noise measurements with a high sensitivity.

We are grateful to L. Gurevich for the important contribution to the sample fabrication. We thank Y. Nakamura, C. J. P. M. Harmans, P. Hadley, Y. Nazarov, H. Mooij, D. Bagrets and Y. Blanter for discussions. We acknowledge the technical assistance of R. Schouten, B. van der Enden and M. van Oossanen. Supported by the Dutch Organisation for Fundamental Research (FOM), and from U.S. Army Research Office (grant DAAD19-02-1-0700).

References

- [1] Y. M. Blanter and M. Büttiker, Phys. Rep. **336**, 1 (2000).
- [2] U. Gavish, Y. Levinson, and Y. Imry, Phys. Rev. B **62**, R10637 (2000).
- [3] G. B. Lesovik and R. Loosen, JETP Lett. **65**, 295 (1997).
- [4] R. J. Schoelkopf, A. A. Clerk, S. M. Girvin, K. W. Lehnert and M. H. Devoret in *Quantum Noise in Mesoscopic Physics* edited by Y. V. Nazarov (Kluwer, Dordrecht, 2003).
- [5] R. J. Schoelkopf, P. J. Burke, A. A. Kozhevnikov, M. J. Rooks, and D. E. Prober, Phys. Rev. Lett. **78**, 3370 (1997).
- [6] R. Deblock, E. Onac, L. Gurevich, and L. P. Kouwenhoven, Science **301**, 203 (2003).
- [7] R. Aguado and L. P. Kouwenhoven, Phys. Rev. Lett. **84**, 1986 (2000).
- [8] J. R. Tucker and M. J. Feldman, Rev. Mod. Phys. **57**(4), 1055 (1985).
- [9] P. L. Richards, T. M. Shen, R. E. Harris, and F. L. Lloyd, Appl. Phys. Lett., **34**, 345 (1979).
- [10] P. K. Tien and J. P. Gordon, Phys. Rev. **129**, 647 (1963).
- [11] M. Tinkham, *Introduction to Superconductivity* (McGraw-Hill, Singapore, ed. 2, 1996).
- [12] D. C. Glatthli, P. Jacques, and A. Kumar, J. Appl. Phys. **81**, 7350 (1997).
- [13] R. H. Koch, D. J. Van Harlingen, and J. Clarke, Phys. Rev. Lett. **47**, 1216 (1981).
- [14] V. A. Khlus, Zh. Éksp. Teor. Phys. **49**, 513 (1989) [JETP Lett. **49**, 592 (1989)].

Chapter 4

Detection of Quantum Noise from an Electrically-Driven Two-Level System

E. Onac, R. Deblock, L. Gurevich and L.P. Kouwenhoven

Quantum mechanics can strongly influence the noise properties of mesoscopic devices. To probe this effect we have measured the current fluctuations arising from coherent charge oscillations in a two-level system, a superconducting charge qubit. For the detection we used a superconductor-insulator-superconductor tunnel junction as an on chip spectrum analyzer for high-frequency fluctuations (5-90 GHz). A narrow band peak is observed in the spectral noise density at the frequency of the coherent charge oscillations.

Parts of this Chapter have been published in Science **301**, 203 (2003).

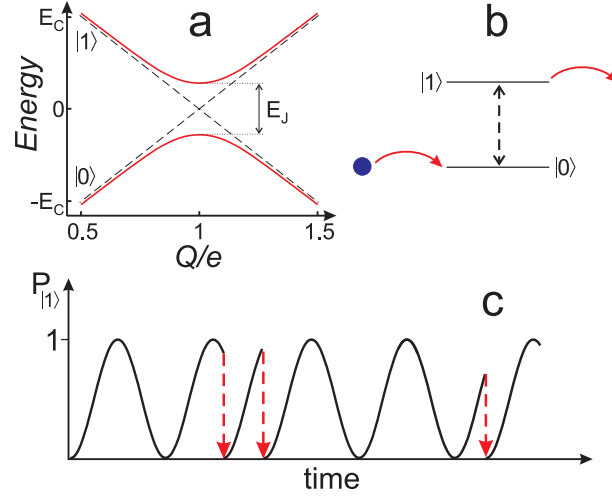


Figure 4.1: (a) Energy diagram for a two-level system with parameters for a superconducting charge qubit of charging energy E_C . Q is the qubit charge. The charge states $|0\rangle$ and $|1\rangle$ are coupled by the Josephson energy, E_J , causing the bending of the dashed lines into the solid red curves. (b) A particular case of current flow via a TLS (see text). (c) Schematic evolution of the probability to be in state $|1\rangle$ as a function of time. The collapses to the $|0\rangle$ state occur when the TLS is emptied. For a superconducting charge qubit the oscillations have frequency E_J/h and the collapse occurs by quasiparticle tunneling.

4.1 Introduction

Noise, i.e. current fluctuations, has proved to be a powerful tool to probe mesoscopic devices [1]. At high frequency it can bear strong signature of the dynamics resulting from quantum mechanics. One of the simplest system to study this effect is a two-level system (TLS) with two coupled quantum states, $|0\rangle$ and $|1\rangle$, which can form a coherent superposition, $\alpha|0\rangle + \beta|1\rangle$, with α and β complex numbers (see Fig. 4.1a). If this TLS is forced into state $|0\rangle$ at time equal to zero, the probability, $P_{|1\rangle} = |\beta|^2$, to find the system in state $|1\rangle$ oscillates in time with a frequency determined by the coupling strength. This prediction [2] has recently attracted much interest in the context of quantum computation where TLS form the physical realizations of the qubit building blocks. To determine the state of the qubit some detection mechanism is needed. In the case of solid state devices the qubit state is often measured by means of the value of an electrical current [3]. We are interested in the fluctuations in the read-out current and how these are affected by the oscillating time-evolution of a qubit.

The central idea is illustrated in Fig. 4.1b and c. Suppose an electron hops on

a TLS and initially occupies state $|0\rangle$. Due to the coupling between the two states (dashed arrow) $P_{|1\rangle}$ starts to oscillate. The electron can leave the TLS towards the right only when $P_{|1\rangle}$ is high. A new electron then repeats the cycle. Thus the outgoing current consists of charge injections that preferentially occur near odd integer times half the oscillation period after the previous tunneling event (see Fig. 4.1c). The fluctuations in the current still bear this non-stochastic noise and instead of the usual white noise spectrum, a narrow band peak is expected at the frequency determined by the coupling strength.

The idea above is very general and theoretical predictions on narrow band noise exist for Bloch oscillations in a double quantum well [4], charge oscillations in superconducting [5] and semiconducting qubits [6], and electron spin resonance oscillations [7]. The experimental detection is difficult as the frequency, f , of the coherent oscillations is typically in the GHz range in order to fulfil the condition $hf \gg k_B T$, with $k_B T$ the thermal energy [8].

Our detection scheme follows the ideas of Refs. [10, 11]: a quantum device is coupled on chip to a detector that converts the high-frequency noise signal into a DC current. The on chip coupling provides a large frequency bandwidth (100 GHz) whereas the conversion to DC allows standard amplification of the signal [12]. Our detector is a superconductor-insulator-superconductor (SIS) tunnel junction, known to be a sensitive microwave detector and well established in astronomy measurements [13]. For low voltage bias, the gap (Δ) in the density of states prohibits tunnelling of quasiparticles. However, for a given voltage bias V_{SIS} , the absorption of a photon of energy that exceeds $(2\Delta - eV_{SIS})$, can assist tunnelling. This photon-assisted tunneling (PAT) current carries information on the number and the frequency of photons reaching the detector [14]. We demonstrate the use of the SIS detection scheme elsewhere [15]. There we obtain the frequency-resolved spectral density of current noise in the range of 5 to 90 GHz [16] by using another SIS junction as noise source.

For a quantitative description, we consider an SIS junction subject to current fluctuations. The PAT current for a bias $eV_{SIS} < 2$ is given by [17]:

$$I_{PAT}(V_{SIS}) = \int_0^{+\infty} d\omega \left(\frac{e}{\hbar\omega} \right)^2 |Z(\omega)|^2 \frac{S_I(-\omega)}{2\pi} I_{QP,0} \left(V_{SIS} + \frac{\hbar\omega}{e} \right) \quad (4.1)$$

with $I_{QP,0}(V_{SIS})$ the SIS current without noise, $Z(\omega)$ the transimpedance [$Z(\omega) = \{S_{V,SIS}(\omega)/S_I(\omega)\}^{1/2}$, i.e., voltage fluctuations at the detector divided by current fluctuations from the source]. We emphasize that here the spectral density $S_I(\omega)$ corresponds to a non-symmetrized noise correlator [10, 11, 18, 19]. Our SIS detector measures absorption of photons, which were emitted from the Josephson junction. Because the SIS detector itself is virtually noiseless for $eV_{SIS} < 2\Delta$,

no emission from the detector occurs and thus no absorption takes place in the Josephson junction. Under these conditions, we only measure the spectral density at (as commonly defined) negative frequencies, $S_I(-\omega)$ [20].

To demonstrate narrow-band noise from an electrically-driven qubit, we have chosen the Cooper Pair Box (CPB) as a physical realization of the TLS. The coherent control of the artificial two level system constituted by a single Cooper Pair Box (CPB) was already demonstrated [3] and recently the coupling of two such qubits permitted the implementation of the CNOT operation [9]. The CPB is fabricated with the same aluminum technology as the SIS detector and therefore easy to integrate on chip.

4.2 Sample Fabrication and Characterization

In order to achieve a good coupling at high frequencies between the source and the detector, we embedded both of them in an on chip circuit. We used a Si substrate with a 300 nm SiO insulating layer on top. For the fabrication electron beam lithography and shadow evaporation technique was employed.

Three electron beam lithography steps were used. First one for the deposition of the on chip resistances, a second one for the insulator layer of the capacitances

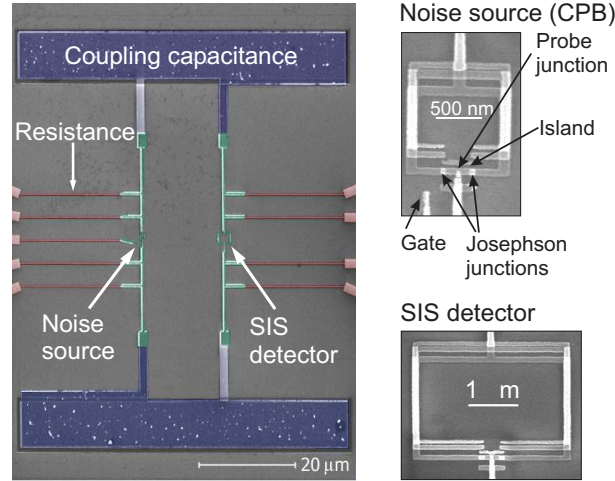


Figure 4.2: *Left:* SEM picture of the sample. Colors were assigned to different parts of the circuit for clarity: the on chip resistances are in red, the coupling capacitances in blue, while the source and the detector are embedded in the green part. *Right:* blow-up of the source and the detector part. Both the source (the Cooper pair box) and the detector are in a SQUID geometry which allows for tuning of Josephson coupling by means of a magnetic flux.

and the third one for the source and detector themselves. Both the detector and the source are provided with four contacts which allows us to measure the current and the real voltage drop at the same time. The on chip resistances are intended to prevent the leakage of the high frequency signal via stray-capacitances to ground. They were made out of a thin Pt layer with the following dimensions: $0.02 \times 0.1 \times 20 \mu\text{m}$. Their measured resistance value was $3.3 \text{ k}\Omega$ at room temperature, respectively $1.9 \text{ k}\Omega$ at 20 mK .

For coupling the source signal to the detector two big capacitances ($10 \times 80 \mu\text{m}$) were fabricated. The bottom layer is made out of a 20 nm thick Pt layer; then a 50 nm thick SiO insulator layer and the top layer is made out of Al (120 nm thick). The estimated capacitance is $C_C = 550 \text{ fF}$. SEM pictures of the CPB and the SIS detector are presented in Fig. 4.2, right. They are both made out of Al with. For the detector and the Josephson junction of the CPB the oxidation was made at 30 mT O_2 for 3 min . For the probe junction of the CPB 5 min of glow discharge in a 45 mT O_2 atmosphere was used. These resulted in resistances of $R_J = 16 \text{ k}\Omega$ respectively $R_P = 335 \text{ k}\Omega$ and capacitances of $C_J = 720 \text{ aF}$ and $C_P = 121 \text{ aF}$ (see Fig. 4.2, left).

The Cooper pair box is a superconductor island on which Cooper pairs, from a superconducting reservoir, can tunnel back and forth through a Josephson

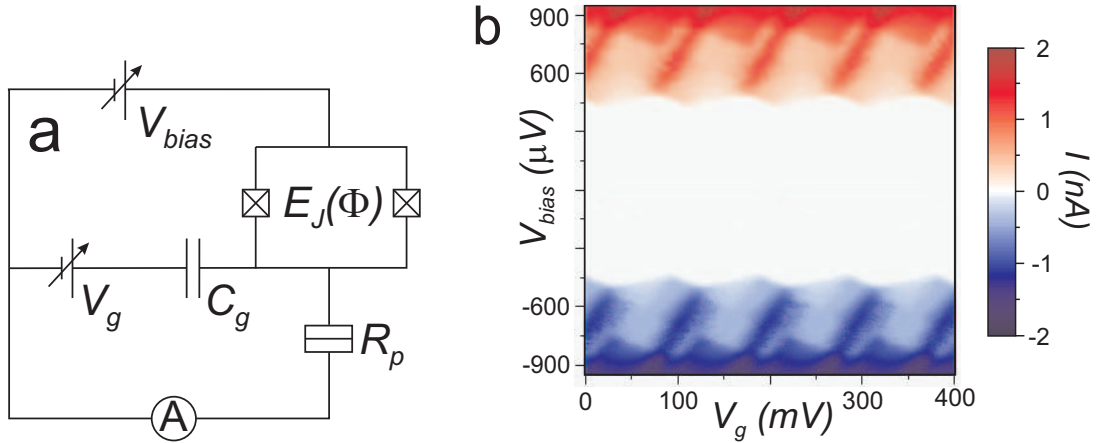


Figure 4.3: (a) Electrical scheme of the voltage biased CPB. The superconductor island is connected with two Josephson junctions to a superconductor electrode allowing the tunneling of Cooper pairs. The voltage bias, V_{bias} , drops mainly across the more resistive probe junction (R_p) causing quasiparticle tunneling. The charge on the island Q can be modified by means of a gate voltage V_g applied to a side electrode. The Josephson energy E_J can be tuned by changing the magnetic flux Φ through the SQUID. (b) Density plot of the current through the Cooper pair box as a function of gate voltage V_g and bias V_{bias} .

junction. In our case, as shown in Fig. 4.2, we use two Josephson junctions in a SQUID geometry. This allows us to tune the tunnel coupling. The electrical scheme of a voltage biased CPB is sketched in Fig. 4.3a.

The relevant energy scales are: charging energy of the island $E_C = e^2/2C_\Sigma$ (with C_Σ the total capacitance of the island), Josephson energy E_J , superconducting gap Δ and thermal energy $k_B T$. When they are in the relation $\Delta, E_C \ll E_J, k_B T$ we can consider the CPB a two level system, where only the two lowest energy states (with zero $|0\rangle$ and one extra Cooper pair on the island $|1\rangle$) play a role. The energies of these two states are plotted in Fig. 4.1a (dashed line) as a function of the gate induced charge $Q = C_g V_g$. Due to the finite Josephson coupling E_J there is a level repulsion, bending the eigen-states (solid line) away from the charge states. They are formed by the symmetric and anti-symmetric combination of the charge states.

To obtain the parameters that characterize the CBP, we first performed Coulomb blockade measurements. The density plot of the current through the qubit is presented in Fig. 4.3b. Quasiparticle current is blocked for bias voltages $|eV_{bias}| < 2\Delta + E_C$ due to the superconductor gap Δ and the charging energy E_C . We are interested in the region $2\Delta + E_C < |eV_{bias}| < 2\Delta + 3E_C$ where the Josephson quasiparticle (JQP) cycle [21, 22] gives rise to peaks in the current.

As a function of the gate voltage V_g , the position of these peaks is periodic: they appear whenever the induced charge on the island is an integer number of electron charge $Q = ne$ (here the charge states are degenerate). Close to these points only Cooper Pair tunneling between the island and the superconducting electrodes takes place through the Josephson junctions (quasiparticle transfer is blocked by the superconducting gap Δ). On the other hand, because of the bias drop at the more resistive, probe junction, the Josephson coupling is strongly reduced and only quasiparticle charge transfer is possible.

The tilting of the JQP peak position is due to the asymmetry between the junction's resistances: the resistance of the Josephson junctions $R_J \approx 16 \text{ k}\Omega$ (from measuring similarly fabricated junctions) and the probe junction resistance $R_p = 335 \text{ k}\Omega$. From the bias onset position of the JQP peaks results a charging energy $E_C = 95 \text{ }\mu\text{eV}$ and gate voltage periodicity leads to a capacitance between the island the gate $C_g \approx 1.6 \text{ aF}$. Knowing the values of E_C and C_g , and the surface ratio of the junctions (Josephson and the probe junction) the values of their capacitances are calculated: $C_J = 720 \text{ aF}$, $C_p = 121 \text{ aF}$.

4.3 Noise Emission on the JQP Peak

The two-levels, $|0\rangle$ and $|1\rangle$, correspond to N and $N+1$ Cooper pairs in the box, which is controlled by the gate voltage V_g (see Fig. 4.3a). The two levels are coupled by the Josephson energy, E_J , as already illustrated in Fig. 4.1a [3, 23]. The coherent charge oscillation corresponds to one extra Cooper pair tunnelling on and off the box. When $P_{|1\rangle}$ is high a sudden decay to the $|0\rangle$ state can take place by quasiparticle tunneling out of the qubit. The resulting current is expected to have narrow-band noise around a frequency [5]:

$$f = \frac{\sqrt{[4E_C(Q/e - 1)]^2 + E_J^2}}{h} \quad (4.2)$$

which describes the energy difference between the two-levels in Fig. 4.1a. Because the decay is a stochastic process occurring around odd-multiples times half the oscillation period, the narrow-band noise is not a delta-peak as in the case of the AC Josephson effect. Instead, a broad peak is expected on top of a white shot noise background [5]. The sudden quasiparticle decay is realized for bias and gate voltages near, the so-called Josephson quasiparticle peak [3]. The average number of coherent charge oscillations is determined by the ratio E_J/Γ where Γ is the decay rate for the two quasiparticles [24]. In our device the Josephson junction has a SQUID geometry allowing to tune E_J . Consequently, we can explore both the coherent ($E_J > \Gamma$) and incoherent ($E_J < \Gamma$) regime.

In the coherent regime, if we start in the $|0\rangle$ state, a number of probability oscillations take place before it breaks in two quasiparticle that tunnel out at the probe junction. The width of the JQP peak in this case is given by Γ . Because at the end of this cycle the system is re-initialized to the $|0\rangle$ state and the fact that quasiparticle tunneling can only occur when we have a large probability of having an extra Cooper pair on the island (state $|2\rangle$), the positions of the quasiparticle current peaks are synchronized in time with a odd half-integer periods of the coherent oscillation $(n+1/2)T$ with $T = 1/f$. For the incoherent regime the JQP peak width is determined by E_J and the detector signal is strongly suppressed.

We fix the bias voltage at $V_{bias} = 600 \mu\text{V}$ and focus on one JQP peak (see the inset of Fig. 4.4). Fig. 4.4 shows measurements of the PAT current through the SIS detector for different CPB gate voltages. The PAT current is rather high on the left side ($Q/e < 1$) of the JQP peak and small on the right side ($Q/e > 1$). This is attributed to the emission character of the left side of the JQP peak versus absorption on the right [25]. On the absorption side ($Q/e > 1$) the small PAT signal is attributed to tunnelling processes not related to the coherent dynamics of the CPB, leading to a background PAT current. Indeed

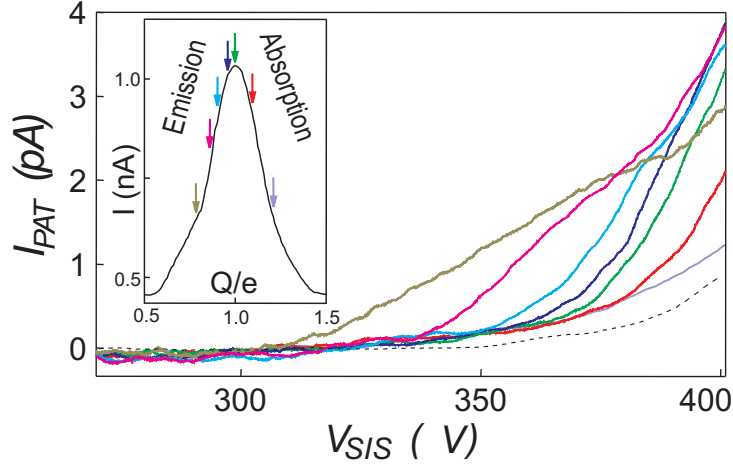


Figure 4.4: PAT current for different positions on the JQP peak, as indicated by arrows in the inset. Colored curves correspond to same colored arrows. The dashed line corresponds to PAT current for $E_J/\Gamma < 1$. *Inset:* Current versus charge, Q , for the CBP on the JQP peak.

since no energy is available flowing towards the CPB the spectral density of the current fluctuations on the absorption side is virtually zero.

On the left side we observe more high-frequency components when moving away from the JQP peak center. To extract the noise component related to the JQP process we subtract the small PAT current at high Q (Fig. 4.5a). We determine then the dominant frequency component from the V_{SIS} value where PAT becomes visible (we checked the validity of this determination of the dominant frequency for the AC Josephson effect). The V_{SIS} values converted to frequencies are plotted versus Q in Fig. 4.5b. The dominant frequency dependence on the charge on the CPB, can be fitted by the energy difference between the two-levels of the CPB (solid curves in Fig. 4.5b). We obtain a charging energy slightly higher than expected. The dominant frequency value for $Q/e = 1$ is consistent with the value of E_J in this sample ($E_J = 50 \mu\text{eV} = 12 \text{ GHz}$ for maximum coupling [26]). Changing E_J (by means of the flux through the SQUID) changes the dominant frequency for $Q/e = 1$ as shown for the red data points. For small values of E_J the PAT signal becomes very weak and has a shot noise shape similar to the PAT curves for $Q/e > 1$ (Fig. 4.4). Indeed, as already discussed, in this incoherent regime ($\Gamma > E_J$) a dominant frequency from narrow-band noise is not expected.

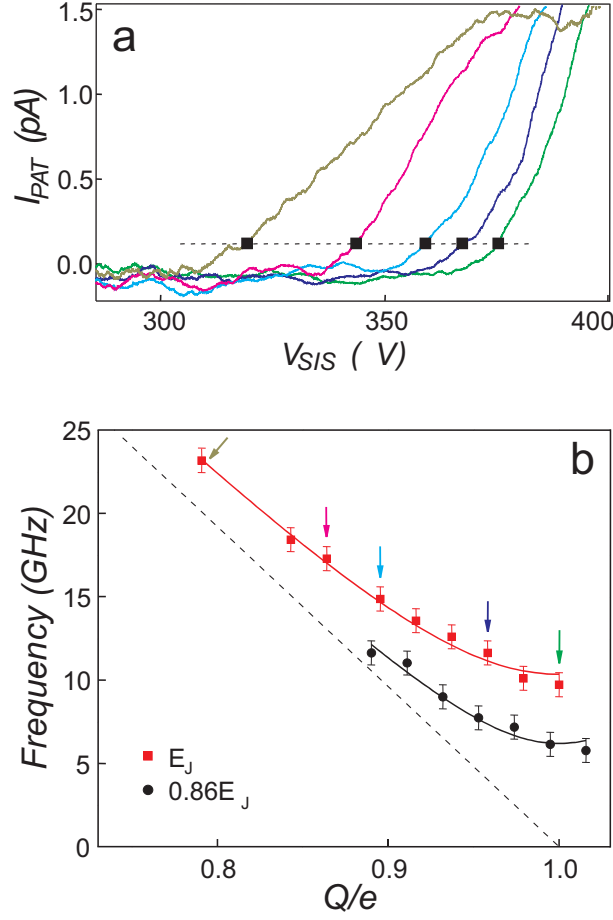


Figure 4.5: (a) PAT current after subtracting the PAT curve for $Q/e = 1.3$. The squares correspond to the V_{SIS} value used for the dominant frequency determination. (b) Dominant frequency deduced from the PAT current for two values of E_J . The solid lines are fits to the expression $\sqrt{(4E_C(Q/e - 1))^2 + E_J^2}/h$. The fit parameter $E_C = 100$ μ eV is slightly higher than the measured charging energy. The arrows correspond to the points denoted on the inset of 4.4.

4.4 Emission Noise at Larger Biases

We study the signal coming from the CPB for the other bias voltages regimes. For $|eV_{bias}| < 2\Delta + E_C$ there the current through the CPB is blocked due to the superconducting gap and the charging energy. When the CPB bias V_{bias} exceeds $(2\Delta + 3E_C)/e$, the spectral density of the detected noise does not depend anymore on the gate voltage V_g and it has a white spectrum as one would expect in the case of a single tunnel junction. This is also apparent from the Fig. 4.6 where we plot (solid lines) the PAT current as a function of detector bias for different CPB bias voltages.

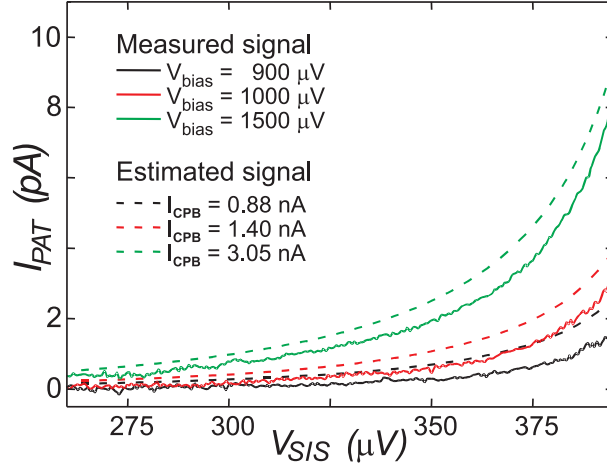


Figure 4.6: Detected and calculated PAT current signal in the case of high V_{bias} across the CPB.

Due to the fact that we have 4 contacts, we are able to voltage bias the CPB ($V_{bias} = 900, 1000, 1500 \mu\text{V}$) and at the same time measure the real bias drop ($V_{real} \approx 880, 985, 1420 \mu\text{V}$). Using this and the value for the total CPB resistance ($R_{total} = R_J + R_p$) we can deduce the current passing through the CPB: $I_{CPB} \approx 0.88, 1.40, 3.05 \text{ nA}$. We compute the expected detector signals corresponding to the emission shot noise for these current values, and plot them (the dashed lines) in Fig. 4.6.

The shapes of the measured and of the estimated detector signal are the same, but there is also a difference between them: the measured signal is always smaller than the expected one. This can be caused to the fact that the Coulomb blockade effects are not completely destroyed even at these large voltage biases, and they still introduce some correlation in the quasiparticle transport, leading therefore to a suppression of the shot noise below the Poissonian value.

4.5 Conclusions

We have demonstrated narrow-band high-frequency detection of non-symmetrized noise. The quantum noise from a charge qubit shows a peak at the frequency of the coherent charge oscillation. The SIS detector is operated as an on chip spectrum analyzer and is applicable for correlation measurements on a wide range of electronic quantum devices.

We thank Y. Nakamura, K. Harmans, P. Hadley, Y. Nazarov, H. Mooij, D. Bagrets and Y. Blanter for discussions. We acknowledge the technical assistance of R. Schouten, B. van der Enden and M. van Oossanen. Supported by the Dutch

Organisation for Fundamental Research (FOM), and from U.S. Army Research Office (grant DAAD19-02-1-0700).

References

- [1] Y. M. Blanter and M. Bttiker, Phys. Rep. **336**, 1 (2000).
- [2] R. P. Feynman, Lectures on Physics, vol. 3 (Addison-Wesley Publishing Company 1965).
- [3] Y. Nakamura, Yu. A. Pashkin, and J. S.Tsai, Nature **398**, 786 (1999).
- [4] A. N. Korotkov, D. V. Averin, and K. K. Likharev, Phys. Rev. B **49**, 7548 (1994).
- [5] M. S. Choi, F. Plastina, and R. Fazio, Phys. Rev. B **67**, 045105 (2003).
- [6] R. Ruskov and A. N. Korotkov, Phys. Rev. B **67**, 075303 (2003) and references therein.
- [7] I. Martin, D. Mozyrsky, and H. W. Jiang, Phys. Rev. Lett. **90**, 018301 (2003).
- [8] The condition $hf > k_B T$ is not required if the two-level system is decoupled from phonons such as in spin systems[27].
- [9] T. Yamamoto, Yu. A. Pashkin, O. Astafiev, Y. Nakamura, and J. S.Tsai , Nature **398**, 786 (1999).
- [10] R. Aguado and L .P. Kouwenhoven, Phys. Rev. Lett. **84**, 1986 (2000).
- [11] R.J. Schoelkopf, A. A. Clerk, S. M. Girvin, K. W. Lehnert, and M. H. Devoret, cond-mat/0210247 and references therein.
- [12] Usually the bandwidth is in the kHz to MHz range due to the long cabling between the low temperature device and room temperature equipment and additional filtering against room temperature noise.
- [13] SIS detectors are sensitive up to frequencies $2\Delta/h$. For aluminium junctions, which are used in this work, this is around 100 GHz. Niobium junctions are used in astronomy and go up to THz.
- [14] J. R. Tucker and M. J. Feldman, Rev. Mod. Phys. **57**, 1055 (1985).
- [15] E. Onac, R. Deblock, L. Kouwenhoven, *in preparation*. See also previous Chapter.
- [16] There have been few measurements of the high-frequency symmetrized current noise, e.g. [28, 29].

[17] This follows from the equation derived in the previous chapter:

$$\begin{aligned}
I_{PAT}(V_{SIS}) &= I_{QP}(V_{SIS}) - I_{QP,0}(V_{SIS}) \\
&= \int_0^{+\infty} d\omega \left(\frac{e}{\hbar\omega} \right)^2 \frac{S_V(-\omega)}{2\pi} I_{QP,0} \left(V_{SIS} + \frac{\hbar\omega}{e} \right) \\
&\quad + \int_0^{eV_{SIS}} d\omega \left(\frac{e}{\hbar\omega} \right)^2 \frac{S_V(\omega)}{2\pi} I_{QP,0} \left(V_{SIS} - \frac{\hbar\omega}{e} \right) \\
&\quad - \int_{-\infty}^{+\infty} d\omega \left(\frac{e}{\hbar\omega} \right)^2 \frac{S_V(\omega)}{2\pi} I_{QP,0}(V_{SIS})
\end{aligned} \tag{4.3}$$

The first term corresponds to emission from the device ($\omega < 0$), the second to absorption ($\omega > 0$) and the third renormalizes the elastic current. For $eV_{SIS} < 2\Delta$ only the first term is non-zero.

- [18] G. B. Lesovik and R. Loosen, JETP Lett. **65**, 295 (1997).
- [19] U. Gavish, Y. Levinson, and Y. Imry, Phys. Rev. B **62**, R10637 (2000).
- [20] When $eV_{SIS} > 2\Delta$ the SIS detector is sensitive to $\omega > 0$. The PAT is then a small correction on a large background current and difficult to measure.
- [21] T. A. Fulton, P. L. Glammell, D. J. Bishop, L. N. Dunkleberger, and G. J. Dolan, Phys. Rev. Lett. **63**, 1307 (1989).
- [22] D. V. Averin and V. Ya. Aleshkin, JETP Lett. **50**, 367 (1989).
- [23] V. Bouchiat, D. Vion, P. Joyez, D. Esteve, and M.H. Devoret, Physica Scripta T **76**, 165 (1998).
- [24] From $\Gamma = (eV + E_C)/e^2 R_P$, where R_P is the probe junction resistance, we deduce $\Gamma = 2GHz$.
- [25] The strong asymmetry in the JQP peak regarding emission and absorption was observed by Y. Nakamura *et al.* [30]. It is also consistent with recent theoretical predictions [31, 32].
- [26] The evaluation of R_J is difficult because R_J is in series with R_P . It is estimated from similarly fabricated junctions with a 20% uncertainty.
- [27] C. Durkan and M. E. Welland, Appl. Phys. Lett. **80**, 458 (2002).
- [28] R. H. Koch, D. J. Van Harlingen, and J. Clarke, Phys. Rev. Lett. **47**, 1216 (1981).
- [29] R. J. Schoelkopf, P. J. Burke, A. A. Kozhevnikov, M. J. Rooks, and D. E. Prober, Phys. Rev. Lett. **78**, 3370 (1997).
- [30] Y. Nakamura, C. D. Chen, and J. S. Tsai, Phys. Rev. Lett. **79**, 2328 (1997).

-
- [31] G. Johansson, e-Print available at <http://xxx.lanl.gov/abs/cond-mat/0210539>.
 - [32] A. A. Clerk, S. M. Girvin, A. K. Nguyen, and A. D. Stone, Phys. Rev. Lett. **89**, 176804 (2002).
 - [33] V. Ambegaokar and A. Baratoff, Phys. Rev. Lett. **10**, 486 (1963).

Chapter 5

Shot Noise Detection on a Carbon Nanotube Quantum Dot

E. Onac, F. Balestro, B. Trauzettel, C. F. Lodewijk and L.P. Kouwenhoven

An on chip detection scheme for high frequency signals is used to detect noise generated by a quantum dot formed in a single wall carbon nanotube. The noise detection is based on photon assisted tunneling in a superconductor-insulator-superconductor junction. This is used to measure current (or voltage) fluctuations in the 5-90 GHz range. Measurements of shot noise over the range of two adjacent Coulomb diamonds is reported, with excited states and inelastic cotunneling clearly resolved. Super-Poissonian noise is detected in the case of inelastic cotunneling.

This chapter was submitted to Physical Review Letters.

5.1 Introduction

The study of shot noise, i.e. non-equilibrium current fluctuations due to the discreteness of charge carriers, is an important tool for studying correlations induced in mesoscopic transport by different types of interactions. Extensive studies have been carried out theoretically and experimentally [1, 2]. When transport is determined by a stochastic process (e.g. electron emission in a vacuum diode or the electron transfer through an opaque tunnel junction) current is characterized by Poissonian shot noise. Electron-electron interactions, such as Coulomb repulsion or resulting from the Pauli exclusion principle, can correlate electron motion and suppress shot noise. The noise power density is defined as the Fourier transform of the current-current correlator

$$S_I(\omega) = \int_{-\infty}^{+\infty} d\tau e^{i\omega\tau} \langle \hat{I}(t + \tau) \hat{I}(t) \rangle. \quad (5.1)$$

Generally, $\hat{I}(t)$ is the current operator in the Heisenberg representation and the brackets represent the expectation value. The definition is valid both for positive and negative frequencies ω , corresponding to energy absorption or emission by the device [3, 4, 5]. The distinction between $S_I(\omega)$ and $S_I(-\omega)$ is only important at high frequencies $\hbar\omega \gg eV$, $k_B T$ (V is the device bias and T the temperature). When $eV \gg \hbar\omega, k_B T$, shot noise dominates over other types of noise and the operator $\hat{I}(t)$ in definition (5.1) can be replaced by the current value $I(t)$. The power density has a white spectrum that can be expressed as $S_I(-\omega) = S_I(\omega) = FeI$, with I the average current. The Fano factor, F , indicates the deviation from Poissonian shot noise for which $F = 1$. If the noise detector can not distinguish between emission and absorption processes, a symmetrized version $S_I^{symm}(\omega) = S_I(\omega) + S_I(-\omega)$ is used. The factor 2 in the usual Schottky formula $S_I^{symm} = 2eI$ refers to this symmetrized case. However, for the detection scheme used here, we are only sensitive to emission noise and therefore the non-symmetrized noise approach is valid.

For electron transport through a quantum dot (QD) shot noise can be either enhanced or suppressed with respect to the Poissonian value. First, for resonant tunneling, when a QD ground state is aligned between the Fermi levels in the leads, the Fano factor can vary between 1/2 and 1. The exact value is determined by the ratio of tunneling rates between the dot and the leads [7]. For strongly asymmetric barriers transport is dominated by the most opaque one and shot noise is Poissonian ($F = 1$). If the barriers are symmetric transport is regulated by Coulomb blockade. The resonant charge state is occupied 50% of the time and a $F = 1/2$ shot noise suppression is predicted. Second, when the QD is in

Coulomb blockade, Fermi levels in the leads are aligned in between two charge states of the QD and first-order sequential tunneling is energetically forbidden. Electron transport can still occur via cotunneling processes [8], elastic or inelastic. These are second order tunneling processes in which two electrons tunnel, at the same time, through the two barriers. The system goes through a virtual intermediate state, allowing electron transfer between the leads. The elastic process leaves the QD in its ground state and transport is Poissonian. Inelastic cotunneling switches the system from a ground to an excited state and can lead to a super-Poissonian noise, with a Fano factor that can reach $F = 3$ [15, 16, 17, 18].

Experiments have shown shot noise suppression due to Coulomb blockade [19, 20]. No experimental results exist on shot noise enhancement in the case of inelastic cotunneling. Here we present the detection of noise generated by a carbon nanotube quantum dot (CNT-QD) over the entire range of a Coulomb diamond. Excited states and inelastic cotunneling are clearly resolved in the noise measurements. For inelastic cotunneling we find super-Poissonian shot noise.

5.2 Detection Principle and Calibration

We use an on chip noise detector consisting of a superconductor-insulator-superconductor (SIS) junction. The measurement scheme together with a SEM picture of the sample is presented in Fig. 5.1. The sample circuitry provides a good coupling at high frequency between CNT-QD and detector, while still allowing for independent DC biasing of the two parts. Noise generated in the CNT-QD leads to photon assisted tunneling of quasiparticles between the superconducting electrodes of the SIS detector. This causes a change in the detector current that contains information about the spectral power of noise [6]. The frequency range of the SIS detector is determined by the superconducting gap, Δ (5-100 GHz in case of Al).

5.2.1 Sample Fabrication

Sample fabrication necessitates 5 steps of electron beam lithography for the different circuitry parts. In intermediate steps CVD deposition and AFM imaging is used for growing and locating the nanotubes. First, on a Si substrate, the markers for *e*-beam lithography and AFM imaging are defined and deposited by evaporating 100nm Pt on top of a 5 nm Ti sticking layer. A second *e*-beam lithography step is used to deposit Mo catalyst particles. Carbon nanotubes are CVD grown from the catalyst particles by heating the substrate at $T=900$ °C for $t=10$ minutes in a CH_4 and H_2 flow [21]. An AFM image of the nanotubes is used

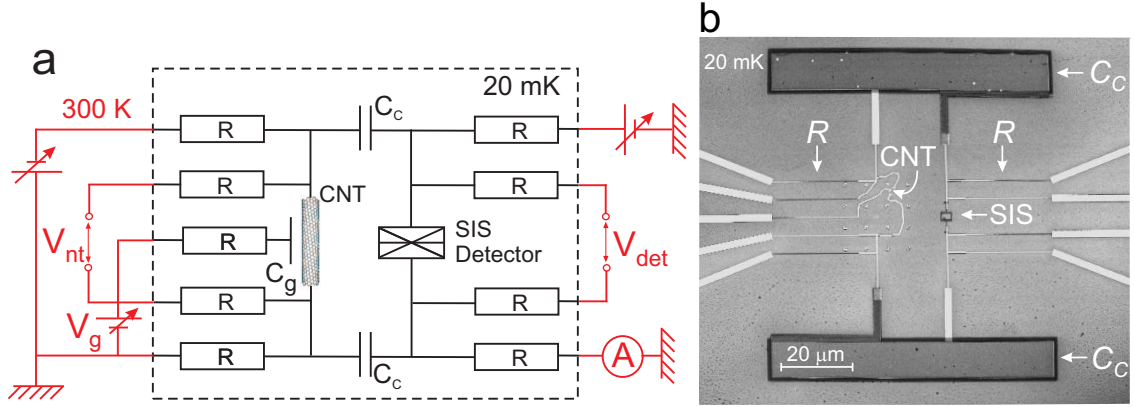


Figure 5.1: (a) Schematic drawing of the detection circuitry. The SIS detector is coupled on chip to the carbon nanotube and is cooled to 20 mK. Bias and measurement wires connect the carbon nanotube and the SIS detector to room temperature electronics. (b) SEM picture of the sample. Two on chip capacitances C_C are used to couple the SIS detector to the CNT-QD (the curly white lines are the custom made contacts). They provide a good AC coupling and allow independent DC biasing for the two sides: CNT and detector. Four contact lines are used for both the CNT and the detector. They allow simultaneous biasing and measurement of current and real voltage drop. An additional contact on the CNT side is used as a side gate. All lines incorporate an on chip impedance R to prevent the high frequency signal from leaking via parasitic capacitances in the leads.

to design contact and side gate electrodes. Contacts and gates are fabricated in a third e -beam step, together with the on chip impedances and the lower plate for the coupling capacitances, by using 10 nm Ti and 20 nm Pt. In the fourth e -beam step the insulating layer (40 nm SiO) for the capacitances is deposited. The SIS detector and the upper plate for the capacitances are fabricated in the last e -beam step. Angle evaporation at $\alpha = \pm 12^\circ$ is used to deposit a 30 nm + 40 nm Al bilayer with an intermediary oxidation step (5 minutes in a 35 mT O₂ atmosphere).

5.2.2 Calibration

Current fluctuations in the CNT-QD, $S_I(\omega)$, induce, via the coupling capacitances, voltage fluctuations between the detector electrodes, $S_V(\omega)$. The detector current in the absence of noise, $I_{SIS,0}(V_{det})$, has a step-like shape (see Fig. 5.2), which is modified by $S_V(\omega)$ into $I_{SIS}(V_{det})$. More specifically, the emission side of the spectrum $S_V(-\omega)$ determines a change of current $I_{det} = I_{SIS} - I_{SIS,0}$ in the sub-gap region ($0 < V_{det} < 2\Delta/e$) that can be expressed as [6]

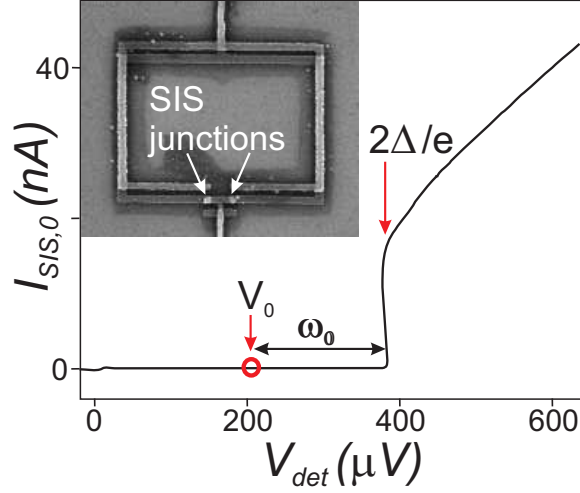


Figure 5.2: $I - V$ characteristic of the detector SIS junction in absence of noise. Current is zero in the superconducting gap region and is determined by the normal state resistance, $R_N = 11.3 \text{ k}\Omega$, for $V_{det} > 2\Delta/e$. For a fixed detector bias, V_0 , the cut-off frequency, ω_0 , represents the lower limit for the detection bandwidth. *Inset:* SEM picture of the detector with two SIS junctions. This SQUID geometry allows us to suppress the supercurrent by means of an external magnetic field.

$$I_{det}(V_{det}) = \int_0^{+\infty} d\omega \left(\frac{e}{\hbar\omega} \right)^2 \frac{S_V(-\omega)}{2\pi} I_{SIS,0} \left(V_{det} + \frac{\hbar\omega}{e} \right) \quad (5.2)$$

Note that $I_{SIS,0}(V_{det}) \neq 0$ only for $V_{det} > 2\Delta/e$. If we consider a detector voltage $V_{det} = V_0$ (see example in Fig. 5.2) then only frequencies above $\omega_0 = (2\Delta/e - V_0)/\hbar$ contribute to the detector current. This means that each point on the detector curve $I_{det}(V_0)$ represents noise detection over a bandwidth $[\omega_0, \infty)$. However, contributions from different frequencies are normalized as $S_V(\omega)/\omega^2$, leading to smaller changes in the detector current for higher frequencies. Finally, S_V is related to the CNT-QD current fluctuations by $S_V(-\omega) = S_I(-\omega)|Z(\omega)|^2$, with the transimpedance $Z(\omega)$ being determined by the coupling circuitry.

In the regime $eV_{nt} \gg k_B T, \hbar\omega$ (V_{nt} is the CNT bias voltage) shot noise dominates over other types of noise (such as Johnson-Nyquist or quantum noise). Here, the power density is proportional to the average current, $S_I \sim I$, and is frequency independent $S_I(\omega) = S_I(-\omega) = S_I(0) = \text{const.}$ (white spectrum). In this case Eq. 5.2 can be written as:

$$I_{det}(V_{det}) = \frac{S_I(0)}{e} \kappa(Z, I_{SIS,0}, V_{det}) \quad (5.3)$$

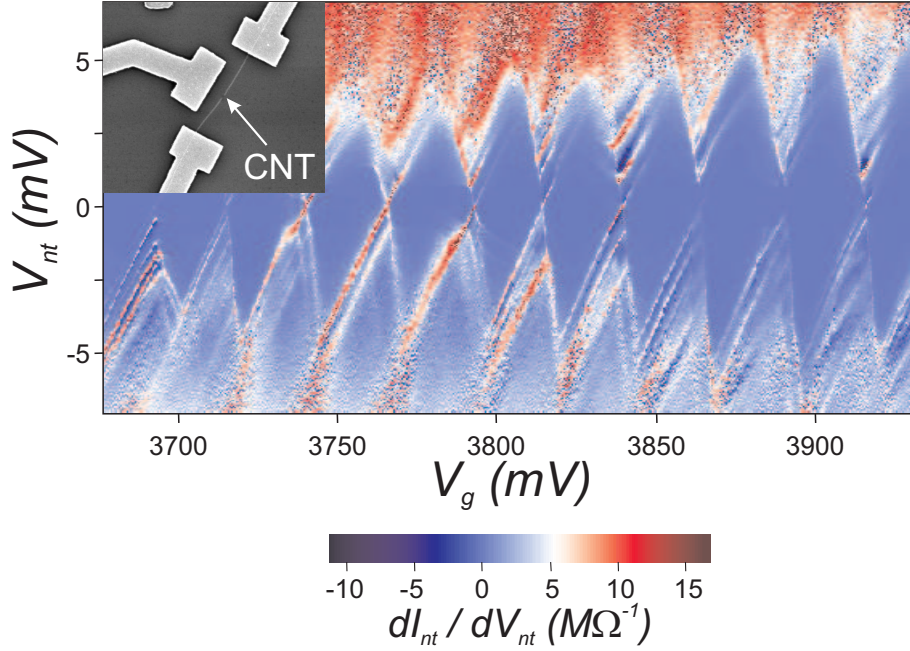


Figure 5.3: Carbon nanotube dI_{nt}/dV_{nt} density plot as a function of bias and gate voltage. This shows standard Coulomb diamonds, corresponding to one dot formed in the carbon nanotube. *Inset:* SEM picture of the CNT with contacts and a side gate for changing the QD potential.

with $\kappa = \int_0^{+\infty} d\omega \frac{e^3}{2\pi(\hbar\omega)^2} |Z(\omega)|^2 I_{SIS,0}(V_{det} + \frac{\hbar\omega}{e})$ a function that depends on transimpedance, detector $I - V$ characteristic in the absence of noise, and detector bias. Equation 5.3 is valid in general, for any white noise source that is coupled to the SIS detector junction. We use κ as a calibration function for our detection scheme and in the Appendix we discuss the limits in which this procedure is valid.

5.3 Carbon Nanotube Characterization. Noise Detection

The single wall nanotube has a length of $l = 1.6 \mu\text{m}$ between the contacts. A side gate, at a distance of 200 nm and over a length of 1 μm , is used to capacitively change the electrical potential (see Inset of Fig. 5.3). From the observation that we can induce both electron and hole transport through the nanotube at room temperature we conclude that we have a small gap semiconductor CNT. After cooling to $T = 20 \text{ mK}$, we measure the current through the nanotube, I_{nt} , as a function of applied bias, V_{nt} , and gate voltage, V_g . The conductance, dI_{nt}/dV_{nt} , density plot shows closing Coulomb diamonds, implying that one quantum dot is

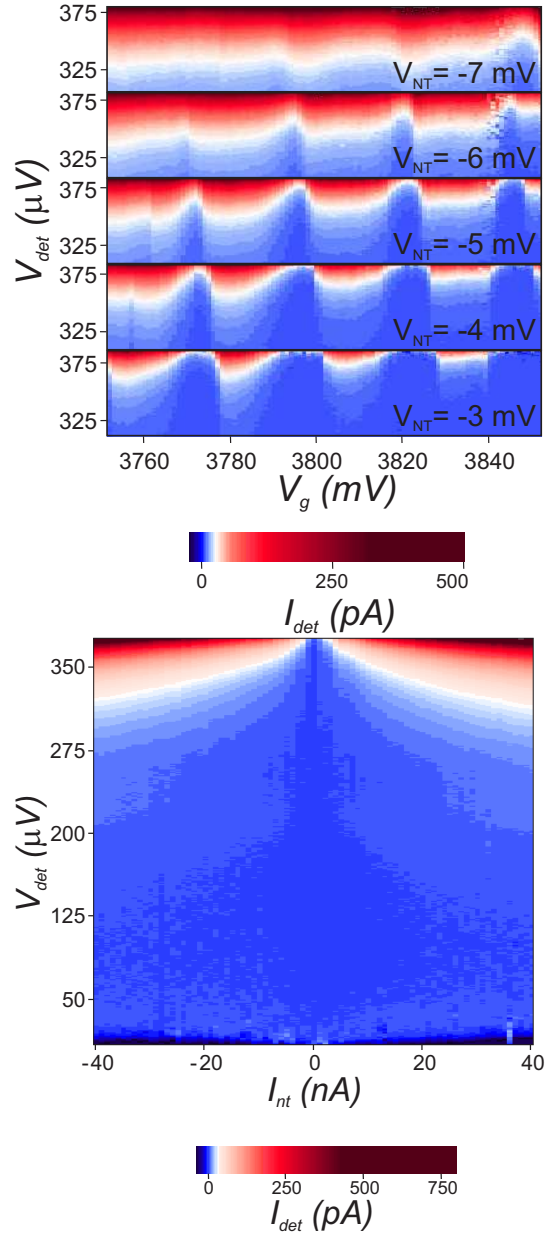


Figure 5.4: **a** PAT signal as a function of carbon nanotube gate voltage, V_g , for different voltage biases, V_{nt} . The gate voltage modulates the current through the quantum dot, accompanied by a change of the current fluctuations. This noise is detected in I_{det} and is shown in colour scale here. **b** Density plot of the detector signal, I_{det} , for the current biased nanotube as a function of detector bias, V_{det} , and current driven through the nanotube, I_{nt} . The detector signal is modulated by the current through the nanotube: I_{det} is larger for $I_{nt} = -40$ nA and 40 nA, and is suppressed when $I_{nt} = 0$.

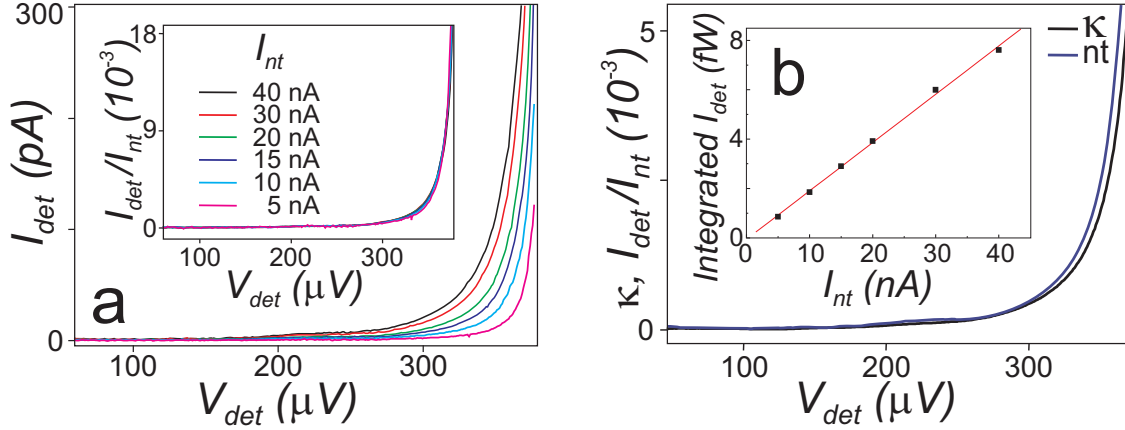


Figure 5.5: (a) Individual curves for the detector signal, I_{det} , as a function of detector bias, V_{det} , for several nanotube current bias values, I_{nt} . *Inset:* the same detector signal curves normalized to the value of the current through the nanotube. (b) Averages of normalized detector curves for the calibrating SIS-SIS, respectively SIS-CNT sample. *Inset:* Integrated detector signal, $\int I_{det} dV_{det}$ (for $140 \mu V \leq V_{det} \leq 370 \mu V$), versus CNT current, I_{nt} .

formed in the CNT (see Fig. 5.3). Excited states are present for both positive and negative bias voltages. They are clearly stronger for one direction (parallel to one side of the Coulomb diamonds), indicating the dot is asymmetric in terms of the tunneling barriers to the leads. From the size of the larger Coulomb diamonds, we can estimate the addition energy $\delta + E_C \approx 4$ mV, with $\delta \approx 1$ meV the orbital energy and $E_C \approx 4$ meV the charging energy. The value for δ is consistent with the figure expected for a quantum dot formed by barriers at the contacts.

Fig. 5.4a presents density plots for the detector signal, I_{det} , as a function of detector bias, V_{det} , and nanotube gate voltage, V_g . The gate voltage shifts the energy levels in the quantum dot bringing the last occupied charge state in and out of resonance with the Fermi levels in the leads. As a result, the current I_{nt} and subsequently the noise power S_I , are modulated. This modulation is more evident at lower bias voltages where the relative change in the current through the nanotube is also stronger. The range of bias voltages $V_{nt} = -7$ mV to -3 mV was chosen for a good illustration of the modulation.

We fix then the gate voltage at a Coulomb peak position and current bias the nanotube. The density plot for the detector signal, I_{det} , is shown in the in Fig. 5.4b for I_{nt} between -40 and 40 nA. Cuts along the detector bias are presented in Fig. 5.5. The detector signal is increasing with the CNT current, I_{nt} . The fact that the normalized curves I_{det}/I_{nt} are identical, over the range of applied I_{nt} (see inset of Fig. 5.5), shows that we are indeed measuring shot noise.

This is also apparent from the inset of Fig. 5.5(b), showing that the integrated detector signal depends linearly on the nanotube current.

Since the power spectral density can be expressed as $S_I = FeI_{nt}$, the normalized curve can be written as

$$I_{det}/I_{nt}(V_{det}) = F \kappa(Z, I_{SIS,0}, V_{det}). \quad (5.4)$$

We determine the circuit calibration function κ by using a separate sample, in which well-known Poissonian noise is generated (see Appendix). This calibration sample is fabricated simultaneously with the CNT sample, but with an SIS junction as a noise source. The obtained calibration curve is presented in Fig. 5.5(b). We also plot there the normalized curve I_{det}/I_{nt} , averaged for CNT currents between 5 nA and 40 nA. The two curves have similar amplitudes, meaning that, for a given value of the current through the source, the detector signal is the same for the two samples. This indicates a Fano factor close to the Poissonian value $F = 1$ [9] for the high bias regime of the CNT. Based on these considerations, we use below the normalized curve, $\kappa_{nt} = I_{det}/I_{nt}$, in Fig. 5.5(b) as a calibration curve. We estimate that the deviation of the Fano factor from the $F = 1$ value is less than 12% (see Appendix). Our calibration allows for detection of changes in the Fano factor within this error bar.

We now focus on the two adjacent Coulomb diamond shown in Fig. 5.6: density plots of (a) current through the dot, I_{nt} , and (b) the conductance, dI_{nt}/dV_{nt} , as a function of nanotube bias and gate voltage obtained from standard DC transport measurement. Excited states are clearly visible for both positive and negative bias voltages, V_{nt} , and inelastic cotunneling processes give rise to a finite current inside the Coulomb blockade region. We now use the SIS detector junction to measure the noise generated by the quantum dot. We fix the gate voltage, V_g , and measure the detector current with finite (I_{SIS}) and zero ($I_{SIS,0}$) nanotube bias voltage, V_{nt} . Then the values for V_g and V_{nt} are changed and the noise measurements repeated. In this way we obtain the detector signal $I_{det} = I_{SIS} - I_{SIS,0}$ over the entire range of the Coulomb diamond.

Due to detection time constraints, we sweep the detector bias V_{det} only over a limited interval (V_{det}^i, V_{det}^f) of the superconducting gap region, where the detector is most sensitive [10]. We obtain the noise power over this interval from

$$S_I/e = \frac{\int_{V_{det}^i}^{V_{det}^f} I_{det}(V_{det}) dV_{det}}{\int_{V_{det}^i}^{V_{det}^f} \kappa_{nt} dV_{det}} \quad (5.5)$$

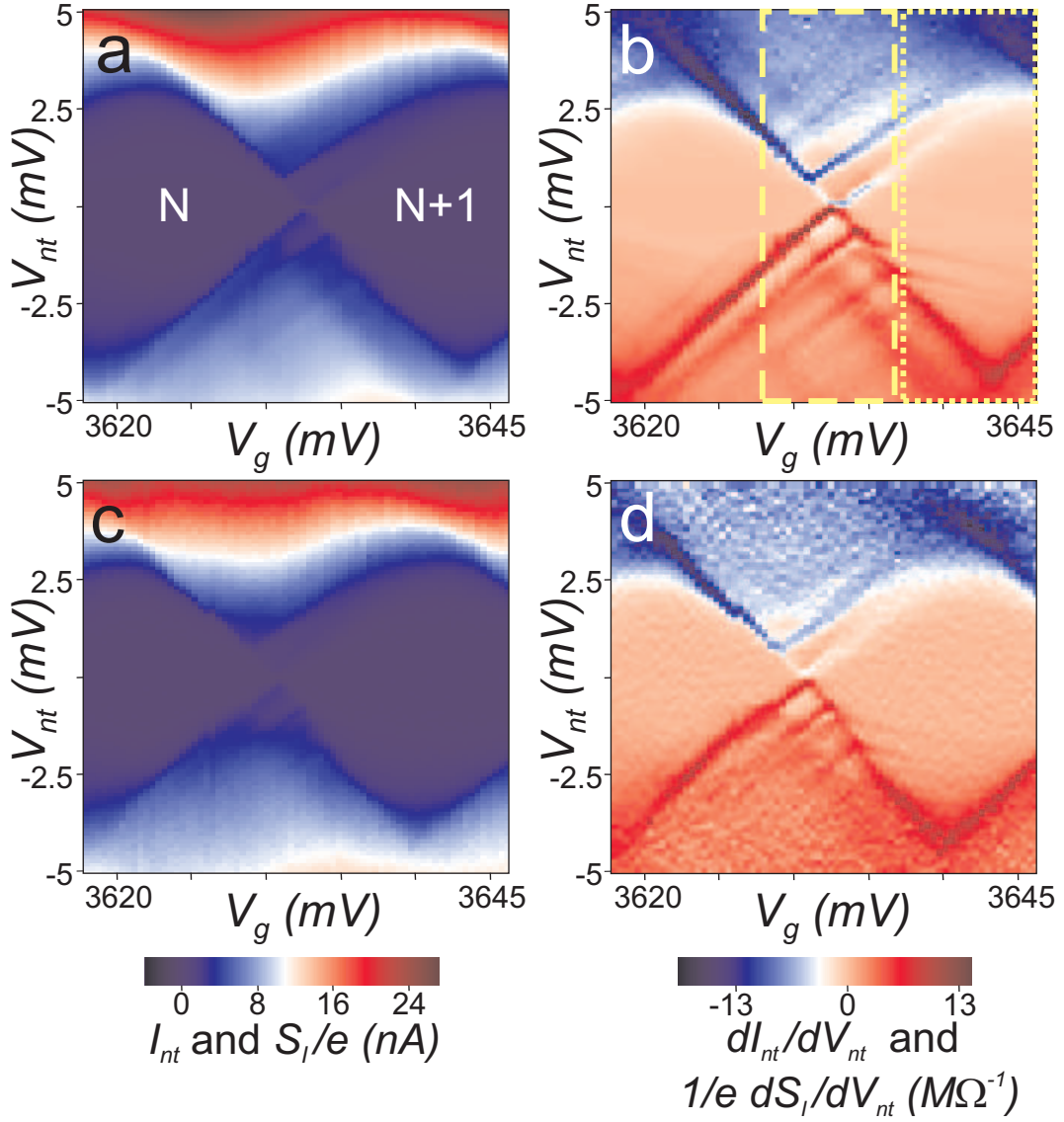


Figure 5.6: Density plots for DC ((a) and (b)) and noise measurements ((c) and (d)) for the transport through the CNT-QD, as a function of nanotube bias, V_{nt} , and gate voltage, V_g . Standard DC measurement of current, I_{nt} , and conductance, dI_{nt}/dV_{nt} , are presented in (a) and (b) for two adjacent Coulomb diamonds. The diamonds correspond to a fixed number of electrons (N , respectively $N + 1$) in the QD. Noise power, S_I , obtained according to Eq. (5.5), together with its derivative, dS_I/dV_{nt} , are presented in (c) respectively (d). Both are normalized to the electron charge such that we can use the same color scale for DC and noise measurements. Our detection scheme proves to be extremely sensitive as we can clearly identify, in the noise measurements, all the features resolved in the DC measurement such as transport through excited states and inelastic cotunneling.

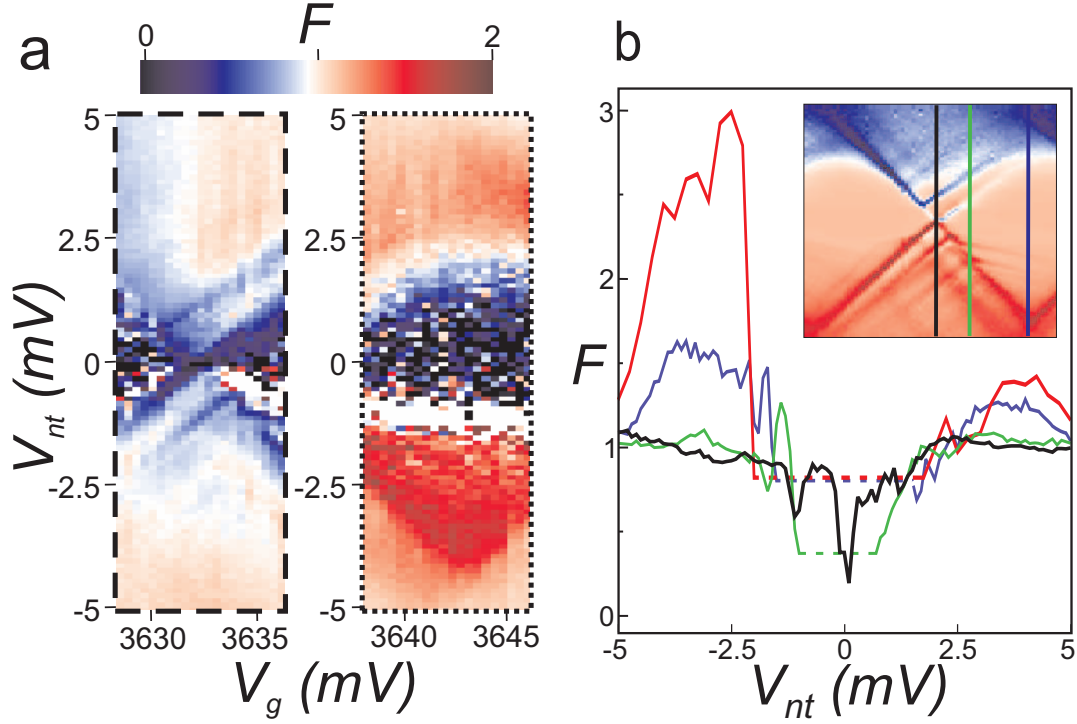


Figure 5.7: (a) Fano factor density plots corresponding to the two parts of the Coulomb diamond indicated in Fig. 5.6(b). (b) Individual Fano factor curves determined for gate voltages indicated in the inset density plot. The red curve was measured in a different Coulomb diamond. $F > 1$ indicates super-Poissonian noise corresponding to inelastic cotunneling. For CNT currents $I_{nt} < 150$ pA (the dashed part of the curves) no excess noise can be measured, with the sensitivity of our detection scheme.

The detector signal is proportional to the current noise generated by the device (see Eq. (5.3) and Fig. 5.5). Equation (5.5) can, therefore, be used to obtain an average for the noise power S_I over the detector points measured. The resulting density plots for noise (see Fig. 5.6(c) and (d)) are in good correspondence with the ones from the standard DC measurement (Fig. 5.6(a) and (b)). This is expected, as changes in I_{nt} also give changes in $S_I \propto I_{nt}$. There is a small shift in gate voltage values between the noise and the DC measurement (due to the long measurement time for noise detection). Excited states, as well as inelastic cotunneling signal inside the Coulomb diamond, are clearly resolved for both types of measurements.

The density plot for the Fano factor could in principle be obtained by simply dividing the plots in Fig. 5.6(c) and (a). However, in our case, the small gate shifts between the two types of measurements prevent us from easily obtaining it for the entire Coulomb diamond. After careful alignment to correct for the

small gate shifts we get the Fano factor values for specific regions outlined by the dashed and dotted lines in Fig. 5.6(b). These values, presented in Fig. 5.7(a), indicate a noise suppression ($F < 1$) at the closing of the diamond (dashed part) and an enhancement of noise ($F > 1$) in the regime of inelastic cotunneling (dotted part). Fano factor curves are also individually determined and plotted in Fig. 5.7(b).

We first consider the situation when the QD is outside Coulomb blockade (left part of Fig. 5.7(a) and black curve in Fig. 5.7(b)). For small biases, close to the diamond crossing, we find that noise is suppressed $F < 1$, most likely because the barriers are not completely asymmetric. At large biases (where also $I_{nt} > 5$ nA) we detect Poissonian shot noise, in agreement with the calibration procedure. Thus, measurements in the sequential tunneling regime are consistent and prove that our detection scheme is reliable.

We now look at the region inside the Coulomb diamond, where transport occurs via cotunneling (see right part of Fig. 5.7(a)). First, for elastic cotunneling, no noise is measured ($F \approx 0$ in the dark-blue region). This is a second order process, in which an electron is transferred between the leads, via an intermediate virtual state. The electron has a very short dwell time and leaves the dot in its ground state. Subsequent elastic cotunneling events are completely uncorrelated and Poissonian shot noise is predicted, i.e. $F = 1$. However, our signal is obtained after subtracting the detector $I - V$ in the absence of device bias: $I_{det} = I_{SIS} - I_{SIS,0}$. This removes any features due to transport mechanisms in the sub-gap region (e.g. multiple Andreev reflection [11] or multiparticle tunneling [12], depending on the transmissions [13, 14]) or due to additional sources of noise, besides the device. We only measure the excess noise (the noise induced by the CNT bias). In the regime of elastic cotunneling I_{nt} is too small (< 150 pA) to give a measurable contribution to the excess noise, and our subtraction procedure yields $F \approx 0$.

Finally we consider the inelastic cotunneling regime. The green curve in Fig. 5.7(b), taken at a gate value where inelastic cotunneling sets in, shows a small region in V_{nt} with super-Poissonian noise. The blue curve indicates an increase of the region with $F > 1$. Measurements of super-Poissonian noise, due to inelastic cotunneling, were also performed for other Coulomb diamonds (see red curve in Fig. 5.7(b)), showing a very pronounced Fano factor enhancement. Super-Poissonian noise can occur when two channels, with different transparencies, are available for transport [15, 16, 17, 18]. If only one can be open at a time, electrons are transferred in bunches whenever transport takes place through the more transparent channel. Such conditions are met by a quantum dot in the inelastic cotunneling regime. In the ground state, current is blocked due to

Coulomb interaction. Still, if the bias is larger than splitting between the ground and the first excited state, a second order, inelastic tunneling processes can take place and an electron is transferred from one lead to the other. The inelastic cotunneling leaves the dot in the excited state. The electron can subsequently either tunnel out or relax to the ground state and block again the current. Thus, depending on the tunneling rate through the excited state and the relaxation rate, we can distinguish two regimes. If the electron relaxes to the ground state, we are in the weak cotunneling regime. For noise, this is equivalent to elastic cotunneling (the electron always relaxes and tunnels out from the ground state) and leads to Poissonian noise $F = 1$. If relaxation is slow and transport takes place through the excited state (strong cotunneling regime), electrons are transferred in bunches and the noise becomes super-Poissonian. For inelastic cotunneling we measure $F > 1$, showing that we are in the strong cotunneling regime. Still relaxation processes play an important role and lead to a Fano factor smaller than the maximum $F = 3$ predicted value.

5.4 Conclusions

We use a SIS junction to detect the high frequency noise generated by a quantum dot formed in a carbon nanotube. Noise measurement over the entire Coulomb diamond region are reported for the first time. Features present in the standard current measurements, including excited states and inelastic cotunneling, are clearly resolved in noise measurements. This confirms the high sensitivity and versatility of our detection scheme. Super-Poissonian noise ($F > 1$), corresponding to inelastic cotunneling, is detected, also for the first time. The noise enhancement is a consequence of electrons being transferred in bunches after each inelastic cotunneling event.

We are grateful to P. Jarillo-Herrero for the assistance in the CNT fabrication. We acknowledge the technical support of R. Schouten and A. van der Enden. Financial support was provided by the Dutch Organization for Fundamental Research (FOM).

References

- [1] Y. M. Blanter, M. Büttiker, Phys. Rep. **336**, 1 (2000).
- [2] *Quantum Noise in Mesoscopic Physics* edited by Y. V. Nazarov (Kluwer, Dordrecht, 2003).

- [3] U. Gavish, Y. Levinson, and Y. Imry, Phys. Rev. B **62**, R10637 (2000).
- [4] R. Aguado and L. P. Kouwenhoven, Phys. Rev. Lett. **84**, 1986 (2000).
- [5] R. J. Schoelkopf, A. A. Clerk, S. M. Girvin, K. W. Lehnert, and M. H. Devoret in [2].
- [6] E. Onac, R. Deblock, L. Kouwenhoven *to be published*
- [7] J. H. Davies, P. Hyldgaard, S. Hershfield, and J. W. Wilkins, Phys. Rev. B **46**, 9620 (1992).
- [8] S. De Franceschi, S. Sasaki, J. M. Elzerman, W. G. van der Wiel, S. Tarucha, and L. P. Kouwenhoven, Phys. Rev. Lett. **86**, 878 (2001).
- [9] A higher curve corresponding to the nanotube sample is in agreement with a larger CNT impedance $R_S = 200 \text{ k}\Omega$ compared with $R_N = 15 \text{ k}\Omega$ of the SIS junction used for calibration (see Appendix B).
- [10] The applied detector bias is between $350 \text{ }\mu\text{V}$ and $400 \text{ }\mu\text{V}$. Due to series resistances in the circuit, this results in a real detector bias between $V_{det}^i \simeq 333 \text{ }\mu\text{V}$ and $V_{det}^f \simeq 370 \text{ }\mu\text{V}$. The corresponding cut-off frequencies $\omega_i \simeq 13.2 \text{ GHz}$, respectively $\omega_f \simeq 4.3 \text{ GHz}$, represent the lower limit for the detection bandwidth.
- [11] G. E. Blonder, M. Tinkham, and T. M. Klapwijk, Phys. Rev. B **25**, 4515 (1982); T. M. Klapwijk, G. E. Blonder, and M. Tinkham, Physica (Amsterdam) **109-110B,C**, 1657 (1982).
- [12] J. R. Schrieffer and J. W. Wilkins, Phys. Rev. Lett. **10**, 17 (1963); L. E. Hasselberg, M. T. Levinsen, and M. R. Samuelsen, Phys. Rev. B **9**, 3757 (1974).
- [13] G. B. Arnold, J. Low Temp. **68**, 1 (1987); T. M. Eiles, J. M. Martinis, and M. H. Devoret, Physica (Amsterdam) **189B**, 210 (1993); E. Bratus, V. Shumeiko, E. Bezuglyi, and G. Wendin, Phys. Rev. B **55**, 12666 (1997).
- [14] J. M. van Ruitenbeek, in [2].
- [15] E. V. Sukhorukov, G. Burkard, and D. Loss, Phys. Rev. B **63**, 125315 (2001).
- [16] A. Thielmann, M. H. Hettler, J. König, and G. Schön, cond-mat/0501534; *ibid.*, Phys. Rev. B **71**, 045341 (2005).
- [17] W. Belzig, Phys. Rev. B **71**, 161301 (2005).
- [18] G. Kiesslich, H. Sprekeler, A. Wacker, and E. Schöll, Semicond. Sci. Technol. **19**, 37 (2004).

-
- [19] H. Birk, M. J. M. de Jong, and C. Schönenberger, Phys. Rev. Lett. **75**, 1610 (1995).
 - [20] A. Nauen, I. Hapke-Wurst, F. Hohls, U. Zeitler, R. J. Haug, and K. Pierz, Phys. Rev. B **66**, 161303 (2002); A. Nauen, F. Hohls, N. Maire, K. Pierz, and R. J. Haug, Phys. Rev. B **70**, 033305 (2004).
 - [21] J. Kong, H. T. Soh, A. M. Cassell, C. F. Quate, and H. Dai, Nature **395**, 878 (1998).

Chapter 6

A Quantum Dot as a High Frequency Shot Noise Detector

E. Onac, F. Balestro, U. Hartmann, Y. V. Nazarov and L.P. Kouwenhoven

We present an experimental realization of a Quantum Dot (QD), operated as a high-frequency noise detector. This is demonstrated by measuring shot noise produced in a nearby Quantum Point Contact (QPC). Current fluctuations in the QPC ionize the QD and are detected thereby. We investigate the dependence of detector signal on the QPC transmission and voltage bias and observe that results are consistent with previous low-frequency measurements. We also observe and explain quantum threshold feature and saturation in the detector signal. This experimental and theoretical study is also relevant in understanding the backaction of a QPC used as a charge detector.

6.1 Introduction

On chip noise detection schemes, where the device and the detector are capacitively coupled using an on chip circuit, can benefit from large bandwidths and the possibility of using quantum detectors, that are sensitive separately to the emission or absorption part of the spectrum [1]. A larger bandwidth results in a better sensitivity and allows one to study the quantum limit of noise. Here, the asymmetry between the occurrence probability of emission and absorption processes becomes significant and leads to an asymmetric spectrum. In this Letter, we investigate the transport through a QD under the influence of high frequency irradiation generated by a nearby QPC. The QPC current fluctuations induce photo-ionization [2], taking the QD out of Coulomb blockade, and allowing therefore sequential tunneling through the excited state. By studying the transient current [3] while changing the QPC parameters, we show that we can perform high frequency shot noise detection in the 20 to 250 GHz frequency range.

One can view the QPC as a charge detector [4] and in this context the experiment provides information regarding the backaction [5, 6, 7] of the QPC when used as an electrometer for QD devices. Here we consider the QPC as a well-known noise source. Indeed the granularity of the electron and the stochastic nature of their transport lead to unavoidable temporal fluctuations in the electrical current, i.e shot noise [8], when the QPC is driven out of equilibrium by applying an external bias. For un-correlated systems, like vacuum diodes [9], noise is characterized by a Poissonian value of the power spectral density, $S_I = 2eI_{dc}$. In the case of a QPC, correlations in the transport can be introduced by the Pauli exclusion principle. This results in a suppression of noise and a spectral density S_I that is reduced below the Poissonian value. When the QPC is driven out of equilibrium, i.e. by applying an electrochemical potential difference between the source and the drain of the QPC, a net current will flow if the QPC is not pinched off. At zero temperature ($k_B T \ll eV_{QPC}$) the stream of incident electrons is noiseless and shot noise, due to the quantum partition, dominates. The electrons are either transmitted or reflected, depending on the QPC transmission T , and $S_I = 2eI_{dc}F$, where $F = \sum_{i=0}^N T_i(1 - T_i) / \sum_{i=0}^N T_i$ is the Fano factor and the summation is over transport channels with transmissions T_i . Shot noise vanishes if all the 1D quantum channels either fully transmit ($T_i = 1$) or reflect ($T_i = 0$). Experimental measurements at lower frequencies have already confirmed this dependence [10, 11, 12].

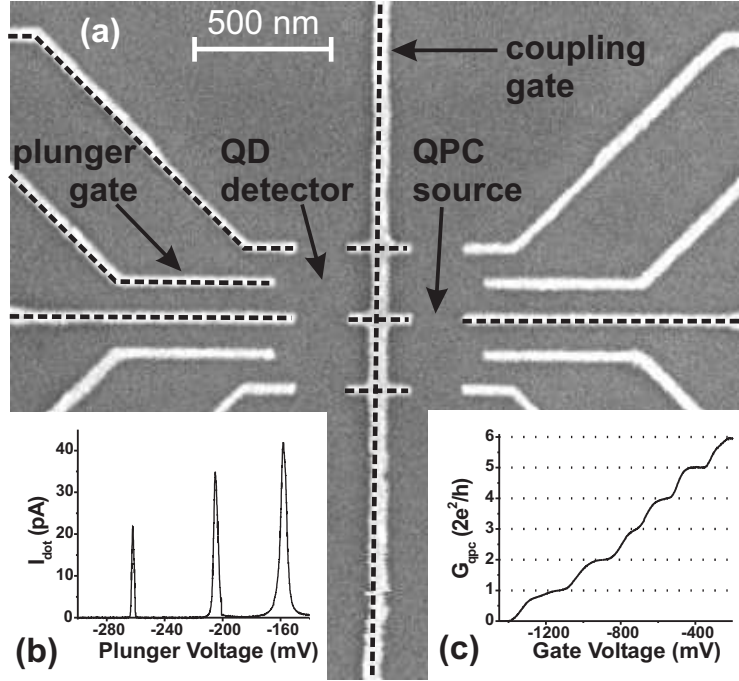


Figure 6.1: (a) Scanning electron micrograph of the gate structure defined on top of the semiconductor heterostructure. The white dotted lines indicate the gates used in the present experiment, defining a quantum dot on the left, and a quantum point contact on the right. All the other gates are grounded. (b) Dot current as a function of the plunger gate voltage for a voltage bias $V_{QD} = 30 \mu\text{V}$ and at a $B = 1.35 \text{ T}$ magnetic field. (c) QPC conductance, G , as a function of the gate voltage at $B = 0 \text{ T}$. The gate voltage on the separation gate is kept constant. The QPC is used as a noise generator and the QD as a detector.

6.2 Sample Characterization

The QD and the QPC are defined in a GaAs/AlGaAs heterostructure, containing a 2DEG at 90 nm below the surface, with an electron density $n_s = 2.9 \times 10^{11} \text{ cm}^{-2}$. We apply appropriate gate voltages such that we form a QD on the left and a QPC on the right (Fig. 6.1a). The lithographic size of the QD is about $250 \times 250 \text{ nm}^2$. Its charging energy, derived from the spacing between Coulomb conductance peaks (Fig. 6.1b), is $E_C = 1.3 \text{ meV}$. With the change of the gate voltage, the QPC manifests conductance quantization [13] (Fig. 6.1c), that can be understood in terms of the Landauer formula $G_{\text{qpc}} = (2e^2/h) \sum_{i=1}^N T_i$.

We regard the QPC as a noise generator that can be 'switched' ON or OFF by applying a voltage bias V_{QPC} and/or changing the QPC transmissions T_i . We measure transport through the QD, as a function of the plunger gate voltage,

under the influence of the noise generator. Where mentioned, a magnetic field was applied, perpendicular to the 2DEG. Stray capacitances in the measurement leads act as short circuits for the high frequency signals and we use the impedance of the edge states as an insulation between the source-detector part and the leads. In this way, the magnetic field enhances the coupling between the source and the detector. We present in this Letter only on measurements performed using the configuration of Fig. 6.1a. Measurements were also performed using the opposite configuration, i.e. defining the QD on the right, and the QPC on the left, with identical results. The experiment was performed in a dilution refrigerator, with an effective electron temperature of 200 mK.

6.3 Noise Detection

The measurements we present are done on a QD containing 10 electrons. This number was measured using the QPC as a charge detector for the QD [4]. The voltage bias across the QD, $V_{QD} = 30 \mu\text{V}$, is much smaller than the level spacing between the ground state and the excited states of the QD. For the configuration in which we use the QD, these energies are larger than $200 \mu\text{eV}$. When the high frequency noise generator is 'switched' OFF (i.e. $V_{QPC} = 0$ or the total QPC transmission $T = \sum_i T_i$ has an integer value), we measure current due to resonant tunneling through the ground state of the QD (see Fig. 6.1b or Fig. 6.2a for $T = 0$). In this situation, current can only flow through the QD when a charge state is positioned between the Fermi energies of the leads. When the last occupied QD level is below both electrochemical potentials of the leads, first order tunnel processes and the associated current are blocked by the Coulomb interaction.

However, if the noise generator is 'switched' ON (i.e. when the QPC is set out of equilibrium by applying a bias voltage), additional current peaks emerge in the Coulomb blockade region. The amplitude of these peaks (labelled 1^{st} es and 2^{nd} es in Fig. 6.2.a) depends on the QPC transmission, and on the voltage applied to the QPC (Fig. 6.4a). Note that we also measured this effect when the QPC was current biased.

The additional peaks in the Coulomb blockade regime correspond, in energy, to the excited states of the QD. These energies were determined from spectroscopy measurements using large QD voltage bias. The energy differences between the excited states (1^{st} and 2^{nd}) and the ground state (see Fig. 6.2c) are equal to $\varepsilon_1 = 245 \mu\text{eV}$, respectively $\varepsilon_2 = 580 \mu\text{eV}$. The QPC gate voltage is adjusted during the QD measurement in order to compensate for the capacitive coupling

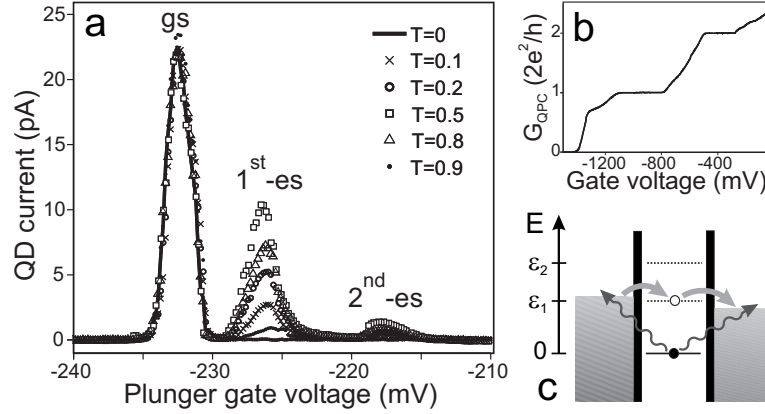


Figure 6.2: (a) Current through the QD, as a function of the plunger gate voltage, under the influence of shot noise generated by the QPC. Measurements are presented for $V_{QD} = 30 \mu\text{V}$, $V_{QPC} = 1.27 \text{ mV}$ and for different QPC transmissions. (b) QPC conductance versus the gate voltage. (c) Schematic representation of the processes that can lead to transport through the first excited state of the QD. Measurements are performed in a $B = 1.35 \text{ T}$ perpendicular magnetic field.

of the plunger gate to the QPC. This allows us to have a well defined transmission T for the QPC, while measuring the QD. We detect a current flowing through the 1st excited state of the QD for total QPC transmission going from 0 to 2, and through the 2nd excited state when only the first QPC channel is open for transport ($0 < T < 1$).

These data can be explained as follows. In the absence of noise, transport through the excited state is blocked since Coulomb blockade prevents having electrons in both the ground state and the excited state simultaneously. The appearance of transport peaks in the Coulomb blockade region is due to a photo-ionization process induced by the high frequency shot noise generated by the QPC. Here, an electron in the ground state absorbs enough energy such that it can leave the dot. Subsequently, a transient current flows through the excited state, as long as the ground state stays empty (Fig. 6.2c). This results in the appearance of conductance peaks, whenever an excited state is between the Fermi levels of the leads. This way, the current fluctuations through the QPC are converted directly into a DC current, flowing through the excited state of the QD. The transient current can be analyzed in order to obtain information regarding the high frequency fluctuations.

6.4 Theoretical Model

For a theoretical description of our results, we first address the question of how the noise couples to the QD? The conversion of QPC current fluctuations into voltage fluctuations on the QD side is described by a circuit transimpedance [1] defined as $|Z(\omega)| = \sqrt{S_V(\omega)/S_I(\omega)}$, with $S_I(\omega)$ the spectral current density of noise generated by the QPC and $S_V(\omega)$ the power spectral density of voltage fluctuations at one barrier of the QD. This can be expressed as $|Z(\omega)| \approx |Z(0)| = \kappa R_K$, where $R_K = e^2/h = 25.8 \text{ k}\Omega$ is the quantum resistance and κ is a dimensionless parameter describing the coupling between different QPC channels and QD barriers. In the theory, we define 4 different κ coefficients depending on the channel involved in the QPC, and the barrier of the QD: $\kappa_{L,1}$ and $\kappa_{L,2}$ are the coupling coefficients between the first respectively the second channel of the QPC and the left barrier of the QD, and $\kappa_{R,1}$ and $\kappa_{R,2}$ describe the coupling of the QPC channels to the right barrier. Experimentally, we can adjust the QD barriers in order to have symmetric escape rates to the left and the right reservoirs. The absence of pumping effects close to the Coulomb peaks (see Fig. 6.2a) indicates symmetric coupling for the QD barriers $\kappa_R = \kappa_L = \kappa$. Thus, the only independent coupling parameters are $\kappa_1 \neq \kappa_2$ corresponding to the first 2 QPC channels. As already discussed, a perpendicular magnetic field can be used to increase the coupling parameter κ .

The second question we address is what kind of energies and cut-off frequencies are involved in the photo-ionization process? In the low temperature limit, two energy scales are important for the detection mechanism. First, the energy difference ε between the ground and the excited state of the QD is relevant, as the photo-ionization process pumps an electron out from the ground state. This level spacing (see Fig. 6.2.c) sets a detector cut-off frequency $\nu_{QD} = \varepsilon/h$, representing the minimum frequency that can induce photo-ionization (the minimum energy that can be detected, assuming single photon PAT processes). The second relevant energy is the one provided by the QPC bias. This gives the cut-off frequency for the noise generator $\nu_{QPC} = eV_{QPC}/h$, corresponding to the maximum frequency that can be emitted (for independent tunneling events in the QPC). Thus, the frequencies contributing to the PAT process are in the range $[\nu_{QD}, \nu_{QPC}]$. For the measurements in Fig. 6.2a, $V_{QPC} = 1.268 \text{ mV}$, which corresponds to $\nu_{QPC} = 317 \text{ GHz}$, and, depending on the 1st or 2nd excited states, ν_{QD} is equal to $\varepsilon_1/h = 59 \text{ GHz}$ or $\varepsilon_2/h = 140 \text{ GHz}$. These set two different detection bandwidths for the 1st and the 2nd excited state, leading to different amplitudes for the detector signal (i.e. the transient current).

The theory considers PAT in a QD. Noise generated by the QPC induces po-

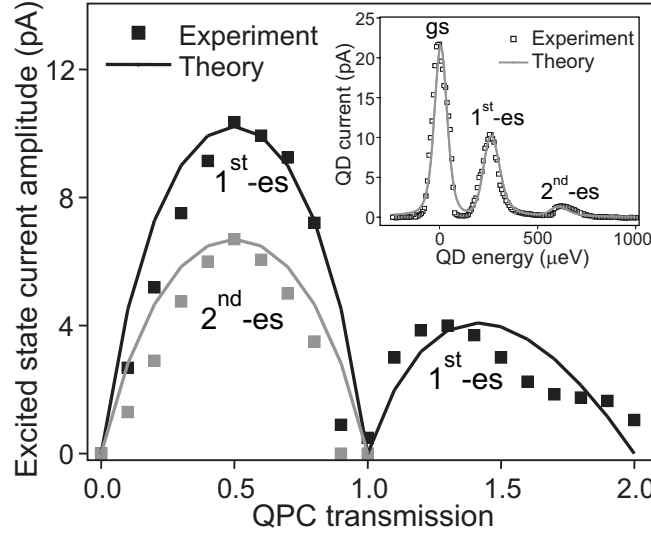


Figure 6.3: Amplitude of the current through the excited state of the QD as a function of the QPC transmission. Measurements are performed at 1.35 Tesla with $V_{QD} = 30 \mu\text{V}$ and $V_{QPC} = 1.27 \text{ mV}$. The current amplitude through the 2^{nd} excited state ($\varepsilon_2 = 580 \mu\text{eV}$) for $0 < T < 1$, and through the 1^{st} excited state ($\varepsilon_1 = 245 \mu\text{eV}$) for $1 < T < 2$ have been multiplied by a factor of 5 for clarity. Inset: QD current as a function of the QD energy for a QPC transmission $T = 0.5$. Experimental points are in good agreement with the solid, theoretical curve. Note that we converted the plunger gate value in QD energy for clarity.

tential fluctuations between the QD energy levels and the electrochemical potentials in the leads. These fluctuations modify the tunneling rates Γ_L , Γ_R between the QD and its source and drain leads. This change can be described using the theory of energy exchange with the environment [14], where the photo-ionization probability can be written as $P_i(E) = \frac{1}{\pi w_i} \frac{1}{1+E^2/w_i^2}$. This Lorentzian dependence on energy has a width $w_i = 8\pi^2 \kappa_i^2 T(1-T)eV_{QPC}$ [1] that includes the coupling coefficient as well as the noise power emitted by the QPC.

Using this theoretical model, we can fit the experimental results and obtain the parameters that characterize our system. We first extract the tunneling rate through the ground state of the QD by fitting the Coulomb peak when the noise generator is 'switched' OFF (no additional peaks in the Coulomb blockade regime). We tune the system, by applying appropriate gate voltages on the electrodes, in order to have a symmetric QD: the two tunneling rates from QD to source (Γ_L) and drain (Γ_R) are equal. From the fit results a value of $\Gamma_L = \Gamma_R = 0.575 \text{ GHz}$. The electron temperature, the voltage across the QD and across the QPC are known parameters, and are respectively equal to 200 mK, 30 μV , and 1.27 mV. In order to explain the additional peaks in the Coulomb

blockade regime, and the modulation of these peaks as a function of the QPC transmission, we introduce one set of fitting parameters: the escape rates Γ_1^{es} and Γ_2^{es} of the first and the second excited state, the coupling coefficients κ_1 and κ_2 to the first and the second channel of the QPC. By using this set of four fitting parameters, we are able to obtain a good theoretical fit for QD current dependence on the plunger gate voltage, in the presence of noise (see inset of Fig. 6.3). The resulting values for the excited states escape rates $\Gamma_1^{es} = 5.75$ GHz, $\Gamma_2^{es} = 4.03$ GHz, and for the coupling coefficients $\kappa_1 = 1.67 \times 10^{-2}$, $\kappa_2 = 4.83 \times 10^{-3}$ are reasonable. The values for the escape rates of the excited states are in accordance with previous experimental measurements [15]. The coupling coefficients are more difficult to estimate and they depend strongly on the details of the electromagnetic environment (e.g. on the geometry of the sample). There is one order of magnitude difference between the coupling to the first and the second channel of the QPC. Indeed, the coupling from the second channel is suppressed due to shunting provided by the first, conducting channel.

In Fig. 6.3 we plot the current flowing through the 1st (black square) and the 2nd (gray square) excited state of the QD as a function of the QPC transmission T . The points represent the current amplitude of transport through excited states and are extracted from measurements presented on Fig. 6.2a. The QD detector signal is modulated by changing the QPC transmission: shot noise vanishes for integer values ($T = 1$ or $T = 2$) and is maximal for $T = 0.5$ and close to $T = 1.4$. The solid lines represent theoretical calculated values by making use of the previous determined parameters. We note that one set of fitting parameters can be used to describe the PAT signal dependence on both the QD energy and the QPC noise power. In Fig. 6.3, a factor 5 has been introduced in the vertical scaling for the 2nd excited state, and also for the 1st excited state from $T = 1$ to 2, for clarity. The suppression of the detector signal for these two cases was already discussed: low amplitude of the 2nd excited state current is due to a smaller detection bandwidth, while the noise generated by the second QPC channel is partly screened by the electrons flowing through the first, ballistic channel. This is also the reason why it is less efficient to use the QPC as an electrometer in this transmission range.

In Fig. 6.4, we measure and theoretically compute the saturation of the excited state current as a function of V_{QPC} . The plot presents the current amplitude for the ground and the excited state, normalized to the amplitude of the Coulomb peak in the absence of noise. We clearly see that the amplitude of the excited state increases as a function of the QPC cut off frequency ν_{QPC} , while the amplitude of the ground state decreases.

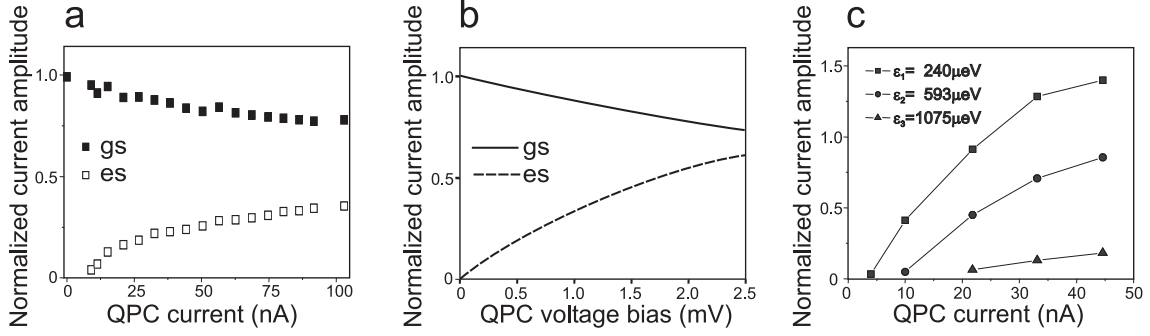


Figure 6.4: (a) Experimental values for the normalized amplitude of current flowing through the ground and excited state as a function of the QPC current. Measurements performed at $B = 2.6$ T, with the QPC current biased at half transmission $T = 0.5$. (b) Theoretical dependence of the normalized amplitude for the current flowing through the ground state and the first excited state of the QD as a function of the QPC voltage bias. We use the parameters from the measurements at $B = 1.35$ T. (c) Quantum limit cut-off frequencies corresponding to three excited states in the quantum dot detector. QPC transmission is set to $T \approx 1/7$.

6.5 High Frequency Cut-off

A distinct quantum feature present in the experimental measurements is the existence of a cut-off in the values of the QPC voltage bias (see Fig. 6.4a). This corresponds to the condition $\nu_{QPC} = \nu_{QD}$ and represents the minimum QPC voltage bias for which the detection bandwidth $[\nu_{QD}, \nu_{QPC}]$ exists. For smaller bias voltages the emission side of the QPC noise is zero at the frequencies $\nu > \nu_{QD}$ where the QD detector is sensitive. The theoretical results are obtained from a ‘classical’, frequency independent, expression for shot noise and, subsequently, they do not show this cut-off. The cut-off in the detector signal corresponding to three excited states are presented in Fig. 6.4c. The noise cut-off frequency associated with the bias $\nu = eV_{bias}/h$ was already measured in the symmetric spectrum of noise [16]. Here we use a quantum detector that allows us to measure, for the first time, the cut-off in the emission part of the spectrum, $S(-\omega)$.

At higher noise power, we measure a saturation for both amplitudes of current through the excited and the ground state. This phenomenon can be understood as an equilibrium is reached in the system between PAT and QD relaxation processes.

6.6 Conclusions

In conclusion, we used a QD as an on chip quantum detector to achieve, for the first time, very high frequency (in the range 20 - 250 GHz) shot noise measurements. The measurement process involves photonionization of the QD due to broadband noise, generated by a nearby QPC. The detector signal shows a noise modulation as a function of the QPC transmission, and is fully understood in the context of a PAT theory. Using this detection technique, we measured the cut-off frequency eV_{QPC}/h in the noise emitted by the QPC. This was done by measuring a threshold frequency for the photoionization process, for a specific QD excited state energy. The process can also be viewed as a backaction of the QPC when used as a QD electrometer and could be an explanation of the dark count in the single-shot readout of an individual electron spin in a quantum dot [17].

We are grateful to L. W. van Beveren and R. Hanson for providing the sample and for discussions. We acknowledge the technical assistance of R. Schouten, A. van der Enden. Financial support was provided by the Dutch Organisation for Fundamental Research (FOM).

References

- [1] R. Aguado and L. P. Kouwenhoven, Phys. Rev. Lett. **84**, 1986 (2000).
- [2] T. H. Oosterkamp, T. Fujisawa, W. G. van der Wiel, K. Ishibashi, R. V. Hijman, S. Tarucha, and L. P. Kouwenhoven, Nature **395**, 873 (1998).
- [3] T. Fujisawa, Y. Tokura, and Y. Hirayama, Phys. Rev. B **63**, 081304 (2001).
- [4] M. Field, C. G. Smith, M. Pepper, D. A. Ritchie, J. E. F. Frost, G. A. C. Jones, and D. G. Hasko, Phys. Rev. Lett. **70**, 1311 (1993).
- [5] S. A. Gurvitz, L. Fedichkin, D. Mozyrsky, and G. P. Bernan, Phys. Rev. Lett. **91**, 066801 (2003).
- [6] E. Buks, R. Schuster, M. Heiblum, D. Mahalu, and V. Umansky, Nature **391**, 871-874 (1998).
- [7] M. Avinun-Kalish, M. Heiblum, A. Silva, D. Mahalu, and V. Umansky, Phys. Rev. Lett. **92**, 156801 (2004).
- [8] Y. M. Blanter and M. Büttiker, Phys. Rep. **336**, 1 (2000).
- [9] W. Schottky, Ann. Phys. (Leipzig) **57**, 541 (1918).

-
- [10] Y. P. Li, D. C. Tsui, J. J. Heremans, G. W. Weimann, and J. A. Simmons, *Appl. Phys. Lett.* **57**, 774 (1990).
 - [11] A. Kumar, L. Saminadayar, Y. Jin, B. Etienne, and D. C. Glatthli, *Phys. Rev. Lett.* **76**, 2778 (1996).
 - [12] M. Reznikov, M. Heiblum, H. Shtrikman, and D. Mahala, *Phys. Rev. Lett.* **75**, 3340 (1995).
 - [13] B. J. van Wees, H. van Houten, C. W. J. Beenakker, J. G. Williamson, L. P. Kouwenhoven, D. van der Marel and C. T. Foxon, *Phys. Rev. Lett.* **60**, 848 (1988).
 - [14] G. L. Ingold and Y. V. Nazarov, in *Single-Charge Tunneling*, edited by H. Grabert and M. H. Devoret (Plenum, New York, 1992)
 - [15] J. M. Elzerman, S. De Franceschi, D. Goldhaber-Gordon, W. G. van der Wiel, and L. P. Kouwenhoven, *Journal of Low Temperature Physics* **118**, 375 (2000).
 - [16] R. J. Schoelkopf, P. J. Burke, A. A. Kozhevnikov, M. J. Rooks, and D. E. Prober, *Phys. Rev. Lett.* **78**, 3370 (1997).
 - [17] J. M. Elzerman, R. Hanson, L. H. Willems van Beveren, B. Witkamp, L. M. K. Vandersypen, and L. P. Kouwenhoven, *Nature* **430**, 431 (2004).

Appendix A

Quasiparticle tunneling current in the presence of an environment

To be more quantitative and take into account the fact the electromagnetic field can have a broad range of frequencies, we consider a SIS junction coupled to an environment characterized by a voltage spectral density $S_V(\omega)$. Again here we consider both negative and positive frequencies, the meaning of this distinction is the same as described in the main text: the negative frequencies correspond to an energy flow from the environment to the SIS junction, i.e. the emission part of the spectrum for the environment. Positive frequencies correspond to energy being absorbed by the environment. This distinction becomes important at high frequencies [1, 2], depending on the detection scheme.

We follow Ingold and Nazarov [3] to derive the expression for the PAT current through an SIS junction in the presence of a high frequency electromagnetic environment. The hamiltonian of a tunnel junction can be written as

$$H = H_{qp} + H_T + H_{env} \quad (\text{A.1})$$

where

$$H_{qp} = \sum_{k\sigma} \epsilon_k c_{k\sigma}^\dagger c_{k\sigma} + \sum_{q\sigma} \epsilon_q c_{q\sigma}^\dagger c_{q\sigma} \quad (\text{A.2})$$

represents the quasiparticles in the left and right electrode with wave vectors k and q ; σ denotes their spin and ϵ_k, ϵ_q their energies. In the tunneling hamiltonian

$$H_T = \sum_{kq\sigma} T_{kq} c_{q\sigma}^\dagger c_{k\sigma} e^{-i\varphi} + H.c. \quad (\text{A.3})$$

the first term describes the creation of an electron of momentum q in the right electrode and the annihilation of one with momentum k in the left electrode. This

transfer is characterized by the tunneling matrix element T_{kq} . The hermitian conjugate term describes the reverse processes and the phase φ is defined as

$$\varphi(t) = \frac{e}{\hbar} \int^t dt' V_{SIS}(t') \quad (\text{A.4})$$

where $V_{SIS}(t)$ represents the voltage drop and the operator $e^{-i\varphi}$ changes the charge on the junction electrodes. Finally H_{env} describes the environment degrees of freedom. In our case (SIS junction used as a detector) the environment is represented by the device under study.

To get rid of the constant phase increase due to the average bias voltage \bar{V}_{SIS} and only remain with the part due to the fluctuation, $\delta V_{SIS}(t) = V_{SIS}(t) - \bar{V}_{SIS}$, it is convenient to make use of a unitary transformation $\tilde{H} = U^\dagger H U - i\hbar U^\dagger \partial U / \partial t$ with

$$U = \exp \left[\frac{iet}{\hbar} \bar{V}_{SIS} \sum_{k\sigma} c_{k\sigma}^\dagger c_{k\sigma} \right] \quad (\text{A.5})$$

This leads to

$$\tilde{H} = \sum_{k\sigma} (\epsilon_k + e\bar{V}_{SIS}) c_{k\sigma}^\dagger c_{k\sigma} + \sum_{q\sigma} \epsilon_q c_{q\sigma}^\dagger c_{q\sigma} + \sum_{kq\sigma} (T_{kq} c_{q\sigma}^\dagger c_{k\sigma} e^{-i\delta\varphi} + H.c.) + H_{env} \quad (\text{A.6})$$

with shifted energy levels between the leads in \tilde{H}_{qp} and a fluctuating phase factor $\delta\varphi(t) = \varphi(t) - e\bar{V}_{SIS}t/\hbar$ in the new tunneling hamiltonian \tilde{H}_T .

The current through the tunnel junction follows from the golden rule

$$\Gamma_{i \rightarrow f} = \frac{2\pi}{\hbar} \left| \langle f | \tilde{H}_T | i \rangle \right|^2 \delta(E_i - E_f) \quad (\text{A.7})$$

which expresses the tunneling rate from a state $|i\rangle = |E\rangle|R\rangle$ to a state $|f\rangle = |E'\rangle|R'\rangle$. Here $|E\rangle$, $|E'\rangle$ represent the quasiparticle states with energies E , E' and $|R\rangle$, $|R'\rangle$ are the reservoir states with energies E_R , E'_R . The total transfer rate from the left to right electrode can be calculated by summing the part of equation (A.7) which represent these transfers over all the initial states ($|E\rangle$ and $|R\rangle$) multiplied by the probability to find these states ($P_\beta(E)$ respectively $P_\beta(R)$) and over all final states ($|E'\rangle$ and $|R'\rangle$)

$$\vec{\Gamma}(V_{SIS}) = \frac{2\pi}{\hbar} \int_{-\infty}^{+\infty} dE dE' \sum_{R,R'} \left| \langle E' | \vec{H}_T | E \rangle \right|^2 \left| \langle R' | e^{-i\delta\varphi} | R \rangle \right|^2 P_\beta(E) P_\beta(R) \delta(E + E_R - E' - E'_R) \quad (\text{A.8})$$

with $\vec{H}_T = \sum_{kq\sigma} T_{kq} c_{q\sigma}^\dagger c_{k\sigma}$ the first part of the new tunneling Hamiltonian and $\beta = 1/k_B T$ the inverse temperature.

The term $\langle E' | T_{kq} c_{q\sigma}^\dagger c_{k\sigma} | E \rangle$ gives a non-zero contribution only when the initial and final states are of the form $|E\rangle = |\dots, 1_{k\sigma}, \dots, 0_{q\sigma}, \dots\rangle$ respectively $|E'\rangle = |\dots, 0_{k\sigma}, \dots, 1_{q\sigma}, \dots\rangle$. This means that in the initial state an electron is occupying the state (k, σ) in the left electrode, whereas the state (q, σ) is unoccupied in the right electrode, leading to $P_\beta(E)$ as a combination of $f(\epsilon_k)[1 - f(\epsilon_q)]$. The argument of the first Fermi function is shifted from $\epsilon_k + e\bar{V}_{SIS}$ in order to be able to use the same Fermi level in the two Fermi functions.

The applied voltage \bar{V}_{SIS} is much smaller than the Fermi energy such that the quasiparticles involved in transport are close to the Fermi level and the tunneling matrix elements $|T_{kq}|^2$ are independent of the energies ϵ_k, ϵ_q . If we gather all the constant terms in the tunneling resistance R_T , equation (A.8) becomes

$$\vec{\Gamma}(V_{SIS}) = \frac{1}{e^2 R_T} \int_{-\infty}^{+\infty} d\epsilon d\epsilon' f(\epsilon)[1 - f(\epsilon')] \sum_{R, R'} |\langle R' | e^{-i\delta\varphi} | R \rangle|^2 P_\beta(R) \delta(\epsilon + e\bar{V}_{SIS} + E_R - \epsilon' - E'_R) \quad (\text{A.9})$$

where the notation for the energies ϵ_k, ϵ_q was changed to ϵ, ϵ' respectively. If we use the identity $\delta(\epsilon) = \frac{1}{2\pi\hbar} \int_{-\infty}^{+\infty} dt \exp(\frac{i}{\hbar}\epsilon t)$ this equation can be rewritten as

$$\begin{aligned} \vec{\Gamma}(V_{SIS}) = & \frac{1}{e^2 R_T} \int_{-\infty}^{+\infty} d\epsilon d\epsilon' \int_{-\infty}^{+\infty} \frac{dt}{2\pi\hbar} \exp\left[\frac{i}{\hbar}(\epsilon + e\bar{V}_{SIS} - \epsilon')t\right] f(\epsilon)[1 - f(\epsilon')] \times \\ & \sum_{R, R'} P_\beta(R) \langle R | e^{i\delta\varphi(t)} | R' \rangle \langle R' | e^{-i\delta\varphi(0)} | R \rangle \end{aligned} \quad (\text{A.10})$$

The probability $P_\beta(R)$ to find the reservoir in the state $|R\rangle$ is

$$P_\beta(R) = \langle R | \rho_\beta | R \rangle \quad (\text{A.11})$$

where $\rho_\beta = Z_\beta^{-1} \exp(-\beta H_{env})$ is the equilibrium density matrix and $Z_\beta = \text{Tr} \{\exp(-\beta H_{env})\}$ is the environment partition function. Taking into account the expression for the equilibrium correlation function

$$\langle e^{i\delta\varphi(t)} e^{-i\delta\varphi(0)} \rangle = \sum_R \langle R | e^{i\delta\varphi(t)} e^{-i\delta\varphi(0)} | R \rangle P_\beta(R) \quad (\text{A.12})$$

and the fact that $|R'\rangle$ form a complete set for the environment, equation (A.10) becomes

$$\vec{\Gamma}(V_{SIS}) = \frac{1}{e^2 R_T} \int_{-\infty}^{+\infty} d\epsilon d\epsilon' f(\epsilon)[1 - f(\epsilon')] \int_{-\infty}^{+\infty} \frac{dt}{2\pi\hbar} \exp\left[\frac{i}{\hbar}(\epsilon + e\bar{V}_{SIS} - \epsilon')t\right] \langle e^{i\delta\varphi(t)} e^{-i\delta\varphi(0)} \rangle$$

$$(A.13)$$

From Wick generalized theorem, if the noise is Gaussian, it follows that

$$\langle e^{i\delta\varphi(t)} e^{-i\delta\varphi(0)} \rangle = e^{\langle [\delta\varphi(t) - \delta\varphi(0)] \delta\varphi(0) \rangle} \quad (A.14)$$

and, if we introduce the notation $J(t) = \langle [\delta\varphi(t) - \delta\varphi(0)] \delta\varphi(0) \rangle$, the Fourier transform of the phase correlator is

$$P(\epsilon) = \frac{1}{2\pi\hbar} \int_{-\infty}^{+\infty} dt \exp \left[J(t) + \frac{i}{\hbar} \epsilon t \right] \quad (A.15)$$

So finally the transfer rate can be expressed as

$$\vec{\Gamma}(V_{SIS}) = \frac{1}{e^2 R_T} \int_{-\infty}^{+\infty} d\epsilon d\epsilon' f(\epsilon) [1 - f(\epsilon')] P(\epsilon + e\bar{V}_{SIS} - \epsilon') \quad (A.16)$$

and it suggests a simple physical interpretation: the Fermi functions give the probability for the initial quasiparticle state on the left side to be occupied and for the final one on the right to be free, while $P(\epsilon)$ represent the probability of energy exchange with the environment: a negative argument ($\epsilon < 0$) designate absorption of energy from environment while a positive one ($\epsilon > 0$) stands for emission of energy by the tunneling quasiparticle.

We considered so far the situation of a normal tunnel junction, where the density of states is constant. In the case of a SIS junction this is modulated due to the superconducting electrodes according to the reduced quasiparticle density of states

$$\frac{N_S(E)}{N_0} = \begin{cases} \frac{|E|}{(E^2 - \Delta^2)^{1/2}} & \text{for } |E| > \Delta \\ 0 & \text{for } |E| < \Delta \end{cases} \quad (A.17)$$

with N_0 the normal density of states corresponding to a Fermi level in the middle of the superconducting gap 2Δ and $N_S(E)$ the density of states in the superconductor. Taking this into account, equation (A.16) for the quasiparticle tunnel rate between the superconducting electrodes becomes

$$\vec{\Gamma}(V_{SIS}) = \frac{1}{e^2 R_T} \int_{-\infty}^{+\infty} d\epsilon d\epsilon' \frac{N_S(\epsilon) N_S(\epsilon')}{N_0^2} f(\epsilon) [1 - f(\epsilon')] P(\epsilon + e\bar{V}_{SIS} - \epsilon') \quad (A.18)$$

The total quasiparticle current through the SIS junction

$$I_{QP}(V_{SIS}) = e \left[\vec{\Gamma}(V_{SIS}) - \overleftarrow{\Gamma}(V_{SIS}) \right] \quad (A.19)$$

can be calculated by making use of the symmetry relation for the two tunneling directions $\vec{\Gamma}(V_{SIS}) = \overleftarrow{\Gamma}(-V_{SIS})$ and the detailed balance symmetry equation $P(-\epsilon) = e^{-\beta\epsilon}P(\epsilon)$ which relates the probabilities for energy emission and absorption from environment. Thus

$$I_{QP}(V_{SIS}) = \frac{1}{eR_T} \int_{-\infty}^{+\infty} d\epsilon d\epsilon' \frac{N_s(\epsilon)N_s(\epsilon')}{N_0^2} \frac{1 - \exp[-\beta e\bar{V}_{SIS}]}{1 - \exp[-\beta(\epsilon' - \epsilon)]} P(\epsilon + e\bar{V}_{SIS} - \epsilon') [f(\epsilon) - f(\epsilon')] \quad (\text{A.20})$$

In the absence of an environment $P(\epsilon) = \delta(\epsilon)$ which in our case translates in $\epsilon' = \epsilon + e\bar{V}_{SIS}$, so that

$$I_{QP,0}(V_{SIS}) = \frac{1}{eR_T} \int_{-\infty}^{+\infty} d\epsilon \frac{N_s(\epsilon)N_s(\epsilon + e\bar{V}_{SIS})}{N_0^2} [f(\epsilon) - f(\epsilon + e\bar{V}_{SIS})] \quad (\text{A.21})$$

At zero temperature and for $V_{SIS} > 0$, if we rename $\epsilon' - \epsilon \rightarrow \epsilon'$ in equation (A.20) and take into account equation (A.21) we can write

$$I_{QP}(V_{SIS}) = \int_0^{+\infty} d\epsilon' P(e\bar{V}_{SIS} - \epsilon') I_{QP,0}\left(\frac{\epsilon'}{e}\right) \quad (\text{A.22})$$

The next step is to relate the energy exchange probability $P(\epsilon)$ to the voltage fluctuations $S_V(\omega)$ induced across the detector. This is done in the main text of chapter 3.

References

- [1] U. Gavish, Y. Imry, Y. Levinson and B. Yurke in *Quantum Noise in Mesoscopic Physics* edited by Y.V. Nazarov (Kluwer, Dordrecht, 2003).
- [2] G. B. Lesovik and R. Loosen, JETP Lett. **65**, 295 (1997).
- [3] G. L. Ingold and Yu. V. Nazarov, in *Single-Charge Tunneling*, edited by H. Grabert and M. H. Devoret (Plenum, New York, 1992.)

Appendix B

Properties and measurement of the calibration function

We determine the calibration function using an identical sample with only the noise source replaced by another SIS junction. In the normal state regime this is a source of well known Poissonian noise. Changes in κ could come from different detector curves, $I_{SIS,0}(V_{det})$, or from a change in the transimpedance, Z . The detector $I-V$'s we can directly compare and they are identical for the calibration and the real sample. To estimate the changes in the transimpedance, we use a simple model (see chapter 3) for expressing $Z(\omega)$ as a function of the values of the circuit elements

$$Z(\omega) = \frac{i\omega C_C R}{2 + i\omega(2C + C_C)R} \left[\frac{1}{R} + \frac{1}{R_S} + \left(\frac{2}{i\omega C_C} + \frac{R}{1 + i\omega C R} \right)^{-1} \right]^{-1} \quad (\text{B.1})$$

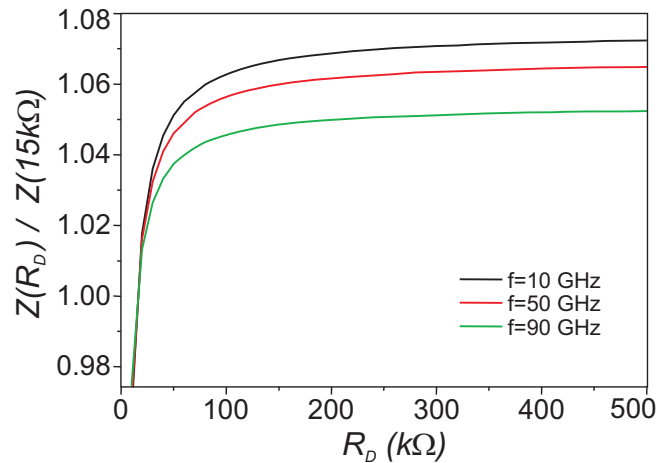


Figure B.1: Change in transimpedance for a circuit with a R_D device with respect to circuit incorporating a 15 kΩ device.

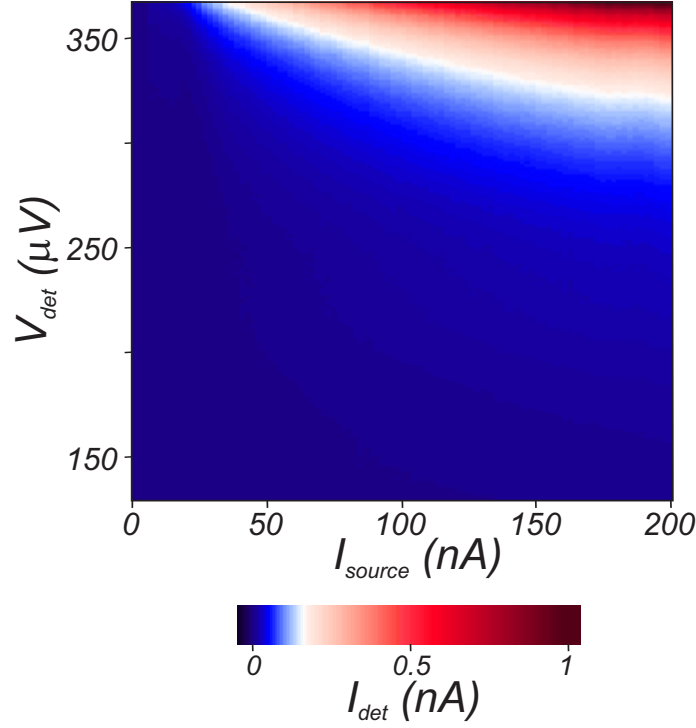


Figure B.2: Density plot for the PAT detector current, I_{det} , as a function of detector bias, V_{det} , and current through the source junction, I_{source} . Making use of the SQUID geometry we tune the magnetic flux such that the detector supercurrent is optimally suppressed. I_{det} is obtained by subtracting the detector I-V in the case of zero current through the source. Therefore, we are left only with the change induced by I_{source} .

R_S is the device impedance and C is the capacitance of the SIS detector junction (its resistance in the sub-gap region is large and can be neglected).

To calibrate our detection scheme we couple the detector to another SIS junction (used as noise source) by making use of the same circuitry elements. Both the calibration and the nanotube sample are fabricated on the same chip. The measured values for the impedances in the bias lines are between $R = 2 \text{ k}\Omega$ and $R = 2.25 \text{ k}\Omega$ (at $T = 4 \text{ K}$) while values for similarly fabricated coupling capacitances are $C_C = 1.2 \text{ pF}$ (with a variation less than 1%). The normal state resistance of the SIS junction used as noise generator is $R_N = 15 \text{ k}\Omega$.

Eq. B.1 allows us to estimate how much the transimpedance is modified by a different device impedance R_S . The results for 3 different frequencies (10, 50 respectively 90 GHz) are presented in Fig. B.1. They indicate a maximum of 7% increase in transimpedance between the calibration sample (with a $R_N = 15 \text{ k}\Omega$ device impedance) and a circuit incorporating a $R_D = 500 \text{ k}\Omega$ device. Furthermore, spread in the values of the circuit elements can induce also a small

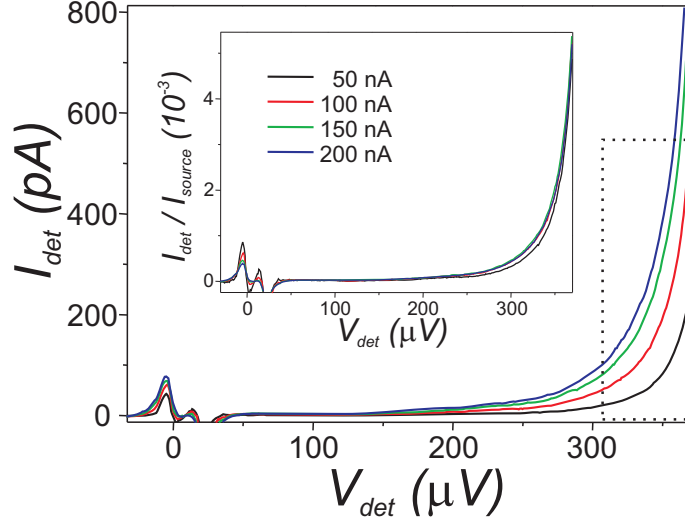


Figure B.3: Extracted detector I_{det} curves as a function of detector bias, V_{det} , for different currents through the source, I_{source} , showing a gradual increase, as expected for the case of white noise. Dotted area indicate the region where the detector is most sensitive. Inset: normalized detector curves I_{det}/I_{source} fall on top of each other confirming the detection of shot noise. (The small deviation in the case of $I_{source} = 50$ nA may indicate that here we are not fully in the normal state regime and correlations are still induced by superconductivity.) The feature around $V_{det} = 0$ μ V is caused by a small super-current still present in the detector (due to slightly asymmetric SQUID junctions).

transimpedance change (e.g. a 12% change in R values could lead to a 10% change in Z). Thus, for similarly fabricated circuits, with devices having comparable impedances, we can use the function κ as a circuit calibration function within a 12% accuracy limit.

For the calibration sample, both the source and the detector were fabricated in a SQUID geometry with different areas, allowing for an independent tuning of the Josephson coupling by means of a perpendicular magnetic field. We current bias the source junction to inject quasiparticles through the tunnel barrier. Tunneling is a stochastic process, leading to current fluctuations with a power spectral density $S_I(\omega)$. These couple as voltage fluctuations $S_V(\omega)$ across the detector.

The density plot of the detector signal is presented in Fig. B.2 for current bias through the source, I_{source} , between 0 and 200 nA. Typical detector curves for several different I_{source} values show a gradual increase of I_{det} (see Fig. B.3). For large biases $V_{source} = I_{source} R_N \gg 2\Delta/e, \hbar\omega/e$ the tunneling processes generate Poissonian shot noise with a power spectral density for the emission side $S_I(-\omega) = eI_{source}$. Using this in equation (5.3), allows us to express the calibra-

tion function as $\kappa = I_{det}/I_{source}$ and plot it in the inset of Fig. B.3.

As expected, the κ curves calculated for different values of I_{source} fall on top of each other. The fact that the detector signal I_{det} scales linearly with the I_{source} is a prove that we are measuring shot noise. An average of normalized curves $\kappa = I_{det}/I_{source}$ (for source junction currents $I_{source} = 65$ nA to 190 nA) is presented in Fig. 5.5b and will be used below to obtain the Fano factor for the noise generated by the nanotube device.

Summary

High Frequency Noise Detection in Mesoscopic Systems

This thesis focuses on high frequency measurements of current fluctuations in mesoscopic devices. Shot noise is a non-equilibrium current noise caused by the granularity of the charge carriers (e.g. electrons). Investigation of non-equilibrium fluctuations at zero temperature can give access to additional information, not available from conventional conductance measurements. Assuming a noiseless source of incident carriers (e.g. electrons from a Fermi sea at zero temperature) shot noise is a direct result of carrier scattering processes taking place in the device. For a small transmission probability, the transfer of electrons is random (completely uncorrelated), and is described by a Poissonian distribution. Interactions between charge carriers inside the device or between the ones in the device and the ones in the leads, regulate the transport and, as a result, shot noise is generally suppressed.

Two new techniques for noise detection are demonstrated in the thesis. The detection principle behind both of them follows a very general idea: the configuration and subsequently the electronic transport properties of a quantum device are modified by the presence of electromagnetic fluctuations in the environment. A noise source, capacitively coupled to this quantum detector, will form its environment. Current fluctuations in the source induce potential fluctuations across the detector. The change in the detector properties (e.g. the DC conductance) can be used to determine the amount of noise generated by the source.

There are a number of advantages of an on chip detection scheme over other ‘conventional’ schemes presented in chapter 2. The detection frequencies are determined by the energy level separation in the quantum detector. For the systems used, they are in the several 10 μeV to several 100 μeV range, corresponding to detection frequencies between 10 GHz and several 100 GHz. At these extremely high frequencies the quantum limit of noise can be addressed, as discussed in chapter 2. A large detection bandwidth increases the noise signal and leads to a

higher sensitivity for the detection of power density. The detection procedure is simple and fast and resides on standard DC measurements.

In chapter 3, a detection scheme using a superconductor-insulator-superconductor (SIS) junction as a noise detector is presented. The detector is coupled on chip to a noise source (another SIS junction). Generated noise induces voltage fluctuations across the detector electrodes and cause photon assisted tunneling of quasiparticles. The resulting change in the detector current is directly related to the noise power density. The maximum detection frequency is determined by the superconducting gap Δ . In case of Al this is ≈ 100 GHz. The detector is voltage biased below $2\Delta/e$, where only the emission side of power spectrum gives a contribution. Frequency resolved measurements are performed when the source is in the AC Josephson regime and white shot noise is detected for the normal state of the source, proving that the detection scheme is reliable and sensitive.

The SIS detection is used in chapter 4 to measure the high frequency signal generated by a two level system (qubit), namely a Cooper pair box. This is a superconducting island connected, by two Josephson junctions in a SQUID geometry, to a superconducting reservoir. Cooper pairs can tunnel onto and off the island. The charge states are coupled by the Josephson energy E_J , resulting in a level repulsion at the charge degeneracy point. Here, coherent oscillations occur with an extra Cooper pair tunneling on and off the island. The state of the qubit can be probed by quasiparticle tunneling at a more resistive junction. When the qubit is electrically driven, a narrow band peak is observed in the spectral density at the frequency of the coherent charge oscillations.

Noise generated by a quantum dot is measured using the same SIS detection and results are presented in chapter 5. The quantum dot is formed in a single wall carbon nanotube. Initial DC conductance measurements are used for characterization. They indicate that a quantum dot is formed between two barriers with different transparencies to the leads. Then, shot noise measurements are performed over the range of two adjacent Coulomb diamonds. For sequential tunneling at large voltage biases shot noise is Poissonian, in agreement with the asymmetric barrier picture. At the closing of the Coulomb diamonds noise is suppressed below the Poissonian value as transport is regulated by Coulomb interaction. Super-Poissonian shot noise is measured for the first time in the case of inelastic cotunneling. This can be understood in the strong cotunneling limit (slow relaxation from the excited to the ground state) as electrons are transferred in bunches, through the excited state, after each cotunneling event.

In the last chapter, a quantum dot is used to measure high frequency fluctuations generated in a nearby quantum point contact (QPC). Alternatively, the process can also be viewed as a backaction of the QPC when used as a electrom-

eter for the quantum dot. Both the quantum dot and the QPC are formed in a 2 dimensional electron gas by means of negative voltages applied to top gates. Current fluctuations in the QPC cause an ionization of the quantum dot. This can lift the Coulomb blockade and transport through excited states becomes possible whenever these are aligned between the Fermi levels in the leads. As a result a transient current flows until the ground state is occupied again and the systems returns to Coulomb blockade. This current represents the detector signal. The detection frequency is determined by the level spacing between the ground and the excited states of the quantum dot and is typically between several 10 GHz and several 100 GHz. Noise measurements are performed as a function of QPC transmission and bias voltage and they are in good agreement with previous results. The cut-off frequency corresponding to the quantum limit is measured in the noise emitted by the QPC.

Eugen Onac
August 2005

Samenvatting

Hoog Frequentie Ruis Detectie in Mesoscopische Systemen

Dit proefschrift spitst zich toe op hoogfrequente metingen van stroomfluctuaties in mesoscopische systemen. Hagel-ruis is een niet-evenwichtstroomruis, veroorzaakt door de discreetheid van de ladingsdragers (b.v. elektronen). Onderzoek naar niet-evenwichtfluctuaties bij het absolute nulpunt van de temperatuur kan additionele informatie verschaffen, die niet verkregen wordt uit conventionele geleidingsmetingen. Hagel-ruis is een direct gevolg van het verstrooien van ladingsdragers in het sample indien wordt aangenomen dat de bron van ladingsdragers (b.v. elektronen afkomstig uit een Fermi-zee op 0 K) ruisloos is. Voor een kleine transmissiewaarschijnlijkheid is het transport van elektronen willekeurig (volledig ongecorreleerd) en wordt beschreven door een Poissonverdeling. Interacties tussen ladingdragers in het systeem, of die tussen de ladingsdragers in het systeem en die in de elektroden, reguleren het ladingtransport en hebben veelal tot gevolg dat de hagel ruis wordt onderdrukt.

In dit proefschrift worden twee nieuwe ruisdetectie technieken gedemonstreerd. Het achterliggende idee van beide technieken berust op het volgende algemene principe: de configuratie van een quantum systeem en daarmee ook de eigenschappen van het elektrische transport door dit systeem worden gemodificeerd door de aanwezigheid van elektromagnetische fluctuaties in de directe omgeving van het quantum systeem. Een ruisbron, die capacitatief aan deze quantum detector is gekoppeld, vormt deze directe omgeving. Stroomfluctuaties in de bron induceren fluctuaties in het potentiaalverschil over de detector. De verandering van de eigenschappen van de detector (b.v. de DC geleiding) kan worden gebruikt om de hoeveelheid door de bron gegenereerde ruis te bepalen.

Een on chip detectiemethode heeft een aantal voordelen boven andere "conventionele" methoden, zoals gepresenteerd in hoofdstuk 2. De detectiefrequenties worden bepaald door de energieverschillen tussen de toestanden in de quantum detector. Bij de gebruikte systemen zijn deze energieverschillen enkele tientallen

μeV tot enkele honderden μeV , overeenkomend met detectiefrequenties tussen de 10 GHz en enkele 100 GHz. Zoals in hoofdstuk 2 wordt beschreven, kan bij deze extreem hoge frequenties de quantum limiet voor ruisdetectie worden gehaald. Een grote detectie bandbreedte verhoogt het ruissignaal en leidt tot een hogere gevoeligheid voor de detectie van de vermogensdichtheid. De detectieprocedure is eenvoudig en snel, en berust op standaard DC metingen.

In hoofdstuk 3 wordt een detectieprocedure beschreven die gebruik maakt van een supergeleider-isolator-supergeleider (SIS) junctie als ruisdetector. De detector is op de chip gekoppeld aan een ruisbron (een andere SIS junctie). De gegenereerde ruis induceert fluctuaties in de spanning over de elektroden van de detector en veroorzaakt foton-geassisteerd tunnelen van quasideeltjes. De resulterende verandering van de detectorstroom is direct gerelateerd aan de vermogensdichtheid van de ruis. De maximale detectiefrequentie wordt bepaald door de supergeleidende gap Δ . In het geval van Al is dit ≈ 100 GHz. Een spanning over de detector lager dan $2\Delta/e$ zorgt ervoor dat alleen de emissie kant van het vermogenspectrum een bijdrage geeft. Frequentie afhankelijke metingen zijn uitgevoerd met de bron afgesteld in het AC Josephson regime. Witte hagel-ruis werd gedetecteerd indien de bron zich in de normale toestand bevond, hetgeen aantoont dat de detectieprocedure betrouwbaar en gevoelig is.

De SIS detectie wordt in hoofdstuk 4 gebruikt om het hoogfrequente signaal te meten dat wordt gegenereerd door een twee-niveau system (qubit), namelijk een Cooper-paar doosje. Dit is een supergeleidend eiland, verbonden aan een supergeleidend reservoir door middel van twee Josephson juncties in een SQUID geometrie. Cooper-paren kunnen naar en van het eiland tunnelen. De ladingstoestanden zijn onderling gekoppeld met de Josephson energie E_J , hetgeen resulteert in afstoting van de niveaus op het ladingontaardingspunt. Op dit punt kunnen coherente ladingsoscillaties voorkomen waarbij een extra Cooper-paar naar en van het eiland tunnelt. De toestand van het qubit kan worden onderzocht door het bestuderen van het tunnelen van quasideeltjes bij een junctie met een hogere resistiviteit. In de spectrale dichtheid wordt een piek met een smalle bandbreedte waargenomen bij de frequentie van de coherente ladingsoscillatie indien de qubit elektrisch wordt aangestuurd.

De door een quantum dot gegenereerde ruis is gemeten met dezelfde SIS detectiemethode en de resultaten worden gepresenteerd in hoofdstuk 5. De quantum dot wordt gevormd in een enkelwandig koolstof nanobuisje. Initiele DC geleidingsmetingen zijn gebruikt voor de karakterisatie van het nanobuisje. Deze metingen geven aan dat een quantum dot is gevormd tussen twee barrières met verschillende transparanties naar de elektroden. Vervolgens zijn er hagel-ruismetingen verricht over het bereik van twee aaneengesloten Coulomb

diamanten. De hagel-ruis heeft een Poissonverdeling in het regime van sequentieel tunnelen met een grote aangelegde spanning, hetgeen overeenkomt met het model van asymmetrische barrière. Bij het sluiten van de diamanten wordt de ruis onderdrukt tot onder de Poissonwaarde aangezien ladingstransport in dat regime wordt gereguleerd door Coulomb interactie. Super-Poissonian hagel-ruis is voor het eerst gemeten in het geval van inelastische cotunneling. Dit kan verklaard worden in de sterke cotunneling limiet (langzame relaxatie van de aangeslagen toestand naar de grondtoestand) aangezien na elke cotunneling gebeurtenis elektronen in groepjes door de aangeslagen toestand getransporteerd worden.

In het laatste hoofdstuk wordt een quantum dot gebruikt om hoogfrequente fluctuaties te meten die worden gegenereerd in een nabijgelegen quantum punt contact (QPC). Dit proces kan ook worden beschouwd als een "backaction" van de QPC indien deze wordt gebruikt als een ladingsdetector voor de quantum dot. Zowel de quantum dot als de QPC worden gevormd in een 2-dimensionaal elektronen gas door een negatieve spanning op gates op het oppervlak aan te bieden. Fluctuaties in de stroom door de QPC veroorzaken een ionisatie van de quantum dot. Dit kan de Coulomb blokkade opheffen en transport door de aangeslagen toestand wordt mogelijk indien deze zijn gepositioneerd tussen de Fermi-niveaus van de elektroden. Dit resulteert in een kortlopende stroom door de dot totdat de grondtoestand weer bezet raakt en het systeem weer Coulomb geblokkeerd is. Deze kortlopende stroom is het detectorsignaal. De detectiefrequentie wordt bepaald door de energiever verschillen tussen de grondtoestand en de aangeslagen toestanden van de quantum dot en is typisch 10 GHz tot enkele 100 GHz. Er zijn ruismetingen zijn gedaan als functie van de QPC transmissie en de aangelegde spanning over de QPC en zij komen goed overeen met eerdere resultaten. De afsnijfrequentie, die overeenkomt met de quantum limiet, is gemeten in de door de QPC gemitteerde ruis.

Eugen Onac
Augustus 2005

Curriculum Vitae

Gabriel Eugen Onac

- 08-11-1975 Born in Luduș, România.
- 1990-1994 Theoretical High School ‘Alexandru Papiu Ilarian’, Târgu Mureș.
- 1994-1999 Physics Engineer, University of Bucharest.
Solid State Department, prof. dr. ir. D. E. Brâncuș.
- 1998-1999 Awarded scholarship at BTU Cottbus, Germany.
Graduate research project with dr. U. Wulf.
Subject: Theoretical study of vertical transport through
quantum dots in parallel magnetic fields using the R-matrix formalism.
- 1999-2001 M.Sc. in Physics, University of Bucharest,
Solid State Department, prof. D. Dragoman.
Master research project: Electron transport
through magnetically modulated structures.
- 2001-2005 Ph.D research at Delft University of Technology
under supervision of prof. dr. ir. L. P. Kouwenhoven.
Subject: High frequency noise detection in mesoscopic devices.

List of publications

1. *Vertical magneto-transport through a quantum dot in the R-matrix formalism*
E. Onac, J. Kucera, and U. Wulf, Physical Review B **63**, 085319 (2001).
2. *Detection of quantum noise from an electrically-driven two-level system*
R. Deblock, E. Onac, L. Gurevich, and L. P. Kouwenhoven, Science **301**, 203-206 (2003).
3. *On chip detection of quantum noise in mesoscopic devices*
E. Onac, R. Deblock, L. Kouwenhoven, in preparation for Physical Review B.
4. *Detection of quantum noise from mesoscopic devices with an SIS detector*
R. Deblock, E. Onac, L. Gurevich, and L. P. Kouwenhoven, in Proceedings of the XXXIXth Rencontres de Moriond 2004 Conference on *Quantum Information and Decoherence in Nanosystems*, edited by D. C. Glattli, M. Sanquer, J. Trân Thanh Vân V. La Thuile, Italy, January 25 - February 1, 41-44 (2004).
5. *Quantum dot as a high frequency noise detector*
E. Onac, F. Balestro, U. Hartmann, Y. V. Nazarov, L. Willems van Beveren, R. Hanson, and L.P. Kouwenhoven, in preparation for Physical Review Letters.
6. *Shot noise detection on a carbon nanotube quantum dot*
E. Onac, F. Balestro, B. Trauzettel, C. F. Lodewijk, and L.P. Kouwenhoven, submitted to Physical Review Letters.

